Alma Mater Studiorum – Università di Bologna

DOTTORATO DI RICERCA IN SCIENZE AMBIENTALI:
TUTELA E GESTIONE DELLE RISORSE NATURALI
CICLO XXI

Settore scientifico disciplinare di afferenza: GEO12

NUMERICAL SIMULATIONS OF PASSIVE TRACERS DISPERSION IN THE SEA

Presentata dalla
Dott.ssa Nicoletta Fabbroni

Relatore
Prof.ssa Nadia Pinardi

Coordinatore Dottorato
Prof.ssa Elena Fabbri

Correlatori
Dr. Paolo Oddo
Prof. Pierre Lermusiaux
Dr. Pierre-Marie Poulain
Dr. Annalisa Griffa

Esame finale 2009

Contents

List of figures

List of tables

Chapter 1

Introduction

1.1 Objectives and structure of the thesis

The simulation and forecasting of passive tracers in the ocean is a challenging task concentrating great interest in the international scientific community for its important ocean applications, including pollutant spreading preventive actions and search and rescue activities.

The objective of this thesis is to develop a suitable set of numerical tools to simulate and predict passive tracer dispersion in open oceans and coastal seas. A Lagrangian particle tracking model coupled with an Eulerian circulation model is proposed.

Since small errors in estimating ocean currents can drastically change particle trajectories (Griffa *et al.*, 2004), an interesting topic is investigating the change in Lagrangian predictability increasing the resolution of the eulerian current field. The objective is then the design and implementation of a relocatable high resolution model nested in coarse resolution operational systems.

The advent of operational oceanography (Pinardi *et al.*, 2002) has prompted the possibility to have first guess fields that are realistic so that particle tracking errors can be controlled. The concept of Maritime Rapid Environmental Assessment (MREA, Robinson *et al.*, 1996) has been extended in this thesis to couple with operational oceanographic products and drifter trajectories simulations. The

results arising from this study can give new tools to a future oil spill model forecasting systems.

This thesis is organized into 4 chapters and one appendix. Each chapter consists of the content of a manuscript which is nearly ready to be submitted for publication in a refereed academic journal.

In Chapter 2, after a brief description of the Lagrangian formulation, four particle-tracking routines are presented. These Lagrangian numerical schemes have been intercompared and the sensitivity of the numerical schemes to time resolution of the Eulerian field is investigated. This work has put the basis to understand the effects of numerical scheme errors in particle trajectories simulations.

In Chapter 3, the predictability and the accuracy of the Lagrangian trajectory model, coupled to a realistic operational numerical forecasting model, is explored by means of a large observational drifter dataset deployed in the Adriatic Sea from 2002 to 2004. In our study the observed drifters are treated as passive tracers and can help us to estimate the uncertainty of the Lagrangian simulation.

Chapter 4 contains the first part of the MREA experiment carried out in the Ligurian Sea in spring-summer 2007 (MREA07). A system of relocatable models, embedded in an operational existing general circulation model, is implemented. The relocatable model represents an affordable solution in order to provide fine resolution forecasting at short time for any sea region of the world. The characteristics of the nested model system are described and the model performance is evaluated using data collected in situ.

Chapter 5 is dedicated to the second part of MREA07 experiment. The hypothesis that higher resolution models could increase the predictability of drifter trajectories is investigated for the specific drifters of the experiment.

Finally, Appendix A contains the MREA08 experiment report, carried out in October 2008 again in the Ligurian Sea. The report describes the oceanographic data collected and presents the preliminary model results provided by a forecasting operational system based on the relocatable model. The operational system was implemented during the experiment in order to release every day a three days current field forecast coupled to drifter predictions. This work is still

preliminary and the scientific study of the results will be restructured in a paper after the thesis.

Chapter 2

Lagrangian Modelling for Particle Prediction in Oceanography

2.1 Introduction

Over recent years, special attention has been paid to the prediction of particle trajectories in the sea. A wide variety of applications are associated with the spreading of tracers considered to be sediments, larvae, phytoplankton or pollutants such as oil or sewage outfalls in the ocean. In particular, the forecast of oil spills in the open ocean and coastal seas is becoming one of the most important applications of operational oceanography. Oil spill predictions will help in preserving a healthy marine environment and developing tools for managing emergencies. The prediction of particle transport in the open ocean and coastal seas has become a reliable tool since numerical models have developed in accuracy and realism. Transport processes are governed by known fluid dynamics equations and numerical solutions of these equations are becoming reliable and standardized. However, the limit of predictability of particle transport is not yet a properly understood problem: the numerical models are affected by uncertainties; small numerical errors can markedly change the trajectories and affect particle path predictions.

In this chapter we review the mathematical description of the advection-diffusion problem and its Eulerian and Lagrangian formulations. Furthermore, we describe several numerical algorithms for the Lagrangian equations. The numerical accuracy is investigated under particular conditions and an estimate of the efficiency and accuracy of the various methods is given.

2.2 The advection-diffusion equation for tracers

The movement and spreading of a tracer in the water can be described by the advection-diffusion equation, which describes the evolution of the tracer concentration in an Eulerian form as (Fischer *et al*., 1979):

$$\frac{\partial C}{\partial t} = -\vec{u} \cdot \nabla C + \nabla \cdot (K \nabla C) + S \tag{2.1}$$

where C is the tracer concentration, the $\partial / \partial t$ operator represents the local time rate of change of the tracer, $\vec{u}$ represents the mean field velocity, $\vec{K}$ is the 'eddy-diffusivity' coefficients which parameterize the turbulence and S incorporates all the tracer sources and sinks. This simple parameterization of the tracer dispersal is obtained using the Reynolds theory: the predictive equation is for the mean components of C, while smaller turbulent scales are parameterized as diffusive processes.

The Lagrangian form of equation (2.1) is:

$$\frac{DC}{Dt} = \nabla \cdot (K \nabla C) + S \tag{2.2}$$

where $\frac{D}{Dt}$ is now the operator that describes changes occurring at the water particle motion.

2.3 Eulerian and Lagrangian formulations

The numerical methods developed to solve the advection-diffusion equation (2.1) can be divided into two main categories: Eulerian and Lagrangian. Hybrid methods are also used in some cases.

The Eulerian method in general solves equation (2.1) on a fixed set of grid points in space; the Lagrangian method, known as 'particle-tracking', transforms the concentration into a discrete and passive set of particles and follows them over time. The concentration at a certain point and time is found assembling the particle trajectories together.

A summary of these methods and an investigation into their efficiency is given in Noye (1987) and Hunter (1987).

The Eulerian method, with the application of finite-difference and finite-element techniques, appears the most popular solution, given that similar techniques are used for the hydrodynamic equations. However, particle-tracking technique can simulate advection to a high degree of accuracy, although the processes of diffusion require stochastic methods (Hunter, 1987).

The particle-tracking model is preferred to the Eulerian for several reasons, summarized as follows by Dimou and Adams (1993):

1. The Lagrangian method represents the sources of contaminant described with particles more easily, while the Eulerian approach cannot resolve processes on a spatial scale smaller than the Eulerian grid resolution;
2. In the particle-tracking method the computational cost is concentrated only in the region where the particles are located, unlike the concentration model, where all domain points are treated at the same time (particle-tracking models may be significantly more computationally efficient);
3. The new parallel computing technique is compatible with the nature of the Lagrangian model and contributes to increase the speed of calculations;
4. Particle-tracking models can describe several natural processes like larva dispersion better;

5. Particle-tracking models can be a mandatory choice when we are interested in properties like residence time.

The particle-tracking methods have been used successfully for the simulation of different natural processes: groundwater dynamics (Tompson and Gelhar, 1990), transport of oil spills (Al-Rabeh *et al*., 1989; Spaulding *et al*., 1994), pollutant dispersion (Al-Rabeh *et al*., 1992; Schönfeld, 1995), larva and sediment transport.

2.4 Lagrangian particle-tracking methods

In this thesis the particle-tracking method has been chosen to simulate particle spreading due to the three-dimensional hydrodynamics of sea water which provides the Eulerian current field. In the Lagrangian model the tracer is modelled by a cloud of massless discrete particles identified by their spatial coordinates. The displacement of each Lagrangian particle is given by a sum of an advective deterministic and a stochastic component; the latter representing the chaotic nature of the flow field, the sub-grid turbulent diffusion.

In the following sections, details of the determinist and stochastic components are given and a brief description of the stochastic theory is presented.

2.4.1 Advection modelling

The movement of Lagrangian particles due to the advection in a three-dimensional current field can be described by the following ordinary differential equations:

$$\frac{d\vec{x}_p}{dt} = \vec{v}(\vec{x}_p, t) \tag{2.3}$$

where $\vec{v}$ is the vector velocity with components (u, v, w) in the x, y and z direction and $\vec{x}_p$ is the coordinate of the particle in the three directions. The movement of the particles can be computed applying a numerical integration scheme to the equation (2.3).

The velocity field is given by an external hydrodynamic model at a series of fixed-point grid and time instants. Particles composing tracers are normally given

at intermediate grid points so that spatial and temporal interpolation is needed. In this thesis we will test different interpolation methods.

2.4.2 Diffusion Modelling

The movement of the particles due to the turbulent part of the flow field is modelled with a random walk scheme (i.e., a Brownian motion process).

The tracer position ($\vec{x}(t) = (x(t), y(t), z(t))$) in a random-walk model can be described by the non-linear Langevin equation (Gardiner, 1985):

$$\frac{d\vec{x}(t)}{dt} = \vec{A}(\vec{x}, t) + \mathbf{B}(\vec{x}, t)\vec{\xi}(t) \tag{2.4}$$

where the vector $\vec{A}(\vec{x}, t)$ represents the deterministic part of the flow field that acts to change $\vec{x}(t)$ (i.e., transport by the mean velocity field), while the second term is a stochastic or diffusion term composed by the tensor $\mathbf{B}(\vec{x}, t)$ that characterizes the random motion and a vector $\vec{\xi}(t)$ the components of which are random numbers with values between 0 and 1.

If we define $W(t) = \int_0^t \xi(s)ds$ and applying the Itō assumption (Tompson and Gelhar, 1990), the equation (2.4) becomes equivalent to the Itō stochastic differential equation:

$$d\vec{x}(t) = \vec{A}(\vec{x}, t)dt + \mathbf{B}(\vec{x}, t)d\vec{W}(t) \tag{2.5}$$

where $d\vec{W}(t)$ is an increment of the 'Wiener process' $\vec{W}(t)$. The Wiener process describes the path of a particle due to Brownian motion and consists of the accumulation of independently stochastic increments $dW(t)$. This term is also called 'white noise' or random forcing with these following properties (Gardiner, 1985):

1. Zero Mean: $\langle dW(t) \rangle = 0$
2. Mean square value proportional to dt: $\langle dWdW \rangle = dt$

In a next step we replace the $d\vec{W}(t)$, in equation (2.5), by a vector of independent random numbers from a standard normal distribution $\vec{Z} \in N(0,1)$ multiplied by $\sqrt{dt}$:

$$d\vec{x}(t) = \vec{A}(\vec{x},t)dt + \mathbf{B}(\vec{x},t)\vec{Z}\sqrt{dt} \ . \tag{2.6}$$

The unknown parameters $\vec{A}$ and **B** can be determined by deriving the Fokker-Planck equation associated with equation 2.6 (Risken, 1989). Under this assumption we can write the 3-D version of the equation (2.6) as follows:

$$d\vec{x}(t) = \begin{pmatrix} u(\vec{x},t) \\ v(\vec{x},t) \\ w(\vec{x},t) \end{pmatrix} dt + \begin{bmatrix} \sqrt{2D_x} & 0 & 0 \\ 0 & \sqrt{2D_y} & 0 \\ 0 & 0 & \sqrt{2D_z} \end{bmatrix} \begin{pmatrix} Z_1 \\ Z_2 \\ Z_3 \end{pmatrix} \sqrt{dt} \tag{2.7}$$

where Z_1, Z_2, Z_3 are the independent random numbers normally distributed around a zero mean value and unit variance and D_x, D_y and D_z are the diffusive coefficients.

2.5 Implementation of the Lagrangian particle-tracking model

In this thesis we have developed different schemes of integration of the Langevin equation (2.4). Four different particle-tracking algorithms have been used, identified by the following names: ARIANE, TRACE, SINCEM and SINCEM2. The first two algorithms were developed by Blanke and Raynaud (1997) and Jarle Berntsen (Institute of Marine Research, Bergen-Nordnes, Norway) and they have been adapted to be coupled with the Eulerian velocity field from our models. The diffusion part of the algorithm has been initially taken to be zero.

The main differences and similarities of the algorithms are listed in Table 2.1.

In the follwing sections we will describe the general characteristics of four algorithms and we will show a first validation with analytical solutions.

	ARIANE	TRACE	SINCEM	SINCEM2
Integration Scheme	Analytical Solution	Euler forward	Euler forward	Fourth-order Runge-Kutta
Spatial Interpolation	Linear interpolation	Linear Interpolation	Bilinear Interpolation	Bilinear Interpolation
Temporal Interpolation	Persistence	Linear Interpolation	Linear Interpolation	Linear Interpolation

Table 2.1 Main characteristics of the particle-tracking algorithms.

2.5.1 ARIANE Algorithm

The ARIANE algorithm was developed by Blanke and Raynaud (1997). ARIANE computes 3D trajectories in the velocity field provided by an ocean general circulation model and it has been used for several studies of water mass dispersion (Blanke *et al*. 1999, 2001; Döös, 1995).

The algorithm is based on the basic assumption of 3D non-divergence (i.e., mass conservation) and it approximates the calculation of analytical streamlines within each model gridcell crossed by a given particle. The trajectory computation involves the interpolation of the three-dimensional Eulerian velocity at the location of a given particle and then its advection by the current. ARIANE is implemented for a C grid (Arakawa, 1972). The three components of the velocity are known over the six faces of each cell grid and a linear variation of each velocity component along each direction is assumed. The final particle position is calculated using the minimum crossing time evaluated independently in each direction by imposing this position as one of the six sides of the grid cell.

Here we report the main equations of the algorithm; for detailed calculations see Blanke and Raynaud (1997).

In each grid cell, the non-divergence of the three-dimensional velocity field $\vec{V} = (U,V,W)$ is defined as function of the transport:

$$\frac{\partial F}{\partial x} + \frac{\partial G}{\partial y} + \frac{\partial H}{\partial z} = 0 \qquad (2.8)$$

where F, G and H represent the transports in the three directions with $F = dydzU$, $G = dxdzV$ and $H = dxdyW$. For a given cell, F, G and H vary linearly in x, y and z.

In the cell extending from $x = 0$ to $x = 1$, the transport F can be written as:

(2.9) $$F(r) = F_0 + r\Delta F$$

with $r \in [0,1]$, $F(0) = F_0$ and $\Delta F = F(1) - F(0)$.

Applying to the transport (F) the equation that links the position to the velocity ($dx/dt = U$) we can obtain:

(2.10) $$\frac{dr}{ds} = F$$

where $s = t/(dxdydz)$ is called the pseudo-time.

Combining equations (2.9) and (2.10) and assuming initially that at $r = 0$, $s = 0$, the time dependency of r within the considered cell is found:

(2.11) $$r = \frac{F_0}{\Delta F}[\exp(\Delta F s) - 1].$$

If $\Delta F = 0$, we have:

(2.12) $$r = F_0 s.$$

A similar relation can be obtained along the other directions.

The time necessary for the particle to switch to another cell is obtained from a different form of equation (2.10):

(2.13) $$ds = \frac{dr}{F};$$

using the relation (2.9) we obtain $dF = \Delta F dr$ and then (2.13) is rewritten as:

(2.14) $$ds = \frac{dF}{(F\Delta F)}.$$

The crossing time in the zonal direction is obtained only if $F(1)$ and $F(0)$ have the same sign and $F \neq 0$ in the cell. The three-dimensional non-divergence of the velocity field for the grid cell ensures that at least one direction satisfies the former condition. The pseudo-time s is related to the transport F by:

$$s = \frac{1}{\Delta F} \ln\left(\frac{F}{F_0}\right) \tag{2.15}$$

or if $\Delta F = 0$, we have:

$$\Delta s = \frac{1}{F_0}. \tag{2.16}$$

The equation (2.15) is applied to compute the crossing pseudo-time in each direction (T_x, T_y, T_z), if $\Delta F \neq 0, \Delta G \neq 0, \Delta H \neq 0$:

$$T_x = \frac{1}{\Delta F} \ln\left(F - F_0\right);\ T_y = \frac{1}{\Delta G} \ln\left(G - G_0\right); T_z = \frac{1}{\Delta H} \ln\left(H - H_0\right); \tag{2.17}$$

the shortest time ($T = \min(T_x, T_y, T_z)$) defines the travelling time of the particle in the considered grid cell and the new particle position is computed using the value T as timestep:

$$x_{n+1} = x_n + \frac{F}{\Delta F}(\exp(\Delta F T) - 1); \tag{2.18}$$

$$y_{n+1} = y_n + \frac{G}{\Delta G}(\exp(\Delta G T) - 1); \tag{2.19}$$

$$z_{n+1} = z_n + \frac{H}{\Delta H}(\exp(\Delta H T) - 1). \tag{2.20}$$

The same computations are done for the next cell, with a starting point equal to the exit point of the previous one and the age of the particle is regularly updated.

2.5.2 TRACE Algorithm

The TRACE algorithm was written by Jarle Berntsen (Institute of Marine Research, Bergen-Nordnes, Norway) as a subroutine of the Princeton Ocean Model (POM; Blumberg and Mellor, 1987) and was published in Beletsky *et al*. (2007).

TRACE integrates the following Lagrangian equations:

$$\frac{dx_p}{dt} = u(x, y, z) \tag{2.21}$$

$$\frac{dy_p}{dt} = v(x, y, z) \tag{2.22}$$

where x_p, y_p are the positions of the particle; u and v are the horizontal components of the velocity and t is the time.

The particle position in the horizontal space is computed with an Euler forward scheme:

(2.23) $$x_p^{n+1} = x_p^n + u_p^n \Delta t$$

(2.24) $$y_p^{n+1} = y_p^n + v_p^n \Delta t$$

where the subscript p indicates the particle label, n is the current time step and Δt is the time interval. The values u_p^n, v_p^n are the zonal and meridional velocity for the current time step at the particle position; they are computed by linear interpolation of the horizontal currents provided by an external Eulerian model from the sides of the C-grid with the following expression (Figure 2.1):

(2.25) $$u_p^n = (1-m)u_{(i,j)} + mu_{(i+1,j)} \; ; \; v_p^n = (1-n)v_{(i,j)} + nv_{(i,j+1)}$$

Furthermore, the algorithm marks the particle as lost when it moves out of the domain of integration and prevents it from crossing the sea bottom or free surface. The algorithm also applies a linear interpolation in time to find the velocity values for the Lagrangian timestep.

This algorithm has been used for several studies, such as the circulation in southern Lake Michigan (Beletsky *et al*., 2006) and the transport of larval yellow perch in Lake Michigan (Beletsky *et al*., 2007).

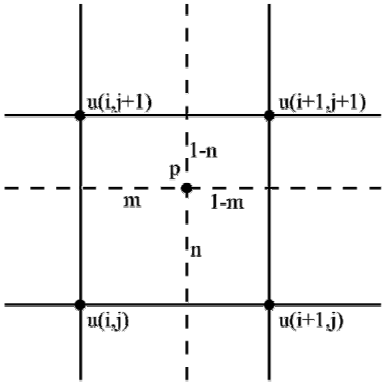

Figure 2.1 The position of the particle p relative to velocity grid points (u) in the linear and bilinear interpolation with the weighting factors m, n, (1-m) and (1-n).

2.5.3 SINCEM Algorithm

The SINCEM algorithm has been developed at the Laboratorio di Simulazione Numeriche del Clima e degli Ecosistemi Marini (SINCEM) of the University of Bologna to compute particle trajectories in a given velocity field; it has been written for terrain-following (sigma) and z-coordinate Eulerian models.

The Lagrangian horizontal particle motion is resolved applying an Euler forward scheme to the ordinary differential equations (2.21) (2.22), following the same methods as TRACE algorithm.

Unlike the previous code, the horizontal velocity values (u_p^n, v_p^n) at the particle location are computed applying a bilinear interpolation to the velocities surrounding the particle position x_p. Let particle p be located in the grid cell of Figure 2.1, and the velocity of the particle is determined from the equations:

$$u_p^n = (1-m)(1-n)u_{(i,j)} + m(1-n)u_{(i+1,j)} + mnu_{(i+1,j+1)} + (1-m)nu_{(i,j+1)} \qquad (2.26)$$

$$v_p^n = (1-m)(1-n)v_{(i,j)} + m(1-n)v_{(i+1,j)} + mnv_{(i+1,j+1)} + (1-m)nv_{(i,j+1)} \qquad (2.27)$$

As with TRACE, the algorithm uses a linear interpolation in time for the velocity values.

In this code the particles are prevented from crossing the bottom and the surface and they are labelled as lost when they reach the boundaries of the numerical domain.

2.5.4 SINCEM2 Algorithm

The final algorithm considered is SINCEM2, developed at the SINCEM laboratory of University of Bologna. This algorithm adopts the same principles as SINCEM for time and space interpolation but uses a different time integration scheme for the particle position.

The numerical time stepping scheme is the fourth-order Runge-Kutta integration method (RK4) that approximates the solutions of ordinary differential equations with an iterative method.

In particular, the integration of the function is carried out by computing four intermediate points called the 'Runge-Kutta coefficients', for direction x, expressed as:

(2.28) $$k_1 = \Delta t * u(t^n, x_p^n)$$

(2.29) $$k_2 = \Delta t * u(t^n + \frac{1}{2}\Delta t, x_p^n + \frac{1}{2}k_1)$$

(2.30) $$k_3 = \Delta t * u(t^n + \frac{1}{2}\Delta t, x_p^n + \frac{1}{2}k_2)$$

(2.31) $$k_4 = \Delta t * u(t^n + \Delta t, x_p^n + k_3)$$

where u is the zonal velocity component, Δt is the time step and x_p^n is the location of the particle at the time t^n. The algebraic derivation of this method is obtained starting from a Taylor-series expansion.

The final position of the particle is predicted with the following expression:

(2.32) $$x_p^{n+1} = x_p^n + \frac{k_1}{6} + \frac{k_2}{3} + \frac{k_3}{3} + \frac{k_4}{6}.$$

Similar relationships are obtained for the other directions.

The algorithm uses a linear time interpolation to find the Eulerian velocity field at the current time step and the same control is applied to the particle position close to the boundary of the computational domain.

2.5.5 Lagrangian diffusion parameterizations

The diffusion coefficients for the Langevin equation (2.7) are added to each of the four algorithms used to compute the advective components of the same equation. At each timestep we add a diffusive motion gave by:

(2.33) $$\sqrt{2D_x}Z_1\sqrt{dt} = [2ran(0,1) - 1]\sqrt{2K_H\Delta t}$$

(2.34) $$\sqrt{2D_y}Z_2\sqrt{dt} = [2ran(0,1) - 1]\sqrt{2K_H\Delta t}$$

(2.35) $$\sqrt{2D_z}Z_3\sqrt{dt} = [2ran(0,1) - 1]\sqrt{2K_V\Delta t}$$

where K_H and K_V are the horizontal and vertical diffusivities coefficients respectively, Δt is the Lagrangian timestep and $ran(0,1)$ represents a random number with uniform distribution in the interval 0 and 1.

The random number generator used is the routine RAN1 described by Press *et al*. (1986).

2.6 Validation of Lagrangian numerical schemes

The Lagrangian particle-tracking algorithms, introduced above, have been tested on two particular solution of the Eulerian equation of motion: inertial oscillations and the Stommel solution.

2.6.1 Inertial motion

The response of the ocean surface to an impulse like a wind blowing for a few hours at the surface of the sea is composed of inertial oscillations.

The water starts to accelerate under the influence of the Coriolis force following the non-advective and non-diffusive equation of motion:

$$\frac{\partial u}{\partial t} - fv = 0 \tag{2.36}$$

$$\frac{\partial v}{\partial t} + fu = 0\,. \tag{2.37}$$

The solutions of these differential equations are:

$$u = u_0 \cos(ft) \tag{2.38}$$

$$v = -u_0 \sin(ft) \tag{2.39}$$

with the initial condition that $u\big|_{t=0} = (u_0, 0)$.

This current is called an inertial current or inertial oscillation.

The water particle trajectory in this velocity field is obtained integrating $\frac{dx}{dt} = u$;

$\frac{dy}{dt} = v$.

The solution is:

(2.40) $$x = x_0 + \frac{u_0}{f}\sin(ft)$$

(2.41) $$y = y_0 - \frac{u_0}{f}(1-\cos(ft))$$

with $\vec{x} = (x_0, y_0)$ at $t = 0$.

The particle then describes an inertial circle with constant radius $r = u_0 / f$.

Taking a further step, we consider a geostrophic current (u_g) superimposed and the equations become:

(2.42) $$\frac{\partial u}{\partial t} - fv = 0$$

(2.43) $$\frac{\partial v}{\partial t} + fu = fu_g .$$

The solutions are:

(2.44) $$u = u_g + (u_0 - u_g)\cos(ft)$$

(2.45) $$v = -(u_0 - u_g)\sin(ft) .$$

For this velocity field, the particle trajectory is:

(2.46) $$x = x_0 + u_g t + \frac{(u_0 - u_g)}{f}\sin(ft)$$

(2.47) $$y = y_0 - \frac{(u_0 - u_g)}{f}(1-\cos(ft)) .$$

The oscillation radius is now proportional to the difference between initial and geostrophic velocity:

(2.48) $$r = \frac{(u_0 - u_g)}{f} .$$

In the third and last case study we also introduce the dissipative effects represented by the viscosity term into the equations of motion:

(2.49) $$\frac{\partial u}{\partial t} - fv = -\gamma u$$

$$\frac{\partial v}{\partial t} + fu = -\gamma v + fu_g \tag{2.50}$$

The solutions are now:

$$u = u_g e^{-\gamma_g t} + (u_0 - u_g) e^{-\gamma t} \cos(ft) \tag{2.51}$$

$$v = -(u_0 - u_g) e^{-\gamma t} \sin(ft). \tag{2.52}$$

The equations of the particle trajectory are:

$$x = x_0 + \frac{u_g}{\gamma_g}(1 - e^{-\gamma_g t}) + \frac{(u_0 - u_g) f}{f^2 + \gamma^2}\left[\frac{\gamma}{f} + e^{-\gamma t}\left(\sin(ft) - \frac{\gamma}{f}\cos(ft)\right)\right] \tag{2.53}$$

$$y = y_0 - \frac{(u_0 - u_g) f}{f^2 + \gamma^2}\left[1 - e^{-\gamma t}\left(\cos(ft) + \frac{\gamma}{f}\sin(ft)\right)\right]. \tag{2.54}$$

The water particle describes circles with a drift to the East due to geostrophic velocity and with a decreasing oscillation radius depending on γ:

$$r = \frac{(u_0 + U_g) f}{f^2 + \gamma^2}. \tag{2.55}$$

These three approximations of the inertial motion have been used to test and to validate the particle-tracking algorithms.

In the three different experiments, we have imposed the Eulerian motion given by equations (2.38) and (2.39), (2.44) and (2.45), (2.51) and (2.52).

We then used the ARIANE, TRACE, SINCEM and SINCEM2 algorithms to deduce the particle trajectory and a comparison was made with the analytical solutions of equations (2.40) and (2.41), (2.46) and (2.47), (2.53) and (2.54).

For the first experiment we consider a parcel at the latitude of 45° with an initial $u_0 = 0.3 m/s$.

The particle motion is simulated with the four different Lagrangian schemes for two days using an integration timestep of $\Delta t = 180$ seconds and $dx = dy = 250m$.

The results are shown in Figure 2.2; the particle trajectory obtained with the four algorithms describes a circle in agreement with the analytical solution.

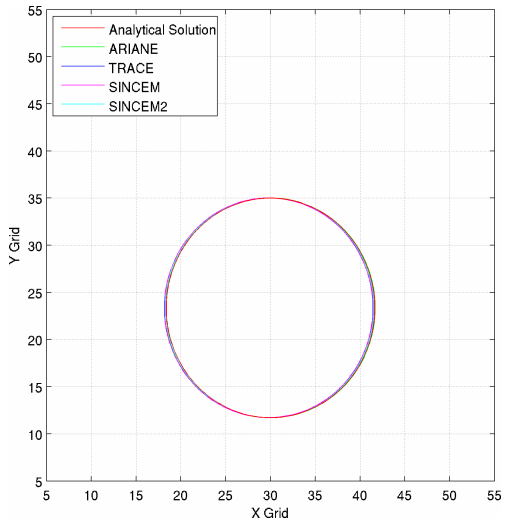

Figure 2.2 Analytical solution of the inertial motion (red line) superimposed on numerical particle trajectories computed with ARIANE (green line), TRACE (blue line), SINCEM (magenta line) and SINCEM2 (cyan line).

The second case study was carried out with two different sets of parameters: (1) $u_0 = 0.3m/s$ superimposed on an initial geostrophic flow $u_g = 0.04m/s$ and (2) $u_0 = 0.05m/s$ and $u_g = 0.1m/s$.

For the Lagrangian simulation we used a timestep of 180 seconds and $dx = dy = 250m$. The results are shown in Figure 2.3A,B for both experiments. The trajectories reproduce the analytical solution accurately except for ARIANE for the case $u_0 > u_g$ (Figure 2.3A).

In the last experiment we used $u_0 = 0.3m/s$, $u_g = 0.04m/s$ and a damping time of $t_d = 1/\gamma = 2.89days$ and $t_g = 1/\gamma_g = 28.9days$ with $\Delta t = 180s$. Figure 2.4 illustrates the numerical trajectories compared with the analytical solution: once again, ARIANE is the least accurate of the schemes.

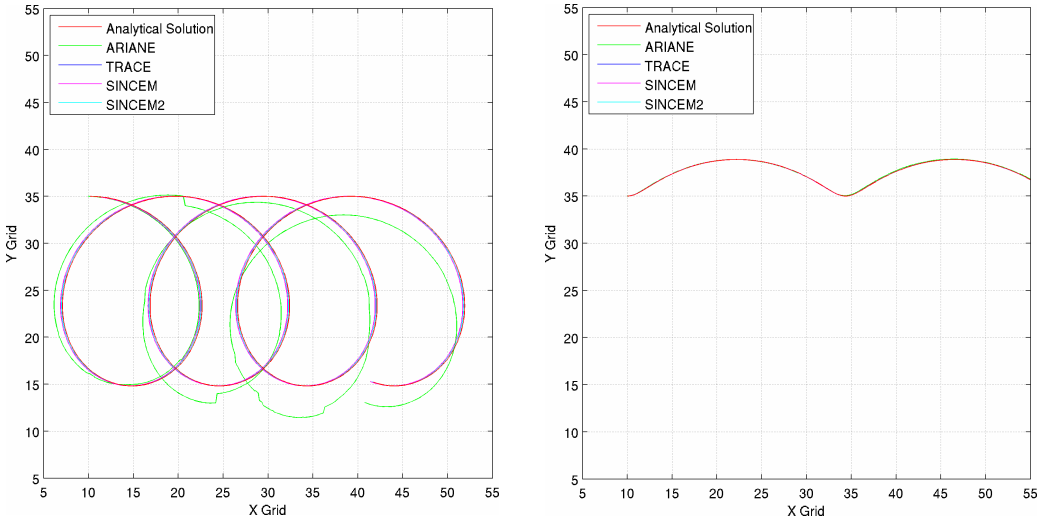

Figure 2.3 Particle trajectories simulated with ARIANE, TRACE, SINCEM and SINCEM2 superimposed on inertial oscillation for: (A) initial velocity value higher than geostrophic velocity and (B) initial velocity value lower than geostrophic velocity.

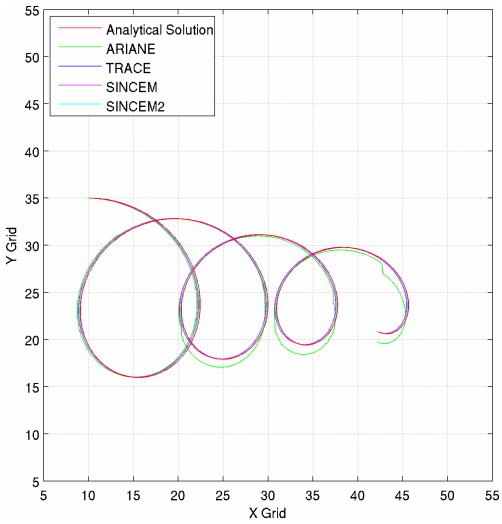

Figure 2.4 Analytical solution of the inertial motion (red line) for the third study case superimposed on numerical particle trajectories simulated with ARIANE (green line), TRACE (blue line), SINCEM (magenta line) and SINCEM2 (cyan line).

2.6.2 The Stommel solution

The Stommel steady-state solution for the stream function ψ is obtained integrating the Stommel (1948) equation:

(2.56) $$r\nabla^2\psi + \beta\psi_x = -\frac{\tau_0\pi}{\rho_0 D_0 b}\sin\left(\frac{\pi y}{b}\right)$$

where a zonal wind stress $\tau^x = -\tau_0 \cos\left(\frac{\pi y}{b}\right)$ has been used.

The boundary conditions are $\psi = 0$ at $x = 0, a$; and $y = 0, b$.

In equation (2.56) the parameter r is the inverse time scale characterizing damping by bottom friction and β represents the latitudinal variation of the Coriolis parameter (f), $\beta = df/dy$.

The analytical solution of (2.56) is:

(2.57) $$\psi = (1 - e^{-x/\varepsilon_S} - x)\pi\sin(\pi y)$$

where ε_S is the thickness of the Western boundary layer: $\varepsilon_S = r/(\beta a) << 1$. A detailed mathematical description of this solution can be found in Pedlosky (1987).

The Eulerian velocity field is obtained from (2.57) by taking:

(2.58) $$u = -\frac{\partial\psi}{\partial y}\ ;\ v = \frac{\partial\psi}{\partial x}$$

The analytical Stommel solution has been used to validate the particle-tracking algorithms introduced above. The validation was only carried out for TRACE and SINCEM.

The numerical values used to apply the Stommel solution are:

$$a = 10000m\ ;\ b = 10000m\ ;\ D_0 = 200m\ ;\ day = 11.6$$

$$\beta = 2x10 - 11(ms)^{-1}\ ;\ r = 1/(dayx86400)\,s^{-1};$$

Figure 2.5A.B shows the stream function (ψ) superimposed on the particle trajectories advected with the analytical solution (2.58) using the SINCEM and TRACE schemes. The trajectories for both cases reproduce a reasonable trajectory solution but they are different and further study will be needed to say why.

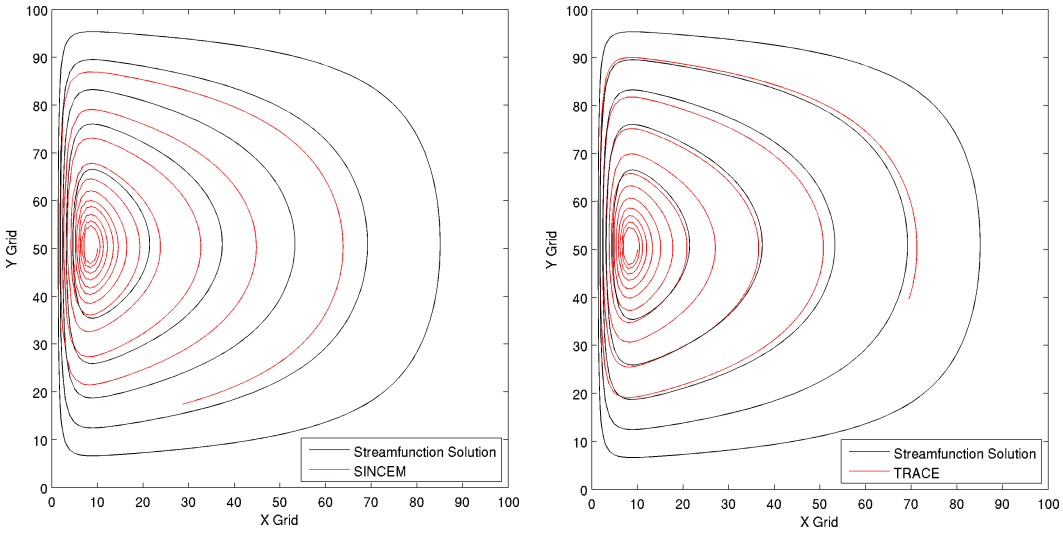

(A) **(B)**

Figure 2.5 Ocean streamlines of the Stommel model solution (black line) that show a strong Western boundary current superimposed on numerical trajectories simulated with the SINCEM (A) and TRACE (B) algorithms (red line).

2.7 Sensitivity of Lagrangian numerical schemes to time resolution of the Eulerian field

There are several factors that affect the accuracy of the trajectory simulation. In this chapter we consider the time resolution of the Eulerian field and the Lagrangian timestep used in the different algorithms, (ARIANE, TRACE, SINCEM and SINCEM2).

In the next following sections we will illustrate the results of the sensitivity experiments performed.

2.7.1 Description of the Lagrangian experiments

The Lagrangian experiments were carried out in the Adriatic Sea ([39°-46° N, 12°-21°E]) where a cluster of 8977 particles was released evenly a distance of 5km from each other. The Eulerian current field is provided by a model solution based on the Princeton Ocean Model (POM, Blumberg and Mellor, 1987), implemented first by Zavatarelli and Pinardi (2003) and Oddo *et al*. (2006). The model has been implemented on a regular latitude and longitude grid with

approximately 5km of horizontal resolution and 21 vertical sigma layers and the minimum depth has been set to 10m.

We performed a total of 19 Lagrangian sensitivity experiments, the parameters of which are summarized in Table 2.2. For each experiment the particles have been integrated for 13 days using the four particle-tracking algorithms: ARIANE, TRACE, SINCEM, SINCEM2.

The Experiment 1 is considered as the reference case (the 'true case') against which all other experiments (Experiments 2-19) are compared; the integration is carried out with the Eulerian current at the highest time resolution of 600 seconds (the Eulerian model time step) using the four numerical schemes.

Experiments 2-11 are performed using daily mean current fields and with variable Lagrangian timesteps ($\Delta t = 600$, 1800, 3600, 7200, 10800, 14400, 21600, 28800, 43200, 86400 seconds). Experiments 12-16 use 3-hour mean velocity fields and $\Delta t = 600$, 1800, 3600, 7200, 10800 seconds. The last set, Experiments 17-19, have been carried out with hourly mean fields and $\Delta t = 600$, 1800, 3600 seconds.

Furthermore, Experiments 2-19 have been carried out under three different conditions:

- CASE1: activating only the deterministic component in the Lagrangian model;
- CASE2: also introducing the stochastic component;
- CASE3: using snapshot instead of mean current fields.

Experiment performance is evaluated computing the distance between predicted particle position and reference case particle position.

2.7.2 Definition of the numerical error

The behaviour of the Lagrangian algorithms with respect to the time frequency of the Eulerian field and the integration time step has been valuated comparing the particle positions of the reference experiment (Experiment 1) with the other simulations (Experiments 2-19).

Experiment N°	Temporal resolution of Eulerian field	Lagrangian Time step (Δt) (Seconds)
1	600 seconds	600
2	Daily mean	600
3		1800
4		3600
5		7200
6		10800
7		14400
8		21600
9		28800
10		43200
11		86400
12	3-hour mean	600
13		1800
14		3600
15		7200
16		10800
17	Hourly mean	600
18		1800
19		3600

Table 2.2 Summary of the Lagrangian sensitivity experiments.

The comparison is carried out through ensemble averages of the difference between the positions of reference and test trajectories; the statistical behaviour of an ensemble of Lagrangian trajectories is more relevant than the trajectories of each fluid parcel.

To quantify the Lagrangian sensitivity two error statistics are introduced: the absolute error $\langle e_a \rangle$ and total error $\langle e_t \rangle$; the brackets define ensemble average over all particle trajectories.

The absolute numerical error defines the average distance between particle positions from reference and perturbed experiments at a given travel time:

$$\langle e_a(n\Delta t) \rangle = \frac{1}{NP} \sum_{p=1}^{NP} \left| r_{ref}^{\,p}(n\Delta t) - r^{\,p}(n\Delta t) \right| \tag{2.59}$$

where r_{ref} and r represent either the zonal, meridional or vertical positions of the reference and test trajectories respectively; superscript p is the particle label

($p = 1,..., NP$) with $NP = 8977$; Δt is the trajectory integration time step, and n identifies the time step number.

The total numerical error represents the total distance between the positions of the reference and test experiment averages in space and time:

$$\langle e_t \rangle = \frac{1}{T} \sum_{n=1}^{T} \left(\langle e_a (n\Delta t) \rangle \right) \tag{2.60}$$

where T is the total number of the integration time steps ($T = n\Delta t$). This total error measured in kilometres gives a first evaluation of the accuracy of the trajectory simulation for 13 days.

2.7.3 Result

2.7.3.1 CASE1

For CASE1 simulations 2-19 have been carried out with only the deterministic component in the particle-tracking algorithms.

The absolute error curves are shown as a function of days and the time frequency of the current field in Figure 2.6, Figure 2.7 and Figure 2.8 (Panels A,B,C and D). The different colours of the curves indicate the experiments obtained with diverse Lagrangian time steps (Δt). The absolute error is considered acceptable if it is less than 5 km of the horizontal resolution of the Eulerian model.

Common behaviour is that $\langle e_a \rangle$ increases with time whatever the temporal frequency of the Eulerian current, Δt and numerical integration scheme. Furthermore, we notice that $\langle e_a \rangle$ decreases with high temporal frequency of the current field, using hourly mean velocity the $\langle e_a \rangle$ is less than 5 km at 13 days of integration (Figure 2.8).

For TRACE, SINCEM and SINCEM2 (Figure 2.6, Figure 2.7 and Figure 2.8 panels B,C,D), $\langle e_a \rangle$ is also correlated to the Lagrangian timestep; better results are achieved with small timestep ($\Delta t = 600$ seconds) and high $\langle e_a \rangle$ corresponds with experiments with larger Δt. TRACE and SINCEM algorithms, which use

both an Euler forward scheme, show similar absolute error curves. $\langle e_a \rangle$ decreases significantly increasing the time frequency of the Eulerian field and decreasing the Δt. On the contrary, ARIANE shows anomalies in behaviour, insofar as $\langle e_a \rangle$ decreases with high Δt, and the relation between absolute error and Lagrangian timestep is non-linear. With daily mean currents (Figure 2.6A) low error values are obtained with $\Delta t = 86400s$ (1 day); with 3-hours mean (Figure 2.7A) the better result is with $\Delta t = 10800s$ (3 hours) and finally with an hourly mean (Figure 2.8A) the optimal is with $\Delta t = 3600s$ (1 hour). Probably this is due to the assumptions made in writing the ARIANE equations, which we have already partially discussed in this chapter. SINCEM2 (Figure 2.6, Figure 2.7 and Figure 2.8D) represents the most accurate algorithm, giving the lowest $\langle e_a \rangle$ values. Similar general conclusions can be derived from the figures of the total error $\langle e_t \rangle$ (Figure 2.9A,B,C,D). We observe that:

- Eulerian field at high time frequency resolution improves the trajectory simulation; hourly field and 3-hour field give better results than daily mean currents;
- For TRACE, SINCEM and SINCEM2, the trajectory simulation also depends on Lagrangian timestep. Small Δt decreases the total error.
- ARIANE shows a non-linear relationship between $\langle e_t \rangle$ and Δt.

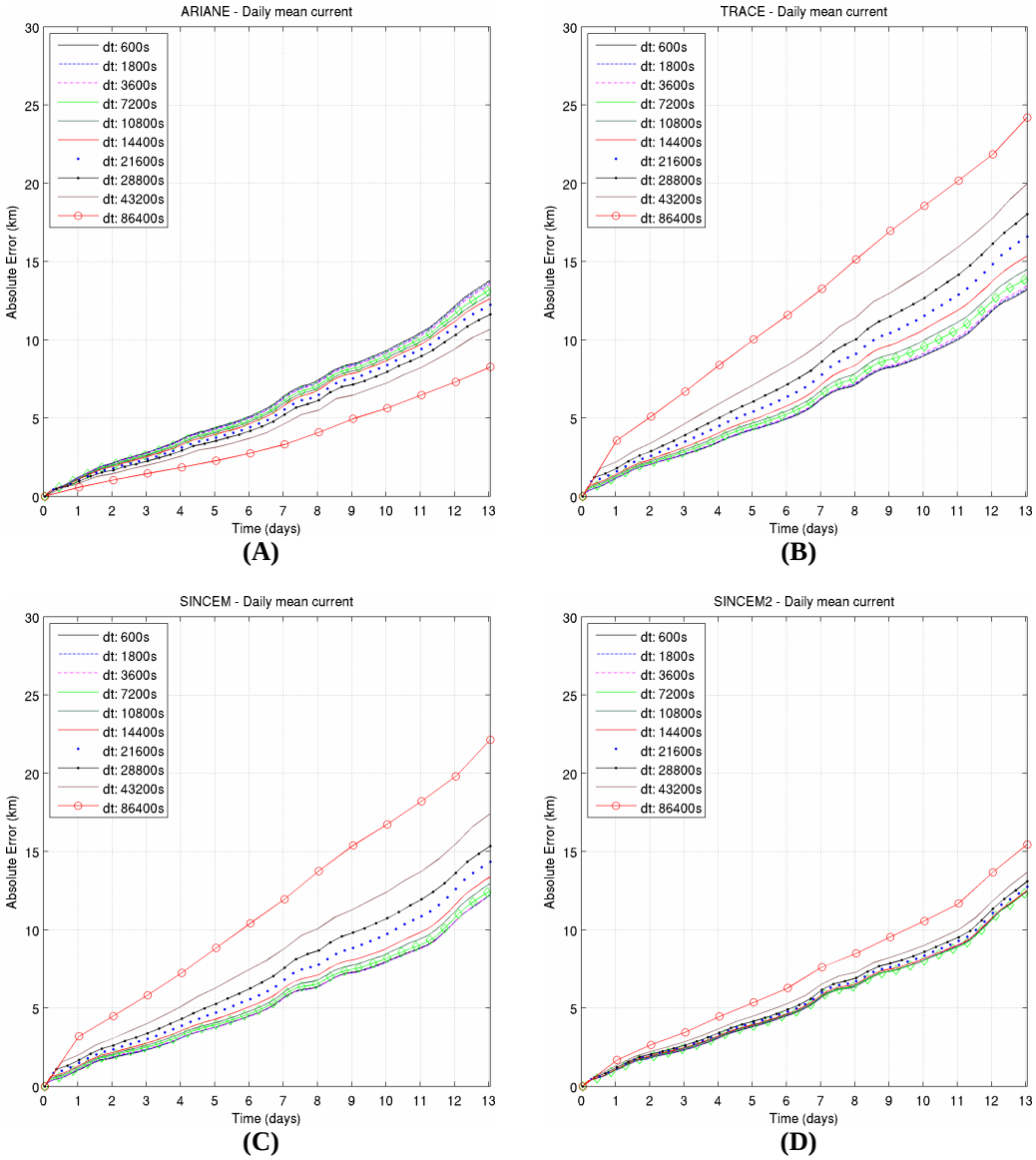

Figure 2.6 CASE1. Absolute error (km) for trajectories for Experiments 2-11 against simulation time (days), using daily mean current field for: ARIANE (A), TRACE (B), SINCEM (C) and SINCEM2 (D) algorithms.

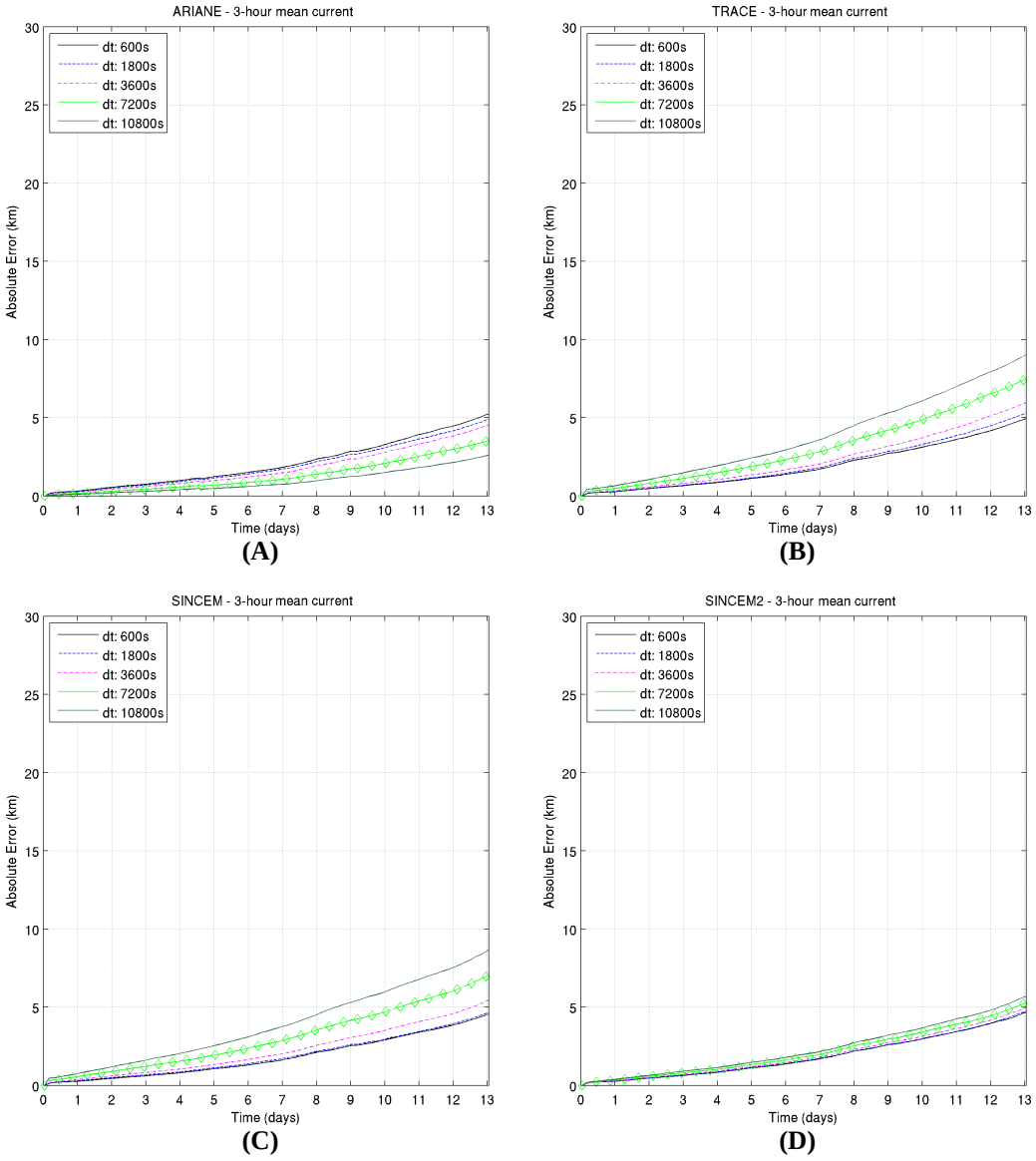

Figure 2.7 CASE1. Absolute error (km) for trajectories for Experiments 12-16 against simulation time (days), using 3-hour mean current field for: ARIANE (A), TRACE (B), SINCEM (C) and SINCEM2 (D) algorithms.

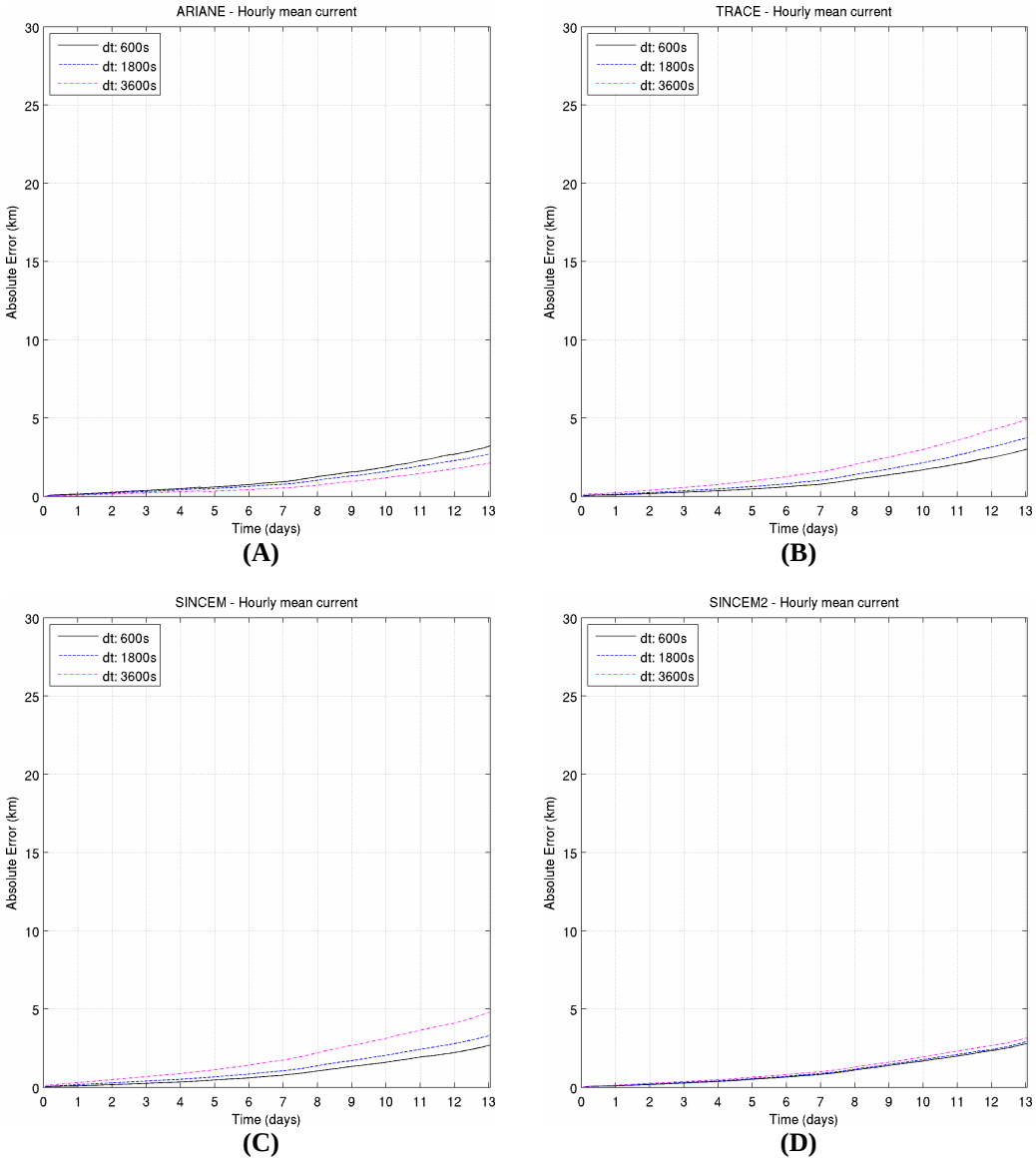

Figure 2.8 CASE1. Absolute error (km) for trajectories for Experiments 17-19 against simulation time (days), using hourly mean current field for: ARIANE (A), TRACE (B), SINCEM (C) and SINCEM2 (D) algorithms.

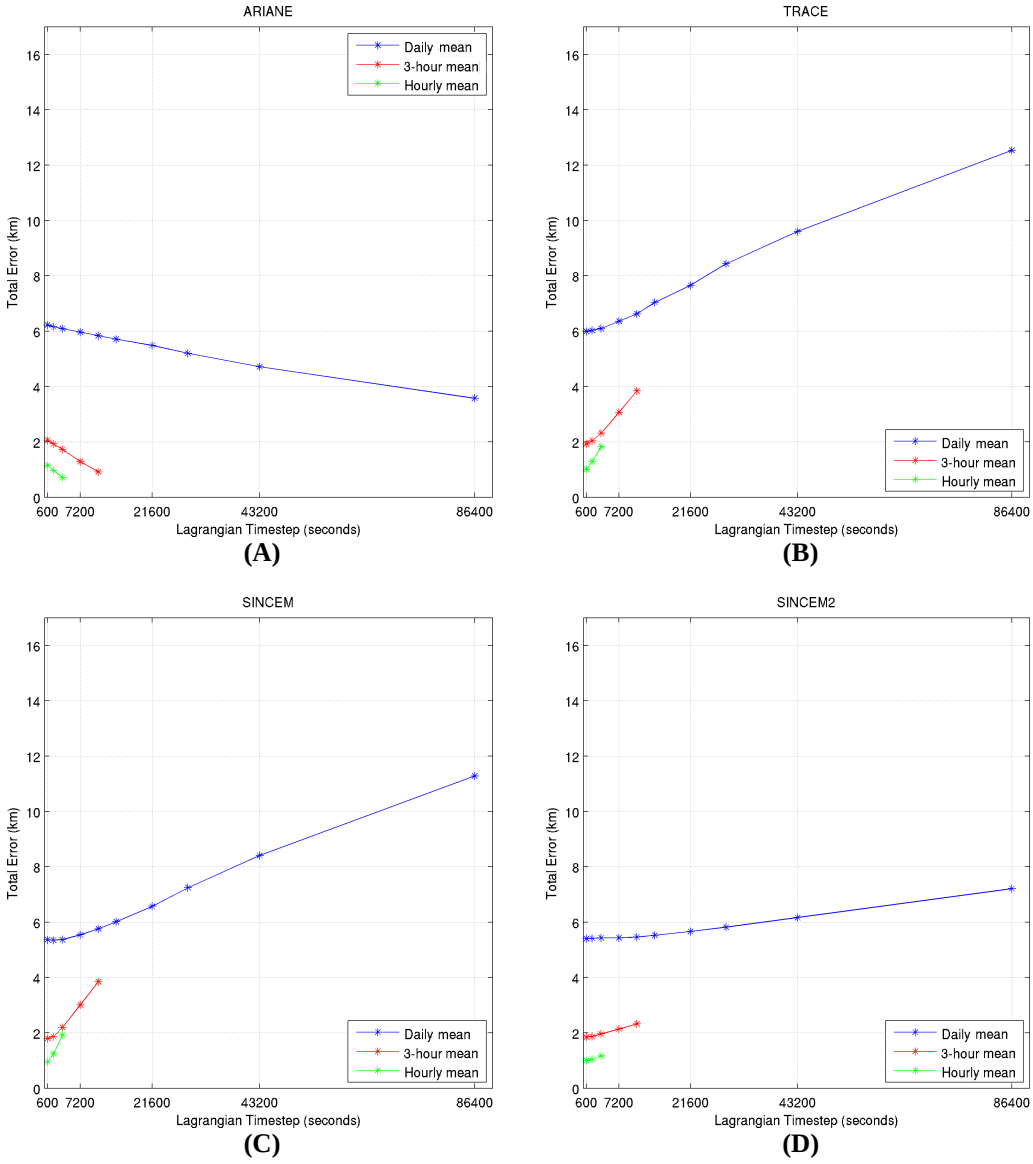

Figure 2.9 CASE1. Total error values (km) for Experiments 1-19 against Lagrangian timestep (seconds), for: ARIANE (A), TRACE (B), SINCEM (C) and SINCEM2 (D) algorithms. The different coloured lines refer to experiments with diverse temporal frequency currents.

2.7.3.2 CASE2

For CASE2 the Lagrangian simulations 2-19 have been carried out with the deterministic and diffusive component in the different algorithms (with $K_H = 20m^2/s$) and in the reference experiment too (Experiment1) we introduce the turbulence part. We show only the figure of the total error ($\langle e_t \rangle$) as a function of Lagrangian timestep and frequency of the Eulerian field (Figure 2.10 A,B,C,D). For TRACE, SINCEM and SINCEM2 the average $\langle e_t \rangle$ increases with high Lagrangian Δt and low temporal resolution of the Eulerian velocity field (Figure 2.10 B,C,D). The results obtained with hourly mean velocity (green line) are very similar to results computed with the 3-hour mean (red line). For the ARIANE experiment we note the same non-linear behaviour observed in CASE1. Comparing CASE2 (Figure 2.10) with CASE1 (Figure 2.9), we notice that the introduction of the stochastic component, of random motion, in the Lagrangian model makes the experiment less consistent and determine an enhancement of $\langle e_t \rangle$.

The $\langle e_t \rangle$ trend depends on the choice of the diffusion coefficients (K_H); for high value of the coefficients $\langle e_t \rangle$ increases substantially; the correction diffusion term dominates the mean flow velocity (not shown).

2.7.3.3 CASE3

In these final experiments the particles have been advected with current snapshots instead of average velocities, and always have the same frequency: daily, 3-hour and hourly. The results are shown in Figure 2.11 A,B,C,D.

Analyzing the results, we can detect the same performances seen in CASE1. The Eulerian field at high temporal resolution improves the prediction; in TRACE and SINCEM algorithms the total error is strongly related to Δt; the SINCEM2 scheme is less influenced by the Lagrangian timestep and ARIANE shows different trends. Furthermore, comparing these results (Figure 2.11) with the results of CASE1 (Figure 2.9), we notice that the $\langle e_t \rangle$ are higher. Thus the

particle advection with snapshots of current fields reduces the predictability of the Lagrangian trajectories with respect to a true field calculated by the snapshots themselves.

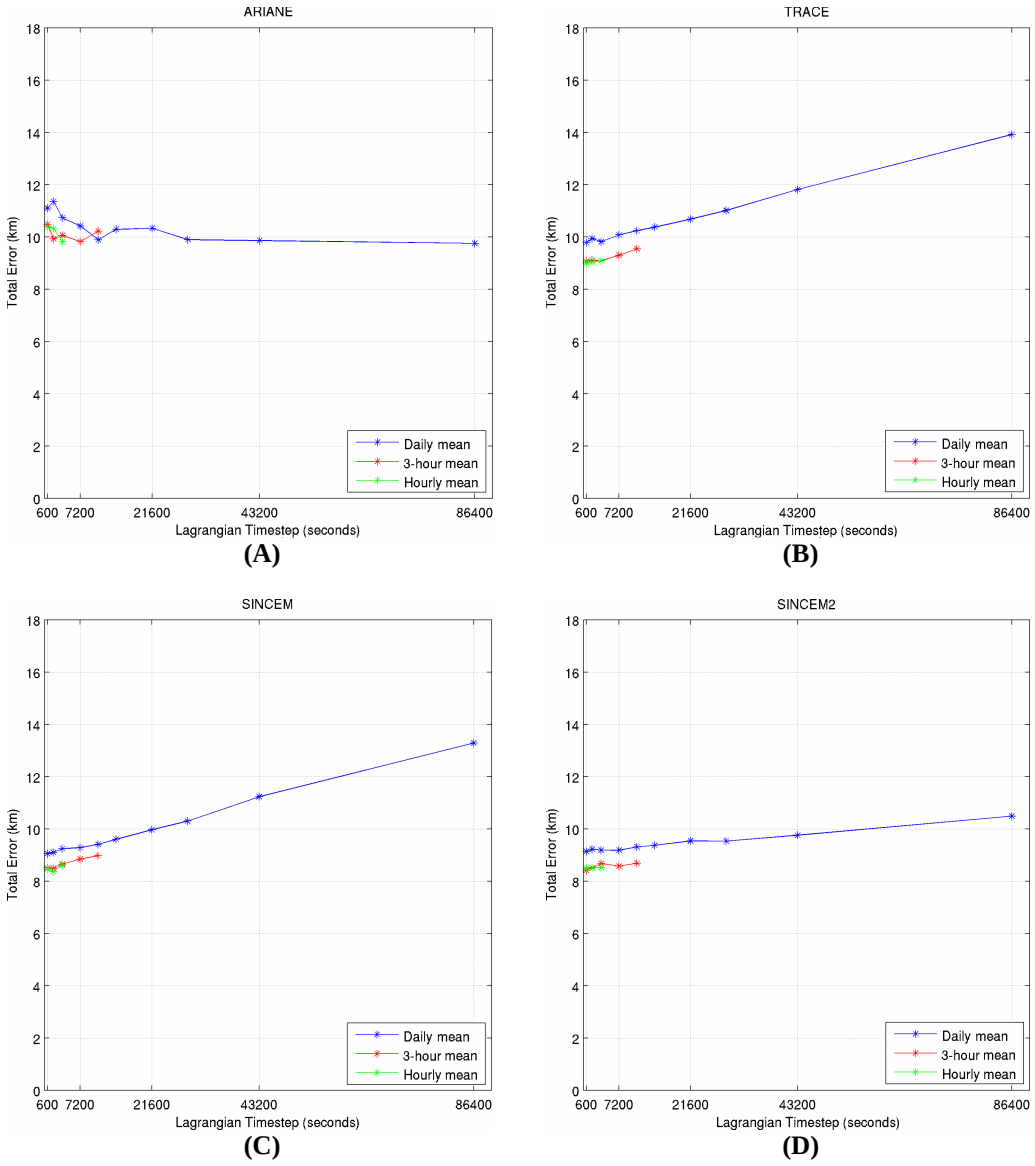

Figure 2.10 CASE2. Total error values (km) for Experiments 1-19 against Lagrangian timestep (seconds), for: ARIANE (A), TRACE (B), SINCEM (C) and SINCEM2 (D) algorithms. The different coloured lines refer to experiments with diverse temporal frequency currents.

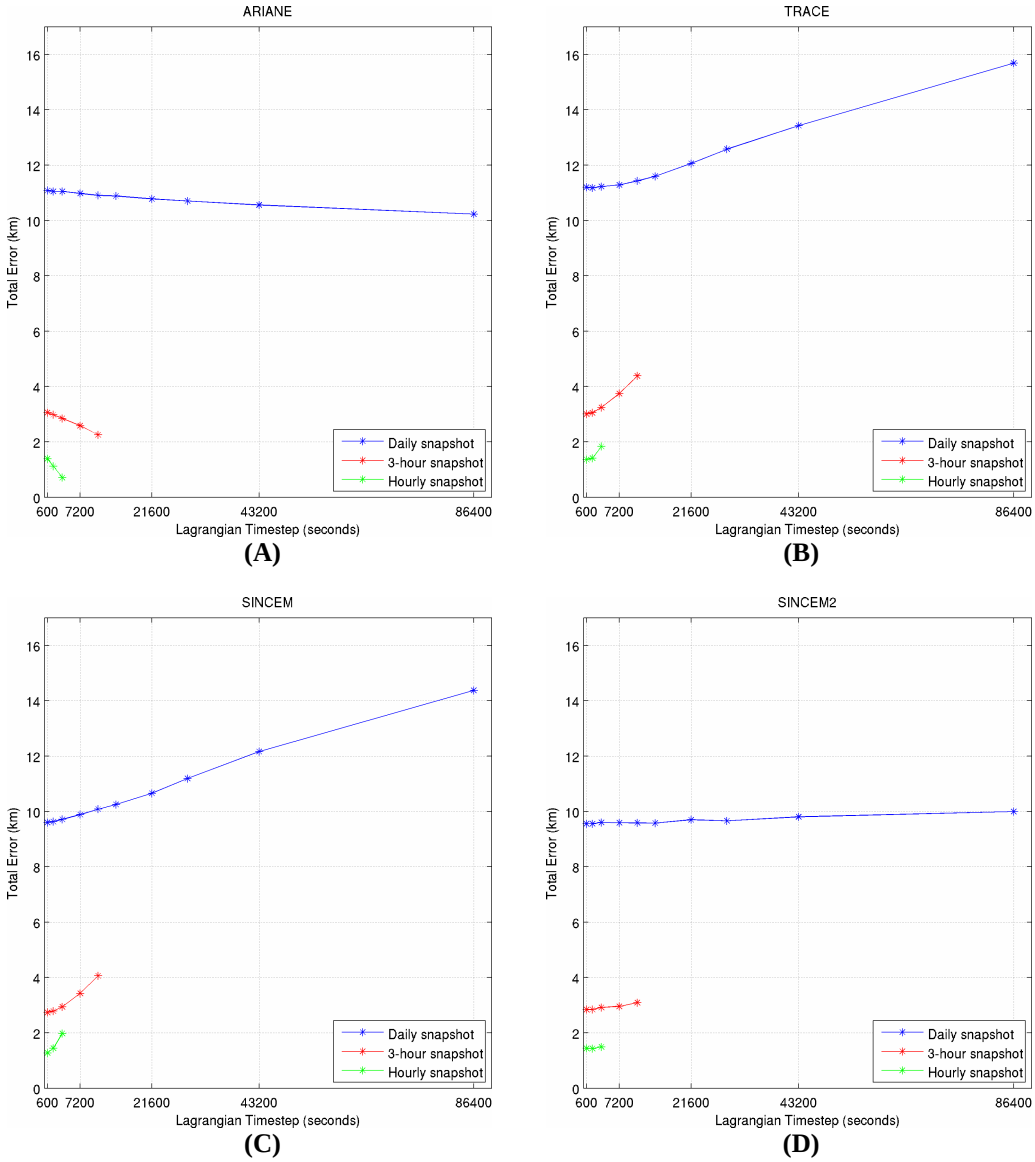

Figure 2.11 CASE3. Total error values (km) for Experiments 1-19 against Lagrangian timestep (seconds), for: ARIANE (A), TRACE (B), SINCEM (C) and SINCEM2 (D) algorithms. The different coloured lines refer to experiments with different temporal frequency currents snapshots.

2.8 Summary and Conclusions

In this chapter we have studied the different algorithms used in particle tracking from Eulerian velocity fields. Different methods to resolve the Lagrangian advection-diffusion equations have been analyzed. The Lagrangian particle trajectories are coupled with the advection field provided by an external Eulerian circulation model and a random-walk scheme is used to simulate diffusive processes.

Four different numerical schemes have been proposed and they have been validated comparing them with analytical solutions. To apply these schemes to the numerical simulations of particle trajectories in realistic ocean system solutions we have analyzed the algorithms as a function of time frequency of the Eulerian field and the Lagrangian timestep.

A set of sensitivity experiments have been performed in the Adriatic Sea. The Lagrangian predictability is strongly affected by the temporal resolution of the Eulerian field; accurate predictions are provided with high resolved velocity datasets. The Lagrangian timestep is a function of the Eulerian frequency; for hourly mean velocity the optimal value of the Lagrangian timestep is 1 hour. Furthermore, Eulerian average current fields provide smaller errors than for snapshots. The diffusive component of the trajectory equation introduces uncertainties in the particle prediction that could decrease the simulation accuracy noticeably.

Finally, out of the four algorithms tested, the most accurate scheme is SINCEM2 using a Runge-Kutta scheme and SINCEM with an Euler forward scheme. Both use a bilinear spatial interpolation scheme and time interpolation for the Eulerian velocity field.

Chapter 3

Numerical Trajectory Comparison with Drifter Data in the Adriatic Sea

3.1 Introduction

The first step for the development of Lagrangian dispersion applications is the estimation of a generic predictability for Lagrangian trajectories in realistic Eulerian flow field simulations.

This present study is one of the recent attempts to quantify the Lagrangian predictability in the ocean using real drifter data; the goal is to provide error estimates for particle trajectories.

This work has been carried out in collaboration with Dr Pierre-Marie Poulain of the National Institute of Oceanography and Experimental Geophysics (OGS), Trieste. Eulerian and Lagrangian comparisons have been performed between drifter data, deployed in the Adriatic Sea as part of the Dynamics of Localized Currents and Eddy Variability in the Adriatic (DOLCEVITA) project, and numerical trajectories simulated with the Lagrangian model one-way coupled with the Adriatic Forecasting System operational model (Oddo *et al*., 2007).

The Adriatic Sea is a semi-enclosed sub-basin of the Mediterranean Sea (Figure 3.1). It extends northwest from 40° to 45° 45'N with a length of about 770 km and a mean width of about 160 km; it communicates at the south with the Ionian Sea

through the Strait of Otranto. The Northern part of the basin is characterized by very shallow water with gently sloping bathymetry with an average bottom depth of about 35 metres. The central part is 140 m deep on average, with two small bottom depressions (the so-called 'Pomo' or 'Jacuba' Pits) having a maximum depth of 250 m. The southern part is characterized by a wide depression deeper than 1100 m.

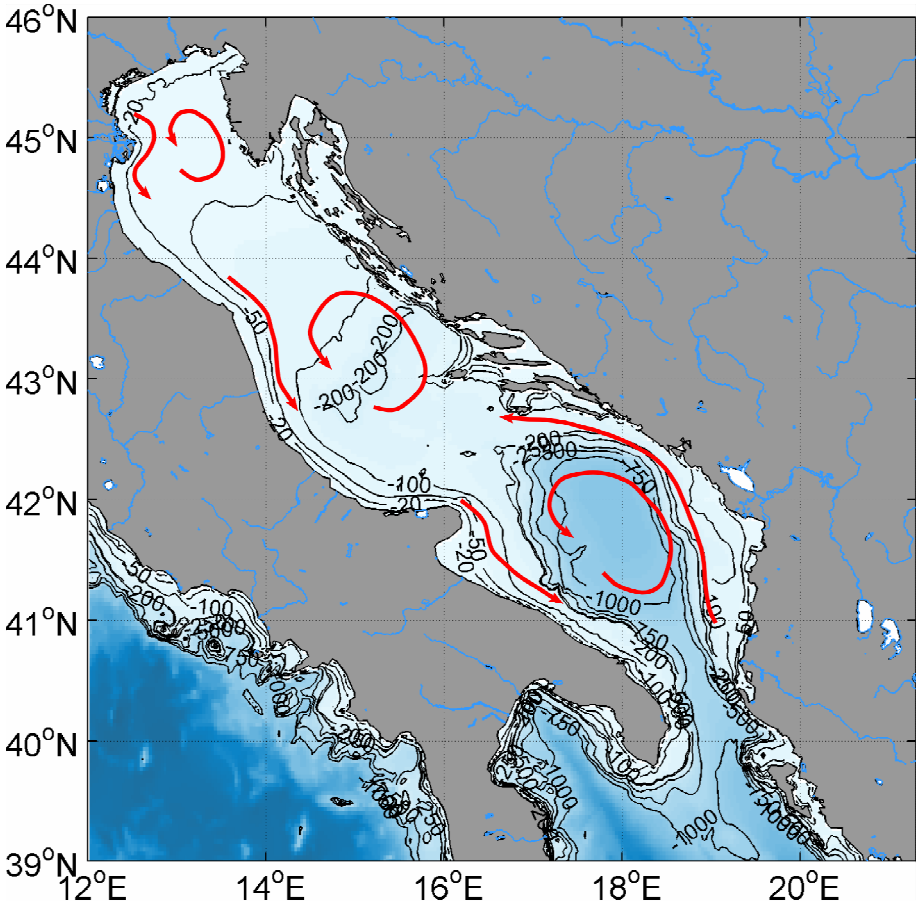

Figure 3.1 Bathymetry of the Adriatic Sea (the depth is given in metres) and schematic map of the circulation.

The two major wind regimes affecting the Adriatic basin are the so-called "Bora" (NEE) and "Scirocco" (SE). The Bora blows during the winter, affecting particularly the northern Adriatic with intense episodic events, while the Scirocco blows mainly in spring and autumn. The Adriatic Sea shows a significant net fresh water gain determined by the strong river runoff contribution (Raicich, 1996); the

larger river is the Po, located in the Northern part of the basin, having an average runoff of about 1500 m^3/s. Despite the large fresh water input, the Adriatic Sea is a site of dense water formation that occurs at two distinct locations: in the shallow northern Adriatic (Artegiani *et al*., 1989) and in the deeper southern Adriatic (Ovchinnikov *et al*., 1987; Manca *et al*., 2001).

The climatological circulation is characterized by well-known current and gyre structures (Artegiani *et al*. (1997a,b), Poulain (2001), Zavatarelli *et al*. (2002), Zavatarelli and Pinardi (2003)). The circulation (Figure 3.1) is generally cyclonic, with three main cyclonic gyres located in the southern, central and northern sub-basin, named, respectively, by Artegiani *et al*. (1997b) Southern, Middle and Northern Adriatic gyres. The three cells are interconnected with seasonally varying characteristics by two coastal currents: the Western Adriatic Coastal Current (WACC) and the Eastern Southern Adriatic Current (ESAC). The WACC flows southward along the western coast from the Po river delta to the Otranto Strait; the ESAC flows northward from the Otranto Strait along the eastern coast and reaches the central Adriatic sub-basin.

Section 2 gives a general description of the data used in this study and a brief review of the numerical models applied. Section 3 shows the Eulerian statistic of the drifter data set and modelled velocity field. The result of Lagrangian comparison and the estimation of the prediction uncertainty are given in Section 4. Summary and conclusions follow in Section 5.

3.2 Data and methods

3.2.1 Drifter data

The observations derive from the surface drifters deployed in the Northern and Central Adriatic between September 2002 and March 2004. A total of 124 drifting buoys were launched during the international DOLCEVITA project, corresponding to 188 deployments because some drifters were recovered and redeployed several times. The main objective of the DOLCEVITA project was to

quantify the kinematic and dynamic properties of the northern and middle Adriatic Sea and to define the mesoscale variability with special attention to coastal Italian current.

Two versions of the CODE drifters (Davis, 1985; Poulain, 1999, 2001) are used, with ARGOS telemetry and GPS systems which permit a finer resolution in space (~10 m) and time (Barbanti *et al*., 2005) to be obtained. The position sampling for GPS-CODE drifters, transmitted to the ARGOS satellite system, was programmed at 1-hour intervals. These surface drifters are considered efficient instruments for measuring and describing ocean circulation due to their accuracy in following the surface current at 1-2 cm/s.

The ARGOS and GPS drifter data positions have been subjected to quality control. The data have been interpolated at half-hour intervals with the'kriging' optimal interpolation method (Hansen and Poulain, 1996; Barbanti *et al*., 2004), low-pass filtered with a hamming filter (36-hour cut-off) in order to eliminate tidal and inertial variability and then the data have been re-sampled every 6 hours. Finally, the surface velocities have been calculated as finite differences of the position data. Detailed explanation of the data editing can be found in Ursella *et al*. (2004).

The data sets analyzed in this work span from September 2002 to March 2004; the total drifter trajectories are shown in Figure 3.2. The Northern and Central Adriatic are well covered by drifters, with a maximum of density in the northernmost part of the basin, while the south Adriatic shows a limited drifter distribution.

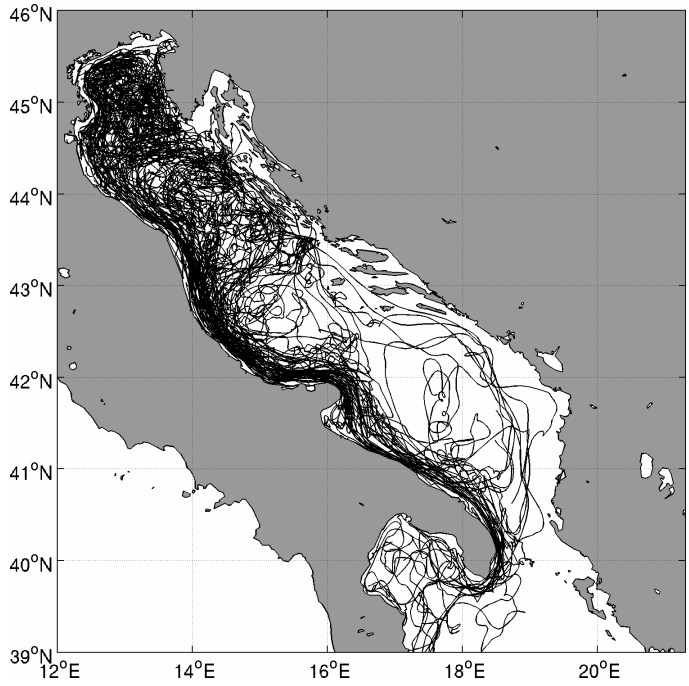

Figure 3.2 Map of the Adriatic Sea with drifter trajectories for September 2002-March 2004.

3.2.2 Model data

The current field simulation, used in this work, is provided by the Adriatic REGional Model (hereafter AREG). AREG is a free-surface, three-dimensional, finite difference numerical model with Boussinesq and hydrostatic approximation; it is based on the Princeton Ocean Model, POM (Blumberg and Mellor, 1997), as implemented by Zavatarelli and Pinardi (2003) and Oddo *et al*. (2006). The AREG grid has a horizontal resolution of about 1/45° (approximately 2.2 km) with 31 vertical sigma levels; detailed description of the model implementation can be found in Oddo *et al*. (2007).

Surface forcing is computed interactively by means of bulk formulae using the atmospheric data provided by the European Centre for Medium-Range Weather Forecasts (ECMWF) with 0.5° horizontal resolution and 6hr frequency and the model predicted sea surface temperature. The model has been used in the forecasting operational system since April 2003 and it releases a nine-day ocean forecast for all Adriatic basins every day. The modelled velocity analyzed in this work is daily mean field.

3.2.3 Lagrangian Trajectory Model

The trajectory predictions are performed with one of the Lagrangian Trajectory Models (LTM) described in Chapter 2. The Lagrangian experiments have been carried out considering only the deterministic component of LTM; the displacement of the particle is due to the advection of the current field. Furthermore, we assume that the particle moves in two dimensions only at the surface. The Lagrangian algorithm applied is SINCEM, which gave very similar results to the SINCEM2 numerical scheme.

3.3 Mean and eddy kinetic energy

In this section the comparison of average properties of the flow provided by drifter data and numerical model is explored. The analysis consists of the calculation of mean kinetic energy (MKE) and eddy kinetic energy (EKE) from the period September 2002-March 2004 for both the Eulerian model and the drifters.

The goal is to investigate the overall consistency of the Eulerian current field used to advect the particles and verify the agreement between model and observations.

Drifter density is high enough to provide significant information on the ensemble average circulation of the Adriatic basin. In order to represent the surface currents from drifters a spatial scale of averaging must be chosen. Following Poulain (2001), we have chosen to compute the mean Eulerian field in bins of 10 km radius circular separated by 10 km (with approximately 50% of overlap) assuming stationary and uniform statistics within the bins. The size of the bins has been defined in such a way that the drifters, sub-sampled every 6 hours, contribute to the bin statistics with 1-2 observations. Furthermore, to guarantee robust statistical analysis, the bins with less than 5 observations have been rejected (Ursella *et al*., 2007).

The Eulerian property has been estimated following the definition given by Poulain (2001). The mean flow has been computed averaging the six-hourly low-

pass filtered drifter velocity observations for a given bin and in time. The MKE of the mean flow is computed as:

$$MKE = \frac{1}{2}\left(\langle u\rangle^2 + \langle v\rangle^2\right) \tag{3.1}$$

where $\langle u\rangle$ and $\langle v\rangle$ are average components of the zonal and meridional velocity respectively; the EKE has then been evaluated as:

$$EKE = \frac{1}{2}\left(\langle u'u'\rangle + \langle v'v'\rangle\right) \tag{3.2}$$

where $u' = u - \langle u\rangle$, $v' = v - \langle v\rangle$ are the residual velocity components and $\langle u'u'\rangle$ and $\langle v'v'\rangle$ are diagonal elements of the velocity covariance matrix.

The mean AREG current field has been represented in two different conditions: (1) sampling the modelled current in the drifter position and binning in a box of 10 km following the same method used for the drifters (hereafter AREGa); (2) without post-processing (hereafter AREGb), using the full model resolutions.

The mean drifter flow is shown in Figure 3.3A; the main well-know features of the surface circulation in the entire Adriatic Sea are depicted. A global cyclonic circulation is represented, with a fast Eastern Adriatic Current (EAC) that flows northward along the eastern side. The EAC controls the major sub-basin recirculation cells: in the south and in the middle Adriatic around the Jacuba Pit, in the northern basin, close to the tip of the Istrian Peninsula and at the north end of the basin. The northward current returns south along the Italian coast within the WACC. Maximum velocities are found in WACC and EAC.

The AREGa mean surface current (Figure 3.3B) reproduces the main characteristics of the Adriatic circulation. We note the basin cyclonic circulation, with the intensified currents along the boundaries: the WACC on the western side and the EAC on the eastern side. The cyclonic recirculation cells are well-reproduced in the south, middle and north Adriatic. The simulated EAC and WACC show less energy than the observed one in the southern basin. Finally, Figure 3.3C shows the mean flow of AREGb; the current circulation is cyclonic and is well represented, with the middle and south cyclonic cells well evident.

The comparisons of the mean surface currents show a good agreement between observed data and simulated Eulerian field. The model appears to capture successfully the circulation structures.

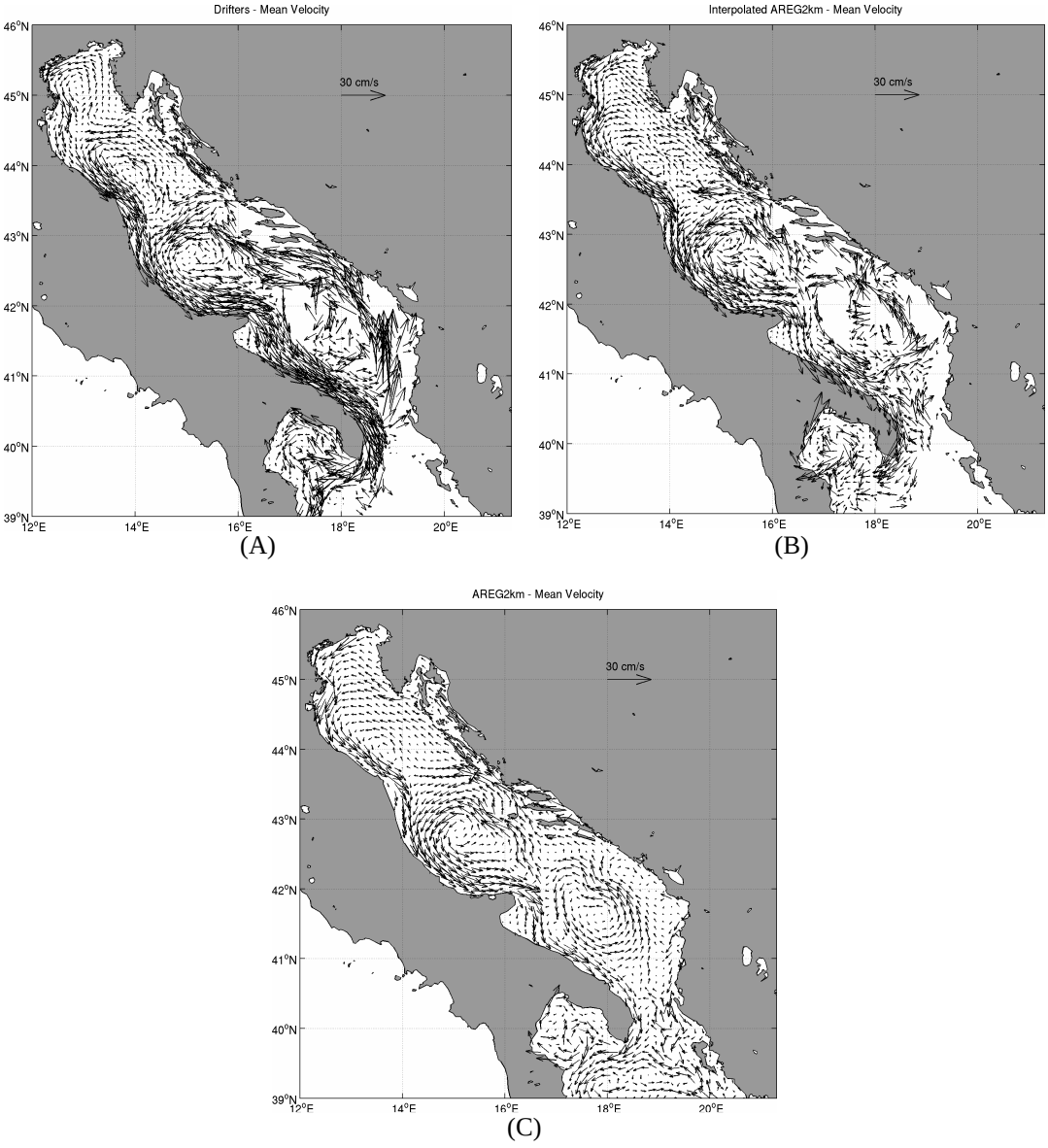

Figure 3.3 Mean current field computed from drifter dataset (A); AREG interpolated and binning (AREGa) (B); AREG without post-processing (AREGb) (C).

Horizontal maps of the MKE for drifters and AREG model are shown in Figure 3.4 (panels A,B and C). For drifter data, high values of MKE are found: (1) in front of the Po river (with 50 cm^2/s^2); (2) along the central and south Italian

coasts; (3) close to the Jacuba Pit in the Middle Adriatic and off Dubrovnik on the eastern side. The highest value is reached along the WACC current, south of Italy, while the minimum MKE is found in the open sea.

The MKE distribution for AREGa is shown in Figure 3.4B. High MKE values are localized: (1) close to the Po delta; (2) south of the Po river along the western side of the Italian coast and (3) in the middle of the Adriatic. Compared with the drifter MKE, the model values are lower with an appreciable attenuation in the southern Italian coasts. Figure 3.4C shows the MKE for AREGb; the field is smoother compared with the drifter MKE; high values are found along the north and middle Italian coasts: off Ancona, around the Gargano Promontory and the Po river delta and in the open sea around the Jacuba Pit.

Finally, we compare the maps of EKE for drifters and model (Figure 3.5). The EKE map for drifters shows high spatial variability with maximum values located along WACC, in the middle and south of the Italian coast and in the eastern side off the Albanin coast. The map of EKE from AREG does not show the same energy structure; the field is smoother than observations. In particular, the WACC signal is not well represented and the EKE is spread over larger areas with respect to observations.

The comparison between the observed data and the circulation model gives a rough validation of the AREG Eulerian product, giving an idea of the accuracy of the numerical simulation. We will now use this current field to simulate Lagrangian trajectories and depict the limited predictability of the trajectories themselves.

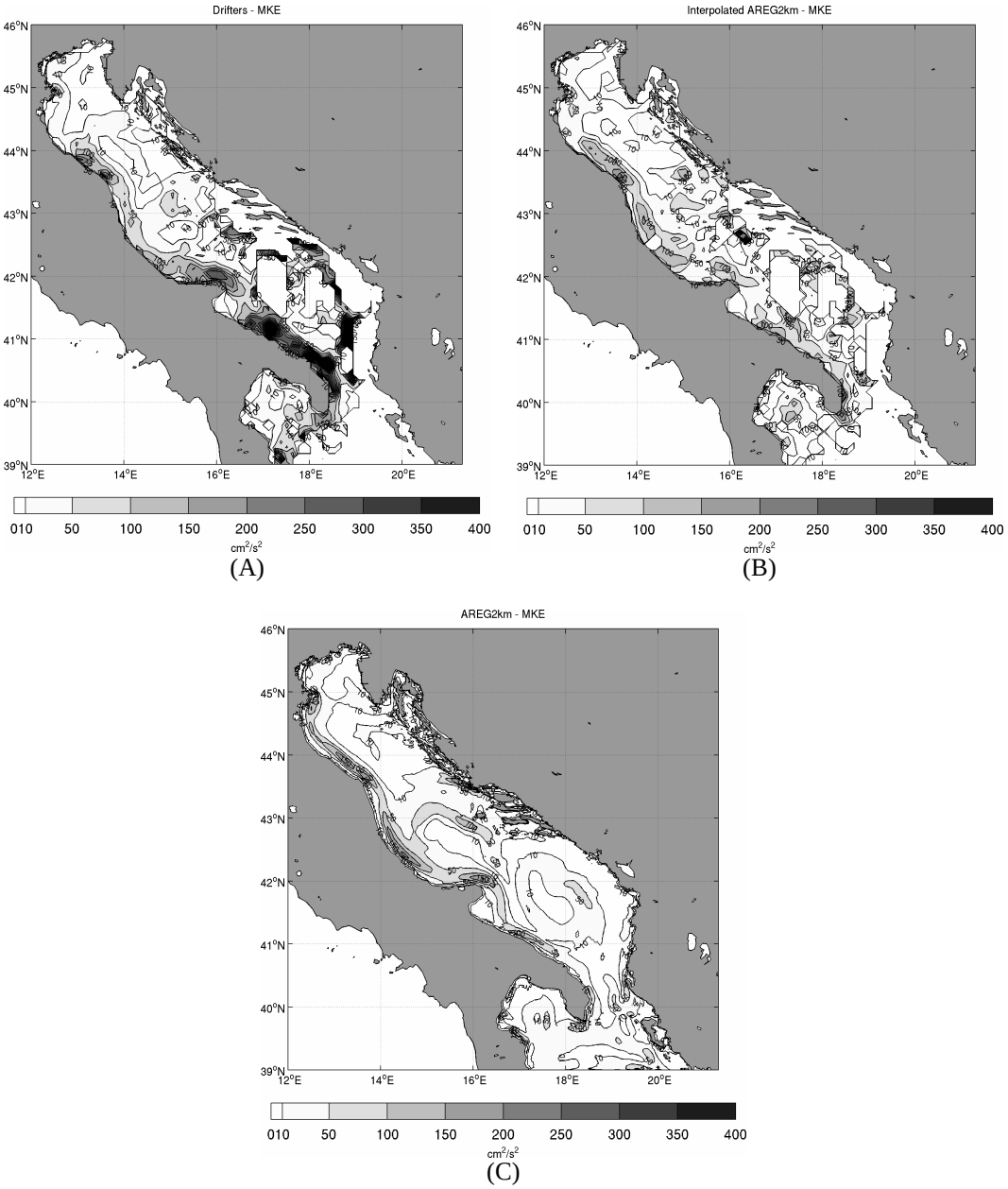

Figure 3.4 Mean Kinetic Energy computed from drifters dataset (A); AREG interpolated and binning (AREGa) (B); AREG without post-processing (AREGb) (C).

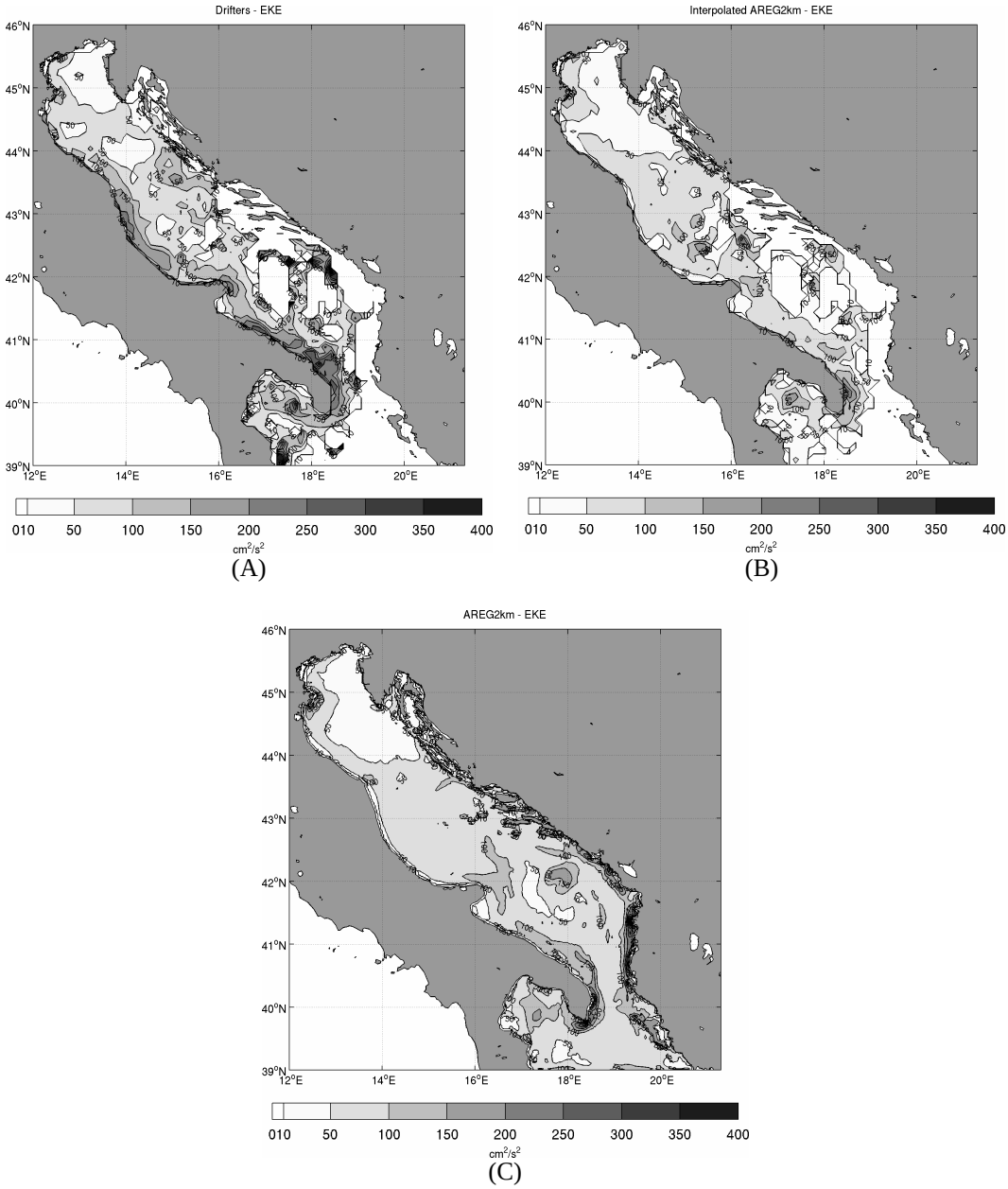

Figure 3.5 Eddy Kinetic Energy computed from drifters dataset (A); AREG interpolated and binning (AREGa) (B); AREG without post-processing (AREGb) (C).

3.4 Lagrangian comparison between drifters and model

In this section we analyze the predictability of the simulated trajectories in the Adriatic Sea using the drifter dataset described above. The goal is to give a first evaluation of the quality and accuracy of the Lagrangian model, quantify the predictive skill and evaluate the uncertainty associated with trajectory simulations. The Lagrangian statistical analysis was performed on a dataset consisting of 1663 numerical trajectories computed as follows. The particle-tracking routine is applied for clusters of particles released around the initial position of the drifter and along its trajectory every 5 days. The cluster consists of 100 particles evenly distributed in a square of 5 km around the initial and intermediate drifter positions; it is integrated for 10-days periods. The predictability has been studied computing the ensemble average distance error ($\langle d_E \rangle$) between the drifter position and the centre of mass of the simulated cluster with a temporal frequency of 6 hours:

$$\langle d_E(n\Delta t) \rangle = \frac{1}{N_T} \sum_{i=1}^{N_T} \left(\left| x_D(n\Delta t) - x_M(n\Delta t) \right| \right) \tag{3.3}$$

where N_T represents the total number trajectories computed, x_D and x_M are the drifter position and the centre of mass position of the cluster respectively, n is the total number of time steps with Δt the timestep of the Lagrangian algorithm.

This analysis has been performed applying the SINCEM algorithm, which gave very similar results to SINCEM2.

The Lagrangian error results are shown in Figure 3.6; the ensemble average distance (km) with its standard deviation is represented in function of the simulation time (days). $\langle d_E \rangle$ grows linearly with the integration time; the distance error after the first day is $\langle d_E \rangle \approx 7km$; after 3 days it becomes $\langle d_E \rangle \approx 20km$ reaching approximately $50km$ after 10 days. We conclude that the trajectory simulation accuracy is limited to 2-3 days.

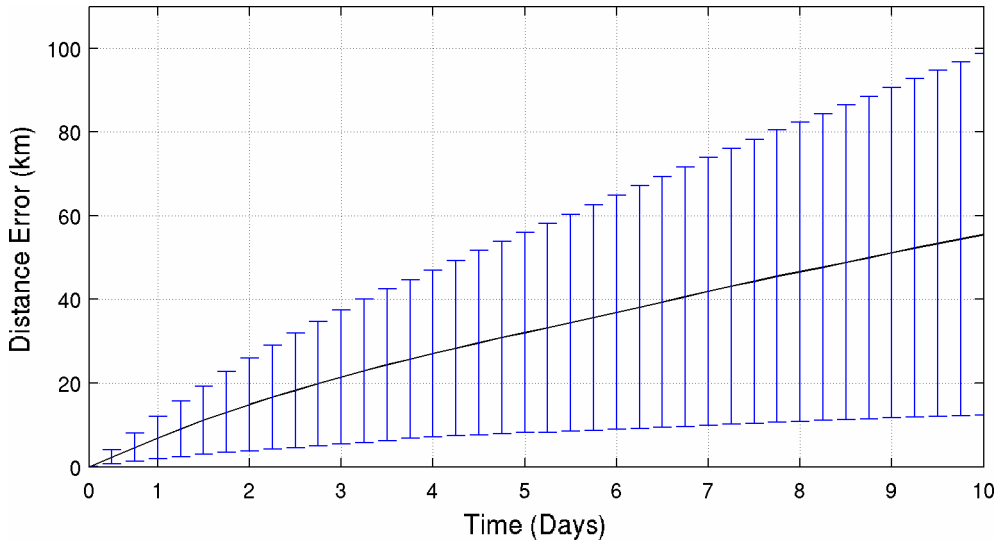

Figure 3.6 Ensemble average of the distance error between drifters and simulated particles in function of the simulation time.

In order to identify areas of different predictability the same Lagrangian analysis has been done for subregions. The Adriatic Sea has been divided into 5 different regions (Figure 3.7) on the basis of the MKE distribution. For each area we computed the $\langle d_E \rangle$ as a function of the simulation time.

Figure 3.8 shows the distance errors for each area; after 3 days of simulation area A has $\langle d_E \rangle \approx 22km$; area B ($\langle d_E \rangle \approx 17km$; area C $\langle d_E \rangle \approx 24km$; area D $\langle d_E \rangle \approx 35km$, and finally area E $\langle d_E \rangle \approx 26km$.

Lowest $\langle d_E \rangle$ values are found in area B ($\langle d_E \rangle \approx 17km$), while higher $\langle d_E \rangle$ values are present in areas D and E (respectively $\langle d_E \rangle \approx 35km$ and $\langle d_E \rangle \approx 26km$). The distance errors computed for each area have been correlated with MKE and EKE values of the AREG model. In Table 3.1 the mean values of MKE and EKE for each area computed by the drifter dataset and by the numerical model with the $\langle d_E \rangle$ values after 5 and 10 days of integration are indicated. We note that the lowest error is obtained in area B where there is the lowest difference (%) of MKE between model and observations. It seems that EKE differences are not as relevant

as MKE differences in explaining the behavior of $\langle d_E \rangle$. These results have to be repeated again with a higher precision model output now available.

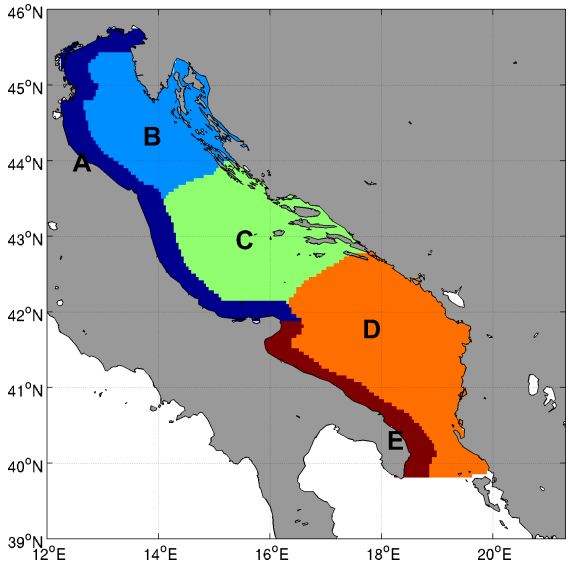

Figure 3.7 Areas of the Adriatic Sea used to analyze the Lagrangian prediction skill.

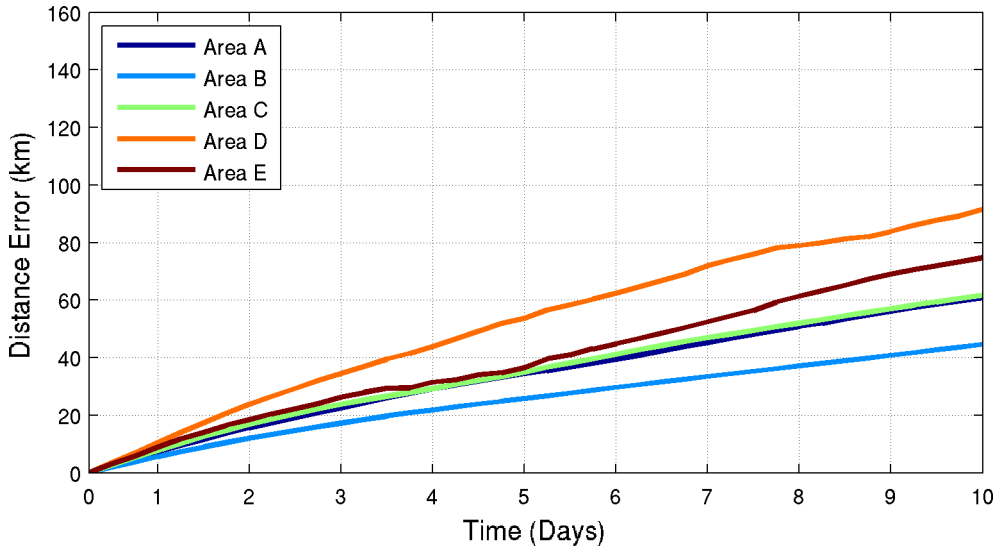

Figure 3.8 Ensemble average of the distance error between drifters and simulated particles in function of the simulation time for each area.

Areas	N°	MKE Drifter (cm^2/s^2)	MKE AREG (cm^2/s^2)	Diff. MKE (%)	EKE Drifter (cm^2/s^2)	EKE AREG (cm^2/s^2)	Diff. EKE (%)	$\langle d_E \rangle$ 5 days (km)	$\langle d_E \rangle$ 10 days (km)
A	406	75	66	12%	101	69	31%	34.5	60.6
B	771	15	12	20%	51	47	0.7%	25.8	44.6
C	307	39	30	21%	82	76	0.7%	35	61.7
D	105	158	15	90%	112	96	14%	53.6	91.5
E	74	196	31	84%	171	108	36%	36.5	74.7

Table 3.1 Statistics obtained from drifters and numerical model. See text for definition of the displayed quantities.

3.5 Summary and Conclusions

The predictability and the accuracy of the Lagrangian model developed have been explored in the Adriatic Sea using an extensive drifter dataset. This work tries to quantify the uncertainty of the simulation of particles and to evaluate the importance of the model as a tool for practical applications of the Lagrangian trajectory model. The Lagrangian model, described in detail in Chapter 2, has been forced by daily mean currents provided by a numerical circulation model at high horizontal resolution implemented in the Adriatic Sea.

Firstly, the model behaviour has been compared with the drifter dataset to determine if the Eulerian modelled field reproduces the overall Adriatic Sea circulation. The Eulerian comparison performed analyzing the mean flow MKE and EKE maps has shown that the agreement between model and data is satisfactory for MKE but not for EKE. In addition, the values of MKE and EKE are underestimated. We note a weakening of the WACC signal along the southern Italian coast.

The prediction skill of the Lagrangian model has been quantified by calculating the error in the distance between the observed drifter position and the centre of mass of a cluster of numerical particles traced by advective components of the Lagrangian model. The distance error value is of the order of 20 km after 3 days of integration. The distance error increases quickly with the time reaching approximately 50 km after 10 days. The predictability time limit of the Lagrangian simulation is there set to 2-3 days. Finally, an analysis has been

performed for different MKE and EKE subregions with the aim of identifying areas of greater and lesser predictability. This study has shown that the predictive skill may be correlated to areas of high MKE reproducibility, while it is insensitive to EKE.

The simulation skill estimated from this work can be used for practical application of the Lagrangian model for pollutant dispersion predictions. In the future we intend to investigate the Lagrangian predictability time using a better Eulerian model output now available.

Chapter 4

Maritime Rapid Environmental Assessment Experiment in the Ligurian Sea, Part 1: Development of a Relocatable Nested System

4.1 Introduction

A Maritime Rapid Environmental Assessment Experiment (hereafter MREA) took place in May/June 2007 in the Ligurian Sea (Figure 4.1). The MREA exercise was a joint effort of several Italian institutes and international organizations. The general objective of an REA is to provide in a very short time a methodology package that can be used in emergency situations in order to predict environmental parameters.

MREA is based on an ocean observational network and a model prediction system; the former collects environmental information of the present status of the ocean and the latter possible integration of the observed information, supplying ocean nowcasting and forecasting in a short time.

The origin of REAs is connected to NATO military operations and met to need of having the environmental information to support navy operations. The NATO MREA concept involves the development of a capability to set up a portable and generic ocean observing and prediction system in any region of the world ocean

efficiently in a short time (Pouliquen *et al*., 1997) relevant to numerous civilian applications, such as crisis response and temporary marine operations.

This work investigates two main novel aspects of the MREA concept:

1. Its possible application in order to manage environmental emergencies such as oil spill accidents, pollutant dispersion and search and rescue activities in open sea and coastal areas.
2. The usage of existing ocean operational forecasting system products in order to have a first guess of the ocean state and initialize ad-hoc designed limited area model.

The purposes of the MREA07 experiment in the Ligurian Sea were: (1) to collect oceanographic data to calibrate and validate the MREA concept for environmental applications in open sea and coastal areas; (2) calibrate and validate a relocatable model system embedded in the basin-scale operational oceanographic model; (3) demonstrate the utility of MREA model systems for contaminant dispersal forecasting.

Considering that pollutant spreading is strongly determined by the surface current field, the ocean forecasting system plays a crucial role in contaminant dispersion modelling. The relocatable nested model for a limited region represents a possible strategy to forecast ocean currents at high resolution and improve the Lagrangian prediction.

In this study we focus on the description of oceanographic data collected during the experiment and on the implementation of a nested system model while the MREA application for particle prediction will be the subject of Chapter 5.

The principal objective of this work is to show that an existing operational forecasting system can be used successfully in operational oceanography, to initialize and update the open boundaries of a limited-area model in order to provide a fine-resolution forecast at short notice for any sea region.

Description of the modelling set-up and comparisons between model results and observed hydrographic data collected during the MREA07 exercise will be shown. A secondary objective is to analyze the dataset coming from the MREA07

campaign during which a large amount of observations are collected and hydrographic characteristics of the water masses are examined.

The modelling system consists of a hierarchy of the following three numerical models: (1) the coarse Ocean General Circulation Model (OGCM) that covers the whole Mediterranean Sea at a resolution of approximately 6.5 km and is the modelling part of the Mediterranean Forecasting System providing ocean forecasts for the whole Mediterranean Sea on a daily basin; (2) the intermediate relocatable model for the whole Ligurian Sea (hereafter named Ligurian Intermediate Model, LIM), at a horizontal resolution of approximately 3 km; (3) the finer relocatable model for the central Ligurian Sea (hereafter named Ligurian High Resolution Model, LHRM), with a horizontal resolution of approximately 1 km.

The models are interconnected along the lateral open boundary from coarse to finer model applying the one-way off-line nesting technique; the dynamics of the finer model thus do not influence the coarse dynamic model.

The study area is the Ligurian Sea, a sub-basin of the north-western Mediterranean Sea connected to the Tyrrhenian basin through the Corsica Channel. To the East and North, the sea borders the Tuscan and Ligurian coasts respectively, while in the West it is open towards the western basin of the Mediterranean. The dominant large scale feature of the water dynamic is a permanent cyclonic circulation, more intense in winter than in summer that affects the surface and intermediate layer of the water (Astraldi and Gasparini, 1992). The southern water enters the Ligurian basin through two main currents that run along each side of Northern Corsica. The West Corsica Current (WCC) flows along the western side of Corsica while the warm and salty Tyrrhenian Current (TC) flows trough the Corsica Channel. The two currents merge north of Corsica forming the Ligurian-Provençal Current (LPC) which moves along the Ligurian and the Provence coast toward the Gulf of Lions (Astraldi *et al*., 1990). Previous works have demonstrated the existence of seasonal variability of currents in the eastern Ligurian Sea. A stronger seasonal signal was observed in the Corsica Channel than in the West Corsican Current; the warmer Tyrrhenian Current is

more energetic in winter and spring than in summer (Astraldi and Gasparini, 1992).

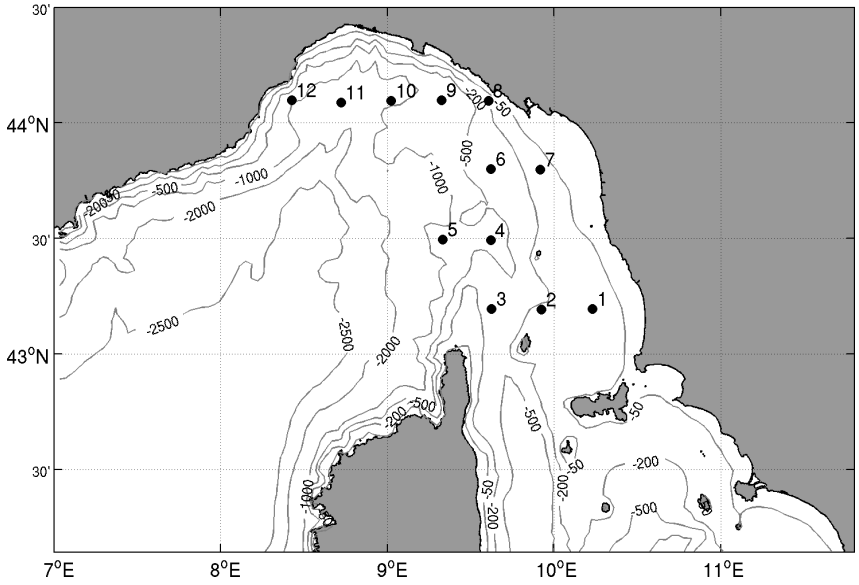

Figure 4.1 Map of the Ligurian Sea and locations of CTD stations (dots) collected during the first survey (from 7 to 9 May 2007) superimposed over the bathymetry (metres).

The monthly climatological mean for May computed from the OGCM (MFS) model for the period 2001-2007 (Figure 4.2A) shows the main features of the Ligurian Sea circulation: the northward WCC and TC that join to the north of Corsica and the LPC along the Italian coast. Furthermore, we note the eastern branch of the Tyrrhenian current, called here the 'Elba Island Current' (EIC), that flows northward around the Isle of Elba and meets the LPC. Figure 4.2B depicts the June climatology from MFS; the characteristic circulation of the Ligurian basin is maintained with an attenuation of the TC and LPC currents. The climatology fields are compared with the monthly mean circulation for May and June 2007 provided by OGCM (MFS) (Figure 4.2C, D). Significant differences can be detected in the circulation pattern: an intensification of the northward WCC which creates at the centre of the basin the large-scale cyclonic gyre located farther to the coast and the reversal of the TC along the eastern side of Corsica.

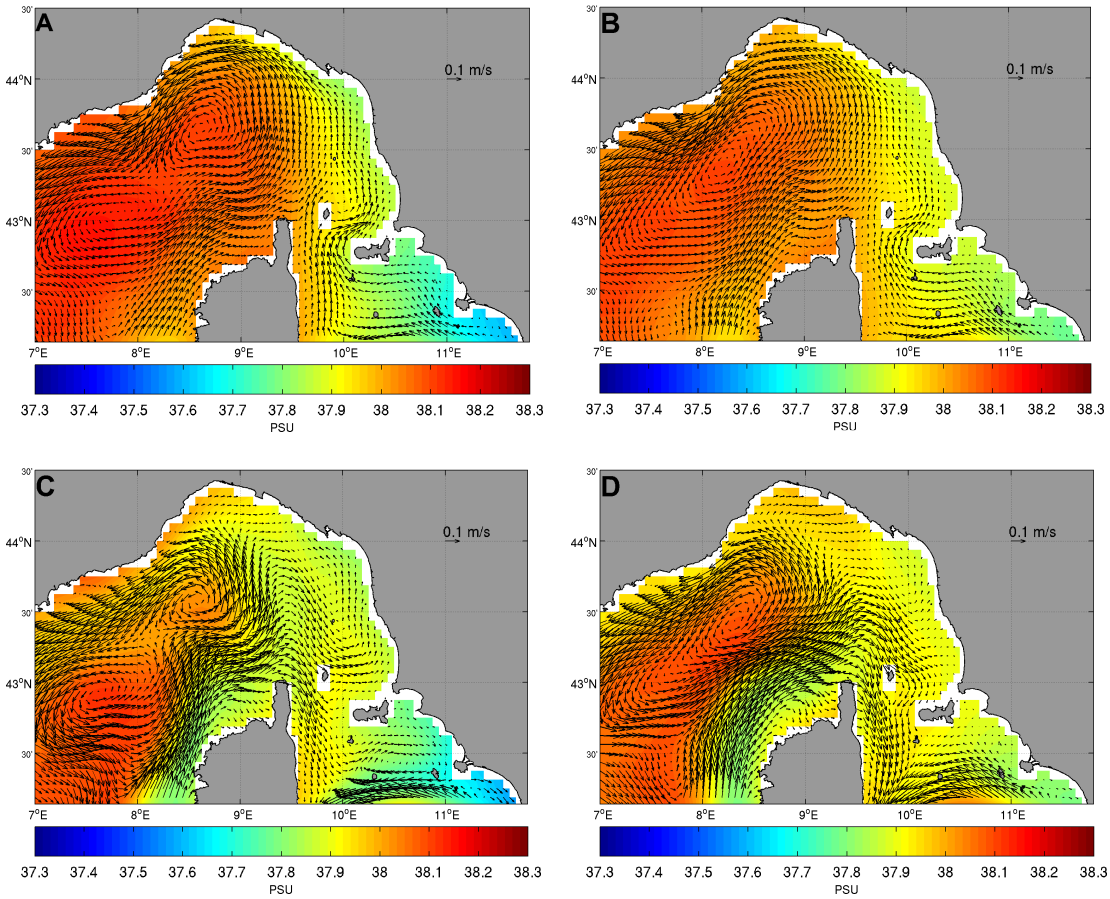

Figure 4.2 Near-surface (1.5m depth) currents [m/s] superimposed on salinity [PSU] field for the Ligurian Sea from the OGCM (MFS) model: A) Monthly mean climatology for May (period 2001-2007), B) Monthly mean climatology for June (period 2001-2007), C) Monthly mean for May 2007, D) Monthly mean for June 2007.

The temperature and salinity profiles for the Ligurian Sea are shown in Figure 4.3; they are extracted from MEDATLAS climatology (MEDAR/MEDATLAS Group 2002) and describe the properties of the water masses of the basin. Three different layers of water can be identified: the surface water, known as Modified Atlantic Water (MAW), extends to a depth of 100-200 metres; the end of this layer is characterized by a temperature minimum. The MAW is related to the Atlantic water coming from the Strait of Gibraltar and entering the Ligurian Sea from the western and eastern sides of Corsica. The intermediate water is characterized by a maximum of temperature and salinity; it consists of Modified Levantine

Intermediate Water (MLIW) coming from the east part of the Mediterranean basin and entering from the western side of Corsica. The MLIW extends approximately down to 600 m but its lower boundary is not as well defined as its upper one. The third is the deep water layer that extends from a depth of approximately 800m to the bottom and its physical properties are very different from the MLIW; this layer probably has a local origin.

This paper is organized as follows: in Section 2, the dataset collected during the MREA07 experiment is shown and the hydrographic observations are discussed. Description of the three numerical models and practical aspects of the nesting system implementation are given in Section 3. The results of the one-way nested models are shown in Section 4. Section 5 offers summary and conclusions.

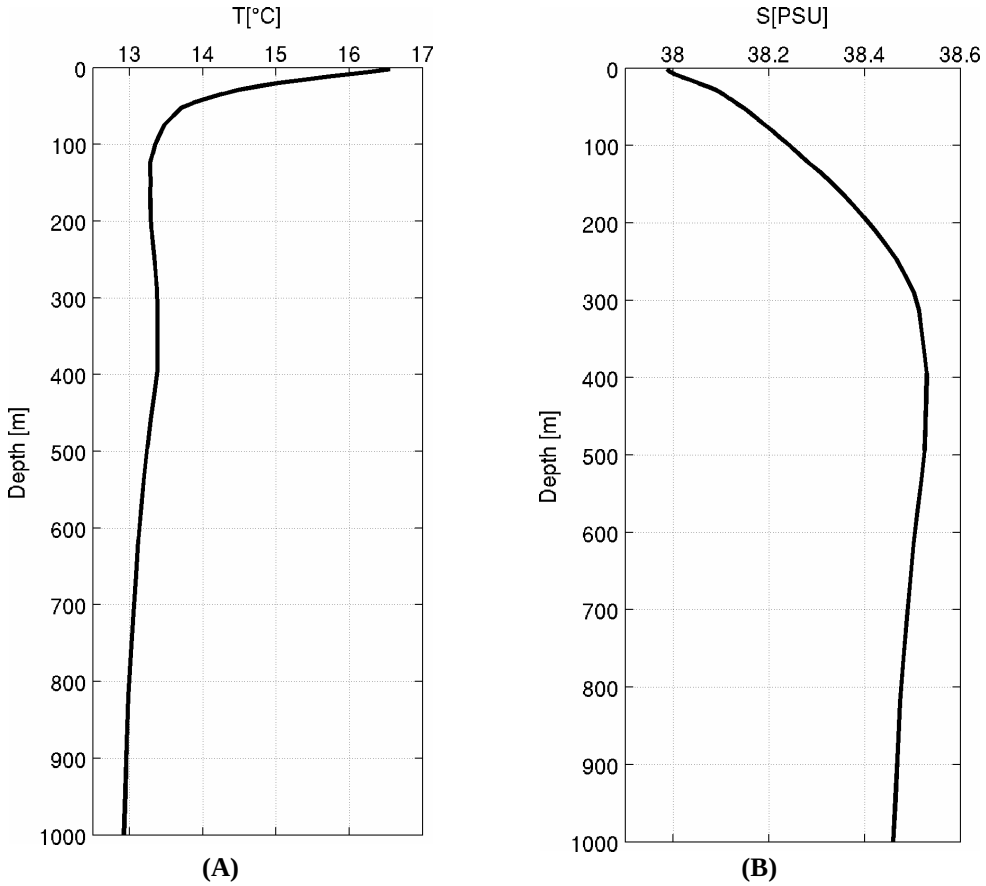

Figure 4.3 Vertical profiles of (A) temperature [°C] and (B) salinity [PSU] for the Ligurian Sea extracted from the MEDATLAS dataset for the period of May.

4.2 The MREA07 observations

4.2.1 Data Collection

The hydrographic data for MREA07 was collected by the Italian Navy Vessels Aretusa and Galatea during two oceanographic surveys. The first cruise was conducted in May by the Aretusa; weather conditions prevented the completion of the original sampling plan, and the position of the CTD collected are shown in Figure 4.1. The second campaign was carried out in June by the Galatea; the station positions are given in Figure 4.4. A total of 58 CTD casts are available over the time period 7 May-18 June 2007 used in this work to analyze the hydrographic properties of the Ligurian basin and to calibrate and validate the relocatable systems.

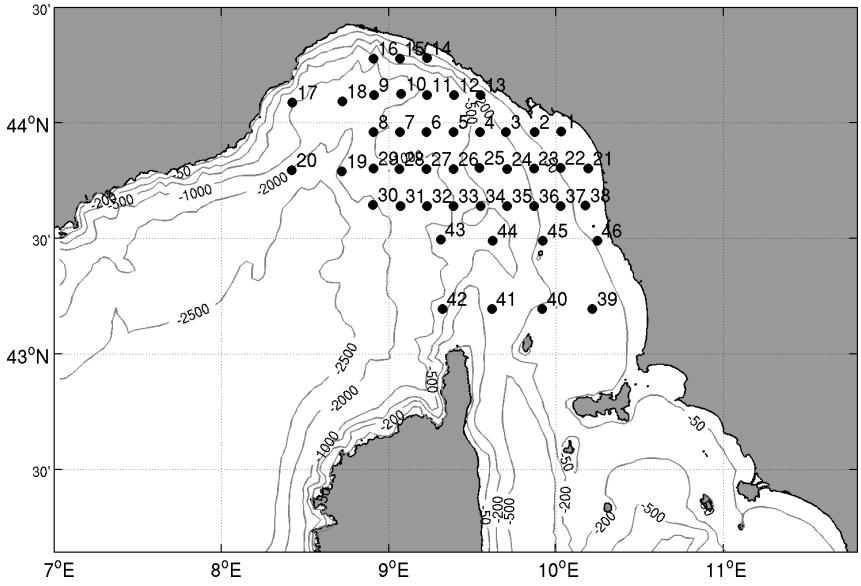

Figure 4.4 Locations of CTD stations (dots) in the Ligurian Sea during the June survey in three different periods: stations 1-20 were collected from 4 to 6 June; stations 21-38 on 13-14 June and CTD 39-46 on 18 June.

4.2.2 Hydrographic observations

In this section we describe the hydrographic observations collected in the Ligurian Sea during the first and second surveys of the MREA07 experiment.

Figure 4.5A,B shows the vertical profiles of temperature and salinity respectively for 12 CTDs collected during the period 7-9 May. We can discern in the vertical profiles the three layers of water described in the previous section. The surface layer presents the MAW signal; it extends between the surface and a depth of 200 metres where the temperature reaches the minimum value (T~13.5 °C, S~38.4 PSU). The intermediate layer is located between 200 and 800 metres and is characterized by a slight increase in temperature and a maximum of salinity (T~13.7 °C, S~38.6 PSU) distinctive of MLIW mass. Furthermore, we note a seasonal shallow thermocline in the first 50 metres of depth with a narrow upper mixed layer; the salinity at the sea surface presents a high variability ranging from 37.3 PSU to 37.9 PSU. The MAW and MLIW water masses are depicted in the T,S diagram (Figure 4.5C), which also highlights the presence of two branches of MAW, one slightly more salty than the other. The less salty branch is recorded by CTDs located in the central area of the basin while the more salty branch is measured by the coastal CTDs. This water mass distribution is also confirmed by the horizontal salinity field (Figure 4.6B) constructed with Objective Analysis (Carter and Robinson, 1987). The salinity field at a depth of 4 metres has only been visualized in the areas where the relative error of the interpolated field normalized about the field variance is less than 30%.

We note a particular pattern distribution: low-salinity water in the central basin of the Ligurian Sea and high salinity close to the Italian coast. The horizontal temperature field at 4 metres (Figure 4.6A) shows the thermal front which divides the warmer coastal waters from those in the interior.

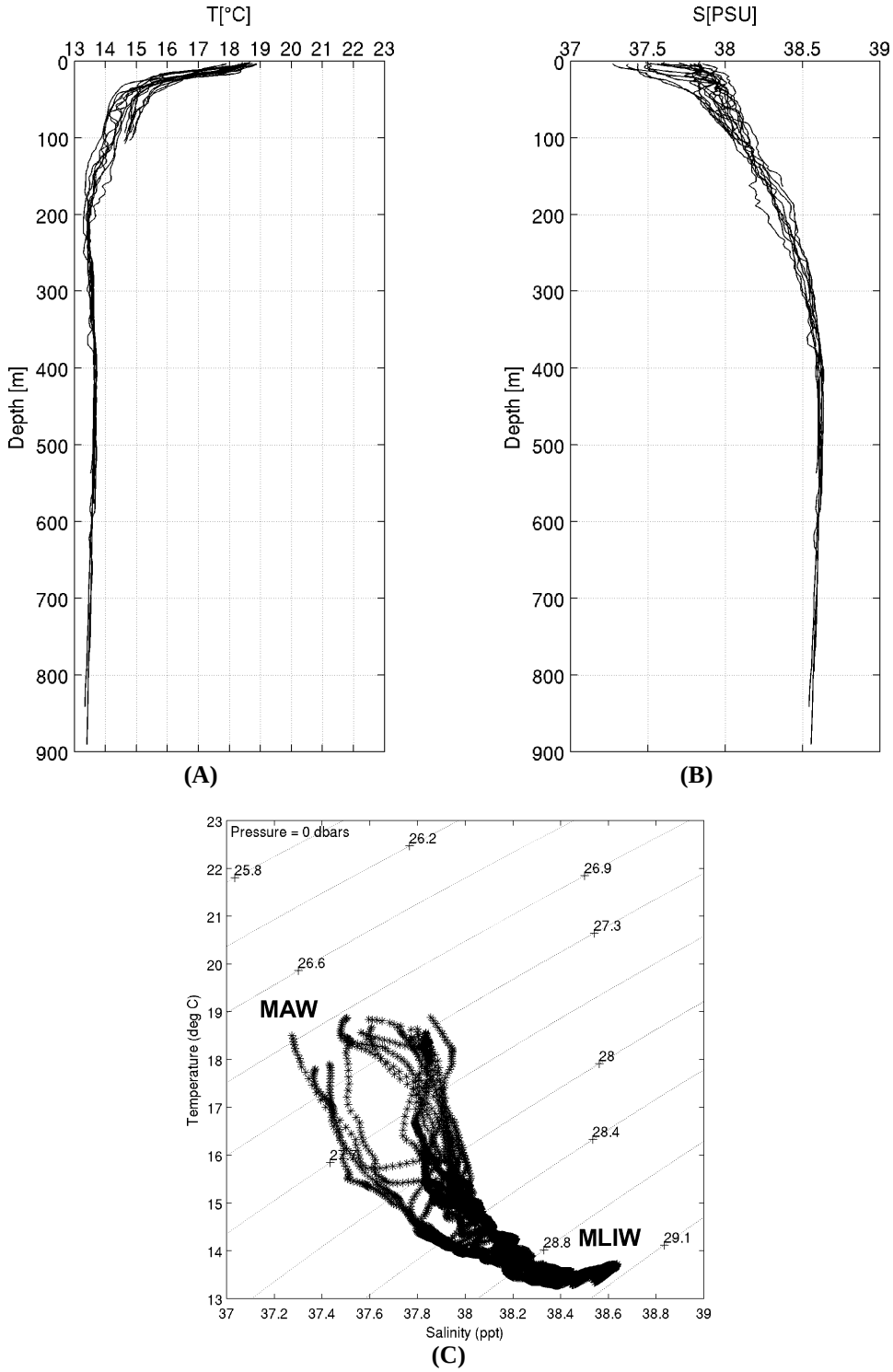

Figure 4.5 Vertical profiles of (A) temperature [°C] and (B) salinity [PSU] and (C) temperature-salinity diagram with potential density contours obtained from the CTD stations collected during the May survey in the Ligurian Sea. MAW, Modified Atlantic Water; MLIW Modified Levantine Intermediate Water.

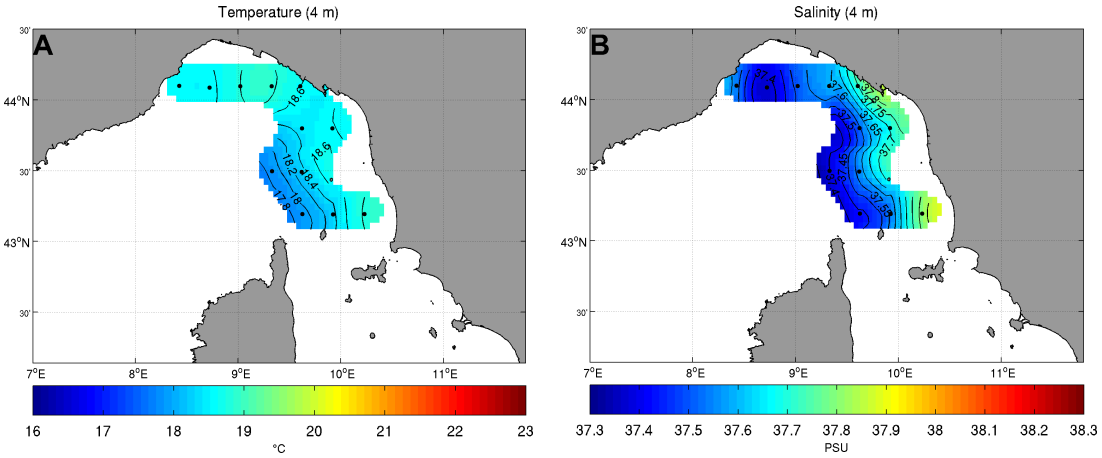

Figure 4.6 Horizontal maps of (A) temperature [°C] and (B) salinity [PSU] fields at 4 m depth constructed with the Objective Analysis technique for CTDs collected on 7-9 May, represented with dots.

The vertical profiles of temperature and salinity collected during the second cruise in June are shown in Figure 4.7A,B. The temperature profiles show stable stratification with a strong thermocline in the upper 50 metres typical of the summertime period. At the surface the temperature ranges from 17 °C to 23 °C and the salinity from 37.5 PSU to 38 PSU. A subsurface salinity maximum (S~38.6 PSU) located at 300-500 metres identifies the MLIW mass. The T,S diagram Figure 4.7C confirms the presence of the MAW and MLIW water masses and the lack of the MAW branching at different salinity observed in the May period.

The horizontal temperature and salinity fields (Figure 4.8A, B), constructed with the OA using the CTD observations collected in June, show different pattern distribution of salinity and temperature compared with May. Low-salinity water dominates the coastal area close to the Italian coast, while water of higher salinity is located in the central basin. This change can be related to seasonal variability of the TC and consequently to the EIC that weakens in the summer period. Instead the temperature field shows the thermal front with high temperature close to the coast and low temperature in the central area of the basin.

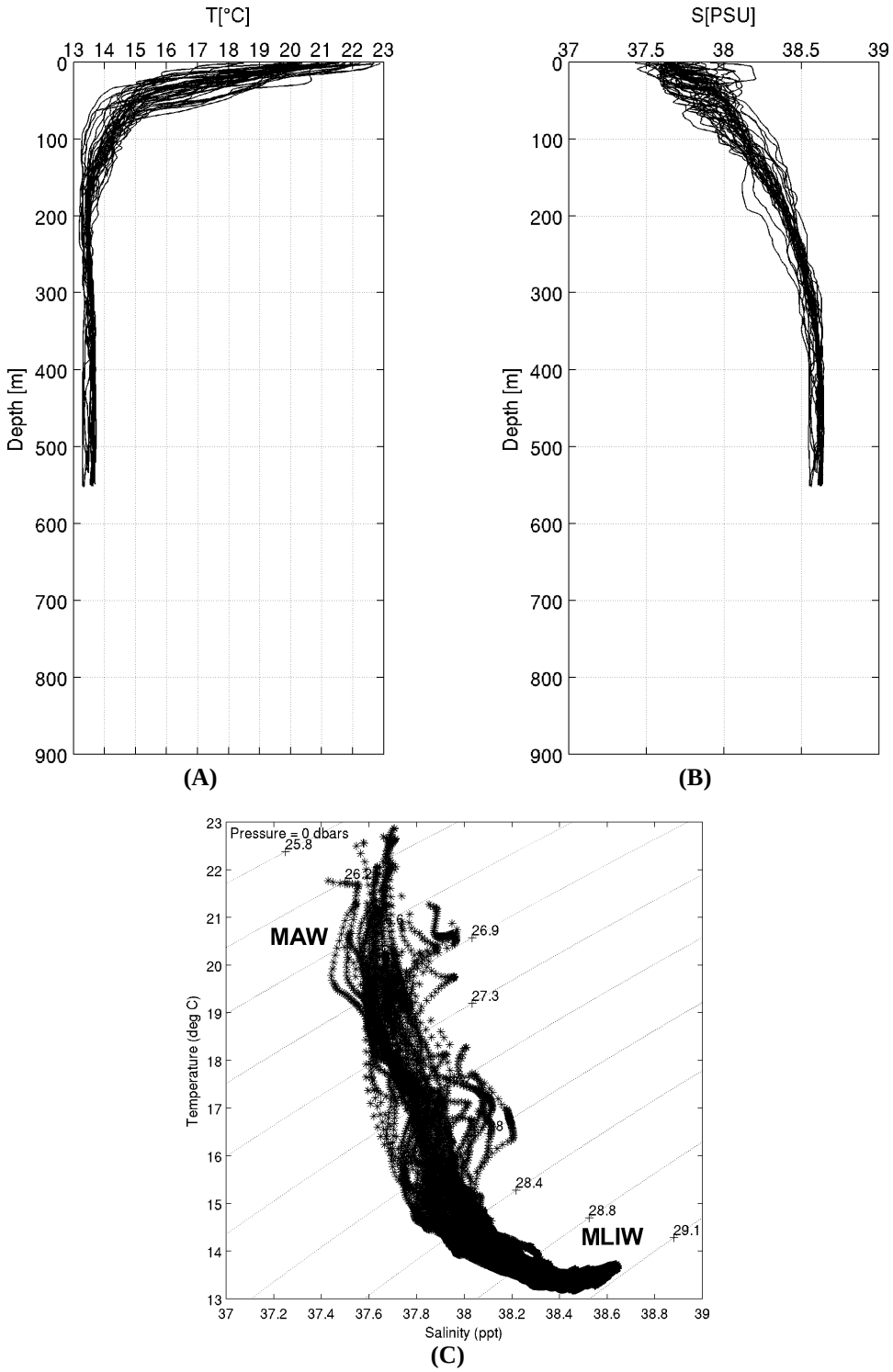

Figure 4.7 Vertical profiles of (A) temperature [°C] and (B) salinity [PSU] and (C) temperature-salinity diagram with potential density contours obtained from the CTD stations collected during the June survey in the Ligurian Sea. MAW, Modified Atlantic Water; MLIW Modified Levantine Intermediate Water.

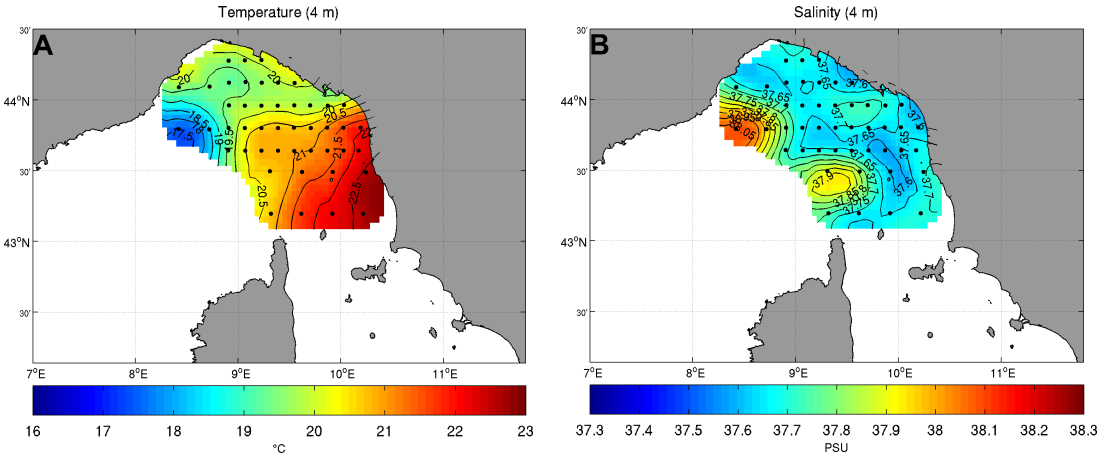

Figure 4.8 Horizontal maps of (A) temperature [°C] and (B) salinity [PSU] field at 4 m depth constructed with the Objective Analysis technique for CTDs collected on June (represented with dots).

4.3 Numerical Models for MREA

In this section we introduce the modelling system. The OGCM downscaled is the Mediterranean Forecasting System (hereafter MFS), which covers the whole Mediterranean basin, while the double nesting system embedded in the Ligurian Sea is based on the Harvard Ocean Prediction System (HOPS). The relocatable model domains are shown in Figure 4.9.

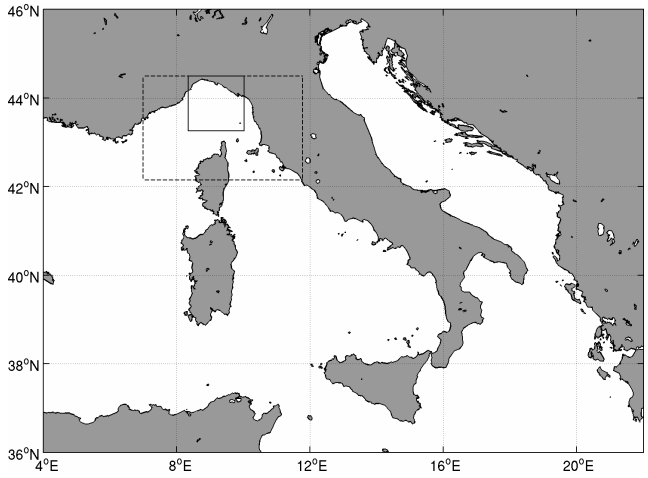

Figure 4.9 Domains of the two models. MFS is over the whole Mediterranean Sea; LIM at 3km is the area enclosed by the dashed lines and LHRM at 1km is the area enclosed by the solid line.

4.3.1 MFS Model

MFS is the operational forecasting system for the Mediterranean Sea developed in the framework of the EU-MFSTEP project (Pinardi *et al*., 2003) and is currently maintained operative by the Italian Group of Operational Oceanography (GNOO). The numerical code is based on version of the Océan PArallélisé (OPA) code (Madec *et al*., 1998) with hydrostatic, Boussinesq and incompressibility assumptions; a detailed description of the model implementation can be found in Tonani *et al*. (2008). The MFS solves prognostic primitive equations of the ocean fields of temperature, salinity, momentum and surface elevation and applies an implicit free-surface parameterization described by Roullet *et al*. (2000). The model implementation presents a horizontal resolution of 1/16°x1/16° degrees (approx. 6.5 km) and 72 unevenly-spaced vertical z-levels, with the first level located at a depth of 1.5 m. The values of the main parameters selected in MFS are listed in Table 4.1.

The model is forced at the surface with the atmospheric forcing; the air-sea fluxes of momentum and heat are interactively computed using the MFS sea surface temperature and atmospheric fields from the European Centre for Medium-range Weather Forecasts (ECMWF) with a temporal frequency of 6 hours provided by the Italian National Meteorological Office.

The MFS model also includes a data assimilation scheme based on reduced order optimal interpolation, called SOFA (System for Ocean Forecasting and Analyses code); a detailed description can be found in De Mey and Benkiran (2002) and Dobricic *et al*. (2007). The system assimilates the sea level anomaly (SLA) observed by satellites, temperature and salinity profiles from XBT and Argo floats while the sea surface temperature (SST) is assimilated using a flux correction at ocean surface (Pinardi *et al*., 2003).

4.3.2 The LIM and the LHRM

The LIM and the LHRM are based on the Harvard Ocean Prediction System (HOPS), an integrated system of software for multidisciplinary oceanographic

research developed by the physical oceanography group of Harvard University; a detailed description can be found in Robinson *et al*. (1996), Lozano *et al*. (1994, 1996), Robinson (1996,1999) and Robinson and Lermusiaux (2002, 2004).

The core of HOPS is a free-surface primitive equation model and the prognostic variables are temperature, salinity and total velocity arranged on an Arakawa B grid (Arakawa and Lamb, 1977). The set of analytical equations are the following:

Horizontal momentum:

$$\frac{\partial u}{\partial t} + \vec{u} \cdot \vec{\nabla} u - fv = -\frac{1}{\rho_0}\frac{\partial p}{\partial x} + A_h \nabla_h^2 u + A_v \frac{\partial^2 u}{\partial z^2} \tag{4.1}$$

$$\frac{\partial v}{\partial t} + \vec{u} \cdot \vec{\nabla} v + fu = -\frac{1}{\rho_0}\frac{\partial p}{\partial y} + A_h \nabla_h^2 v + A_v \frac{\partial^2 v}{\partial z^2} \tag{4.2}$$

Vertical momentum:

$$\frac{\partial p}{\partial z} = -\rho(x, y, z, t) g \tag{4.3}$$

Thermal energy:

$$\frac{\partial T}{\partial t} + \vec{u} \cdot \vec{\nabla} T = K_h \nabla_h^2 T + K_v \frac{\partial^2 T}{\partial z^2} \tag{4.4}$$

Conservation of salt:

$$\frac{\partial S}{\partial t} + \vec{u} \cdot \vec{\nabla} S = K_h \nabla_h^2 S + K_v \frac{\partial^2 S}{\partial z^2} \tag{4.5}$$

Conservation of mass:

$$\vec{\nabla} \cdot \vec{u} = 0 \tag{4.6}$$

Equation of state:

$$\rho(x, y, z, t) = f(T, S, p) \tag{4.7}$$

where u and v are the velocity components, T the temperature, S the salinity, $f = 2\Omega \sin\theta$ the Coriolis term with Ω the constant earth rotation rate and θ the latitude, ρ_0 is the reference density , p the water pressure, ρ the density, g is the gravity, A_h and K_h are the horizontal eddy viscosity and diffusivity, A_v and

K_v are the vertical eddy viscosity and diffusivity. The vertical coordinate system is a topography-following system ("double-sigma") for accurate modelling of steep topography. The values of the main parameters used in LIM and LHRM are listed in Table 4.1.

The horizontal subgrid-scale processes (A_h, K_h) are parameterized by applying a Shapiro filter (Shapiro, 1970) to the variations of the total velocity, tracers and barotropic vorticity tendency (F_U, F_T, F_W), see Table1. For the vertical mixing near the surface, a mixing-layer model function of the local wind-stress transfers and dissipates the atmospheric forcing; the depth of the mixed layer called in the model 'Ekman depth' (h_e) is computed as $h_e(x,y,z,t) = E_k(\sqrt{\|\boldsymbol{\tau}\|/\rho_0})/f$ (Rossby and Montgomery, 1935; Cushman-Roisin, 1994) where E_k is an empirical factor, $\boldsymbol{\tau}$ the wind stress vector, ρ_0 and f as above; this depth is also constrained by adjustable bounds ($h^e_{\min}$ and $h^e_{\max}$). The vertical eddy coefficients (A_v^e and K_v^e) are set to empirical values inside the mixed layer while below h_e they are based on the local gradient Richardson number (Ri), using a scheme similar to that of Pacanowski and Philander (PP) (1981). Following PP parameterization:

$$A_v = A_v^b + \frac{v_0}{(1+5Ri^2)} \;;\; K_v = K_v^b + \frac{v_0}{(1+5Ri^3)} \tag{4.8}$$

where A_v^b and K_v^b are the background coefficients, v_0 the vertical eddy viscosity coefficient at $Ri = 0$. The model also uses the 'convective adjustment' that consists of applying high mixing coefficients (A_v^{cvct}, K_v^{cvct}) in regions where the stratification is unstable ($Ri < 0$) in order to restore a stable vertical density profile.

Across coastlines, normal flow and tracer flux are set to zero. At the bottom, a dynamic stress balance is applied to the momentum equations, with a drag coefficient (C_d). Along coastlines and in the bottom an additional Rayleigh

friction is applied using a Gaussian weighting of distance from the bottom or the coast respectively (Lermusiaux, 1997).

The HOPS model version of LIM and LHRM interactively computes the heat and momentum surface fluxes starting from ECMWF 6-hour meteorological fields using bulk formulae. Surface flux formulation is called interactive because the heat fluxes depend on the sea surface temperature computed by the model. The bulk formulations used are: the Hellerman and Rosenstein (1983) to compute the wind stress from surface winds, the Gill (1982) for latent heat flux, the Reed (1977) for solar radiation, the Bignami *et al*. (1995) for net long-wave flux and the Kondo (1975) for sensible heat flux.

The fresh water flux is calculated by the difference between the evaporation minus the precipitation. The evaporation flux has been estimated from the latent heat flux while the precipitation values are taken from climatologically monthly dataset CPC Merged Analysis of Precipitation (CMAP) obtained by merging gauge and satellite estimates (Xie and Arkin,1997).

For lateral open boundary condition a simple off-line, one-way nesting technique is implemented. A provided Orlanski implicit radiation condition is applied to the open boundary for tracers and velocity. This boundary scheme follows the algorithm of Perkins *et al*. (1997); corrections to the provided values to the boundary are obtained by applying the Orlanski (1976) algorithm to the difference between the model values and the provided values.

	MFS	LIM	LHRM
Numerical Parameters			
Horizontal Resolution	~ 6.5 km	~3 km	~1 km
Vertical Resolution	72 z-level	30 double σ-level	30 double σ-level
Time step model	600 sec	100 sec	100 sec
Physical Parameters			
Horizontal mixing	Constant Coefficients $A_h = 5x10^9 m^4 / s$ $K_h = 3x10^9 m^4 / s$	Shapiro filter $F_U : n=4; m=1; k=1$ $F_T : n=4; m=1; k=1$ $F_W : n=2; m=1; k=1$	Shapiro filter $F_U : n=4; m=1; k=1$ $F_T : n=4; m=1; k=1$ $F_W : n=2; m=1; k=1$
Surface vertical mixing (mixed layer)	Not present	$E_k = 0.25$ $h^e_{\min} = 1m$; $h^e_{\max} = 35m$ $A^e_v = 30cm^2 / s$ $K^e_v = 5cm^2 / s$	$E_k = 0.25$ $h^e_{\min} = 1m$; $h^e_{\max} = 35m$ $A^e_v = 20cm^2 / s$ $K^e_v = 3cm^2 / s$
Interior vertical mixing (Pakanowsky-Philander)	$A^b_v = 1.5x10^{-4} m^2 / s$ $K^b_v = 0.3x10^{-4} m^2 / s$ $A^{cvct}_v = 1m^2 / s$ $K^{cvct}_v = 1m^2 / s$	$A^b_v = 0.1cm^2 / s$ $K^b_v = 0.01cm^2 / s$ $A^{cvct}_v = 100cm^2 / s$ $K^{cvct}_v = 100cm^2 / s$ $v_0 = 100cm^2 / s$	$A^b_v = 0.1cm^2 / s$ $K^b_v = 0.01cm^2 / s$ $A^{cvct}_v = 100cm^2 / s$ $K^{cvct}_v = 100cm^2 / s$ $v_0 = 100cm^2 / s$
Bottom drag coefficient	$C_D = 10^{-3}$	$C_D = 2.5x10^{-3}$	$C_D = 2.5x10^{-3}$

Table 4.1 Numerical and physical model parameters of the MFS, LIM and LHRM. A_h **and** K_h **are horizontal eddy viscosity and diffusivity coefficients;** F_U **,** F_V **and** F_W **represent the Shapiro filtering parameterization of horizontal subgrid-scale processes on the total velocities, tracer fields and barotropic vorticity tendency with** n **the order,** m **the number of application for timestep and** k **its frequency. For the other parameters see the text.**

4.3.3 The LIM and LHRM: configuration and initialization

The LIM domain covers the region from 42.14° N to 44.49° N and from 6.9° E to 11.8° E. The horizontal grid resolution is approximately 3km and consists of

130x88 points. The vertical grid has 30 double–sigma levels. The model presents two open boundaries located to the South and West (Figure 4.9).

The LHRM domain lies between 43.26°N and 44.49°N and between 8.34° E and 10.02°E. The horizontal resolution is 1km and in the vertical 30 double-sigma levels with similar distribution of LIM. The model has three open boundaries to the South, West and East (Figure 4.9).

The bathymetry for both models has been obtained from the U.S. Navy unclassified 1/60° bathymetric database DBDB-1, by linear interpolation of the depth data into the model grid. The minimum depth has been set to 10 m for both models.

The LIM model's initial and lateral boundary conditions are taken from the coarse model MFS. The variables temperature, salinity and the total velocity (meridional and zonal component) have been extracted from MFS and bilinearly interpolated onto the horizontal grid and mapped from flat (z-levels) to terrain-following levels. The LHRM initial and lateral boundary conditios, however, have been obtained from the LIM model with the same technique.

4.3.4 The numerical experiments

LIM and LHRM have been integrated for three different periods for which the CTD data are available. The experiments carried out are summarized in Table 4.2. The LIM has been initialized 7 days before the first CTD data available, and has been forced at the lateral boundary using MFS output. LIM has been integrated for 15 days for three different periods: 1) from 1 May to 15 May; 2) from 29 May to 12 June and 3) from 7 June to 21 June.

Initial and open boundary conditions for LHRM have been provided by LIM fields. The LHRM model has been initialized three days before the first 'CTD time' and integrated for 12 days forward for the following periods: 1) from 4 May to 15 May; 2) from 1 June to 12 June and 3) from 10 June to 21 June.

These experiments have been performed using two different vertical grids: the original at 40 sigma-levels and the final with 30 sigma-levels. The comparison between simulated and observed vertical profiles of temperature and salinity (not

shown here) have detected a better model performance using the configuration with 30 vertical levels, which is able to represent more accurately the vertical structure of the observed ocean and which has been chosen as the final setup for the LIM and LHRM.

The following section shows the simulation results comparing the nested system with MFS model and observation data.

	LIM		**LHRM**
Exp1	1-15 May (Initialized from MFS)	**Exp1A**	4-15 May (Initialized from LIM-Exp1)
Exp2	29 May-12 June (Initialized from MFS)	**Exp2A**	1-12 June (Initialized from LIM-Exp2)
Exp3	7-21 June (Initialized from MFS)	**Exp3A**	10-21 June (Initialized from LIM-Exp3)

Table 4.2 Numerical Experiments.

4.4 Results and Discussion

In this section we present the assessment of the results obtained with the nested system comparing the observed salinity and temperature vertical profiles with profiles simulated by LIM, LHRM and MFS; furthermore, the current fields simulated will be shown.

4.4.1 LIM & LHRM: Comparisons with MFS

The accuracy and the quality of the LIM and LHRM relocatable models have been studied by using bias and Root Mean Square (RMS) error indices. The bias represents the difference between the model (M_i) and observed (O_i) values and the correspondent RMS error is computed as:

$$RMS = \sqrt{\frac{1}{N}\sum_{i=1}^{N}(M_i - O_i)^2} \tag{4.9}$$

where N is the total number of data.

The bias and RMS error are calculated between observed temperature and salinity vertical profiles and profiles extracted from MFS, LIM and LHRM.

Figure 4.10 shows the bias and RMS error for the first experiment (Exp1) carried out with LIM configuration initialized on 1 May at 00:00 from the MFS analysis; the comparison has been carried out using the 12 CTDs collected on 7-9 May. Figure 4.10A depicts a negative temperature bias for MFS and LIM; that is, the modelled profiles are colder than observed data. However, the salinity bias for MFS and LIM (Figure 4.10B) is positive in the first 30m of depth and the model's behaviour is essentially equivalent. The RMS error profiles (Figure 4.10C, D) indicate good agreement between models and observed values below depths of 30m; in the surface we note a slight improvement in LIM temperature RMS error that can be related to the vertical mixing scheme chosen.

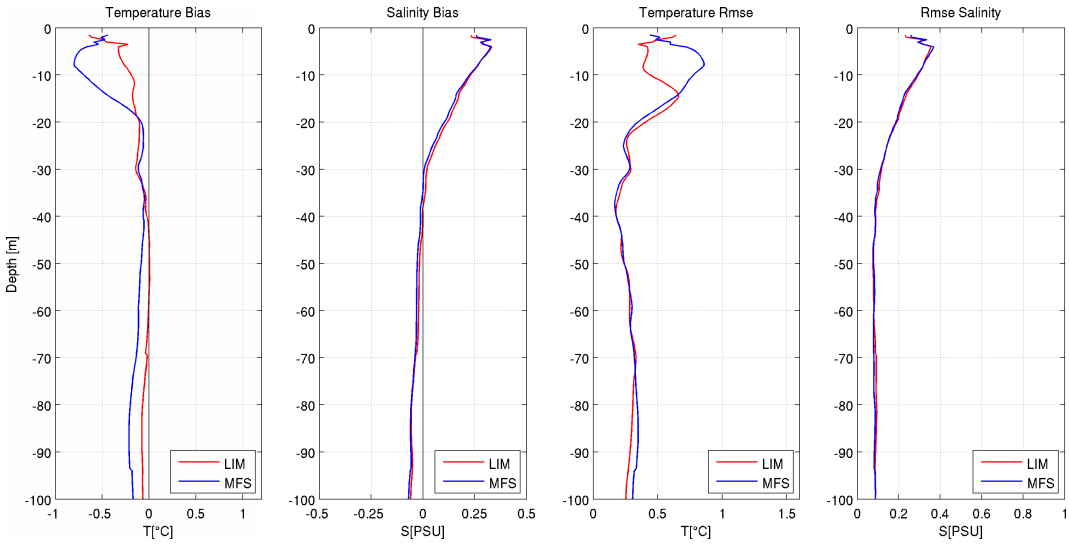

Figure 4.10 Averaged vertical profiles for the upper 100m for: (A) temperature bias, (B) salinity bias, (C) temperature RMS error, (D) salinity RMS error. Blue lines indicate MFS results and red lines LIM results for Exp1.

In the second experiment (Exp2), LIM was initialized on 29 May at 00:00 from the MFS analysis; the bias and RMS error have been computed using the 20 CTDs collected in the period 4-6 June (Figure 4.11). The main differences between MFS and LIM performance are in the temperature vertical structure for the first 70m of depth: the LIM simulated temperature are higher than observed values and the model is not able to improve the MFS result; this may be a direct consequence of

the initialization. The LIM temperature RMS (Figure 4.11C) presents a subsurface maximum located at 25 metres. At the surface water (0-20 depth) there is an overestimation of the salinity in MFS and LIM represented by a positive salinity bias: the models are more salty than observed values (Figure 4.11B).

Figure 4.12 shows the bias and RMS error computed from the third experiment (Exp3) using the 26 CTDs collected on 13-18 June; the LIM is initialized on 9 June at 00:00. We observe a still positive salinity bias in the surface water and a negative temperature bias; the MFS and LIM simulated temperatures are colder than observed data. The RMS error profile for LIM temperature presents a subsurface maximum located at 40 metres (Figure 4.12C).

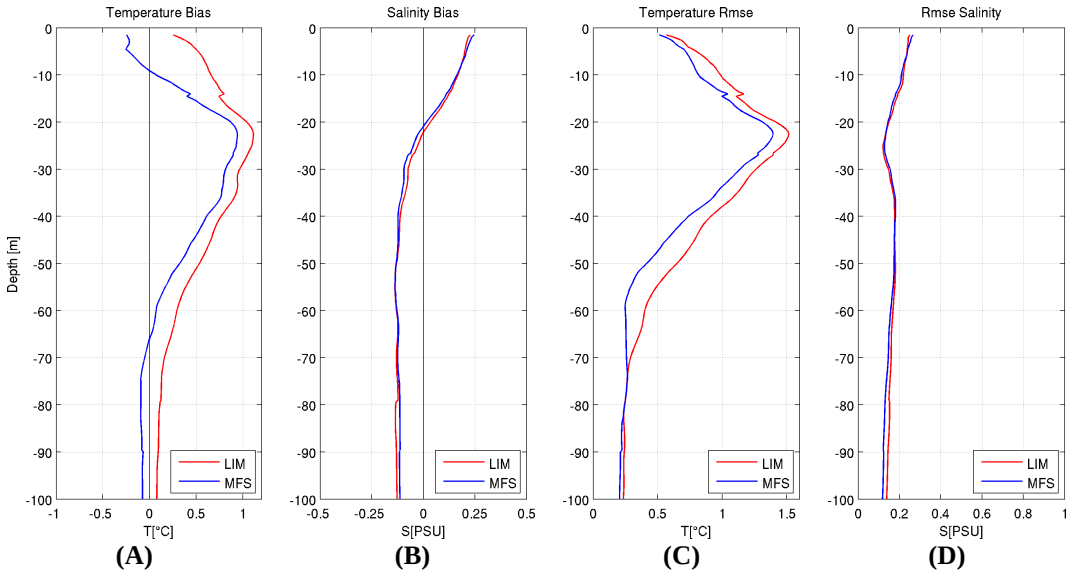

Figure 4.11 Averaged vertical profiles for the upper 100m for: (A) temperature bias, (B) salinity bias, (C) temperature RMS error, (D) salinity RMS error. Blue lines indicate MFS results and red lines LIM results for Exp2.

The performance of LIM simulation has also been analyzed comparing its horizontal temperature and salinity fields with those of MFS and the observed data shown above (Figure 4.6, Figure 4.8). The temperature and salinity fields at 4 m have been obtained applying the OA scheme to both observation and model results sampled in the CTD positions. The MFS (Figure 4.13A, C) and LIM (Figure 4.14A, C) temperature fields build for May and June 2007 show a well

represented thermal front with the LIM temperature slightly closer to the observed fields than MFS. The LIM horizontal salinity field (Figure 4.14B, D), although saltier than observed data, presents a better pattern salinity distribution compared to MFS, which shows (Figure 4.13B, D) a smooth salinity field. For the May period the LIM matches the salinity gradient of the observed field; the salinity decreases from coast to central basin.

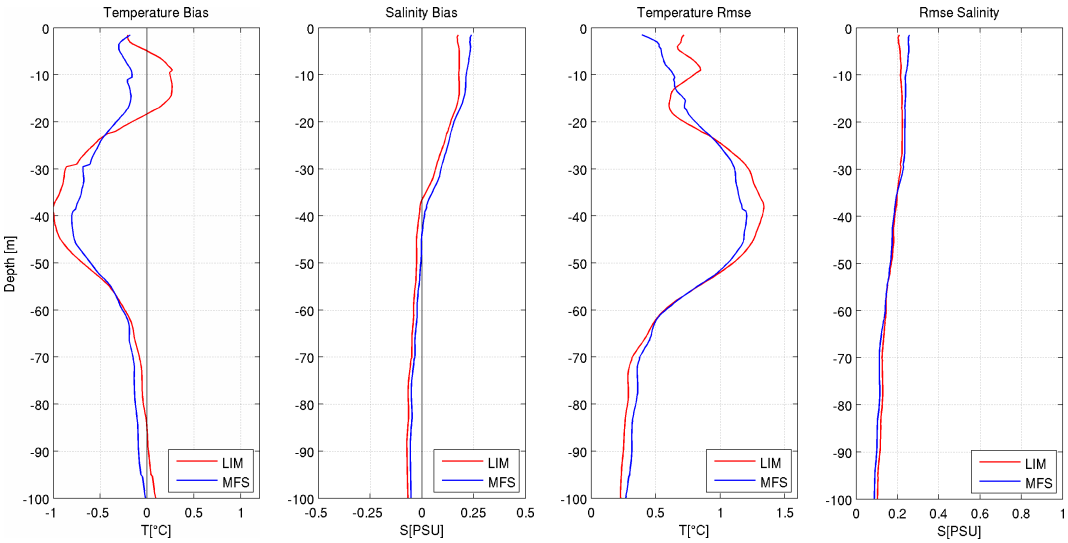

Figure 4.12 Averaged vertical profiles for the upper 100m for: (A) temperature bias, (B) salinity bias, (C) temperature RMS error, (D) salinity RMS error. Blue lines indicate MFS results and red lines LIM results for Exp3.

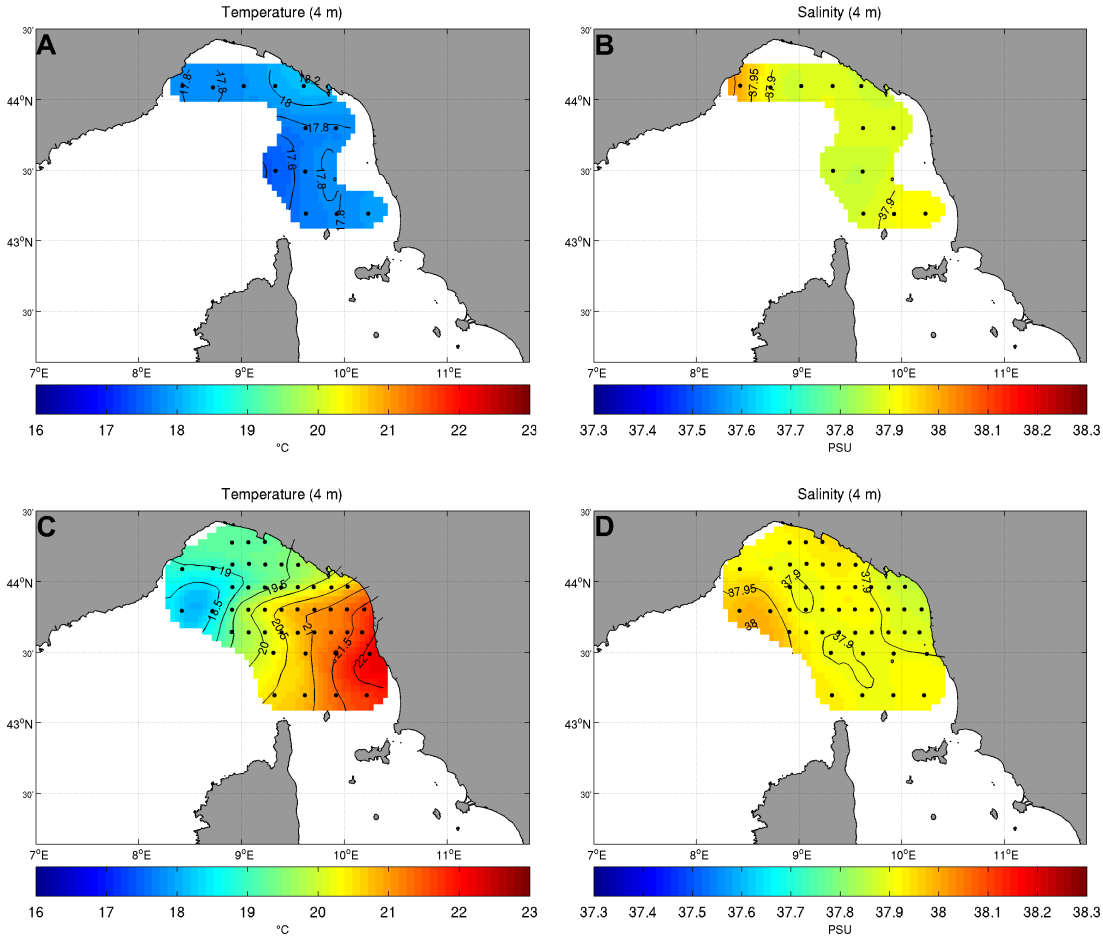

Figure 4.13 Horizontal maps at 4 m depth constructed with the Objective Analysis technique from MFS analyses: (A) temperature map for 7-9 May, (B) salinity map for 7-9 May, (C) temperature map for 4-18 June, (D) salinity map for 4-18 June.

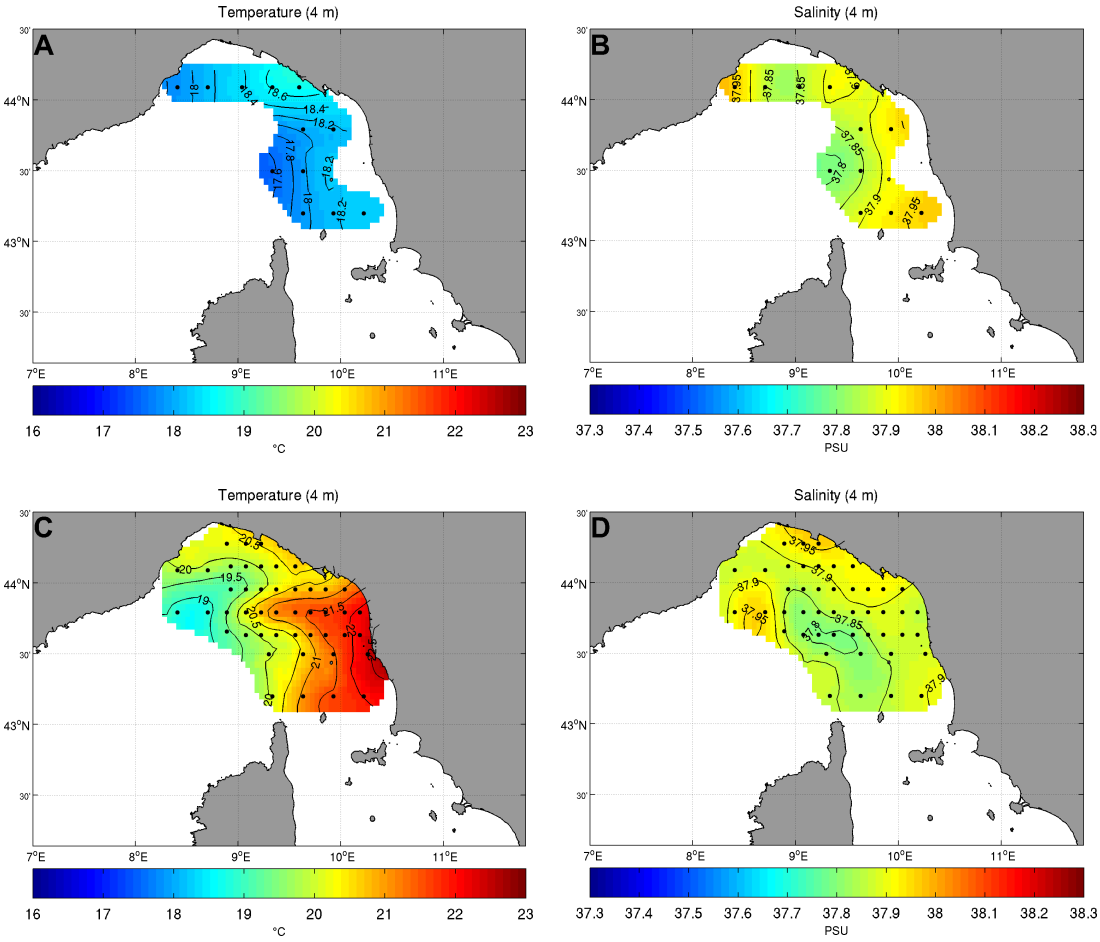

Figure 4.14 Horizontal maps at 4 m depth constructed with the Objective Analysis technique from LIM simulation: (A) temperature map for 7-9 May, (B) salinity map for 7-9 May, (C) temperature map for 4-18 June, (D) salinity map for 4-18 June.

The comparisons of the vertical profiles and the horizontal fields have also been carried out for LHRM simulations. Not all CTD data have been used for the quantitative comparison because the LHRM domain does not cover all data positions; the location of the CTD used for each campaign is shown in Figure 4.18.

In Figure 4.15 the bias and RMS error for Exp1A is shown; the major differences are evident in the temperature RMS error profiles (Figure 4.15C). The LHRM

gives better results in the upper layer (0-15m) with respect to LIM and MFS but a worsening of the results between 20 and 70m of depth. For salinity bias and RMS error the three models are equivalent (Figure 4.15B, D).

In the second experiment, Exp2A (Figure 4.16), we note a slight improvement in the LHRM in the temperature RMS error compared to LIM behaviour. Figure 4.17 shows the bias and RMS error of the third experiment (Exp3A). LHRM provides similar behaviour to the LIM simulation in salinity and temperature profiles.

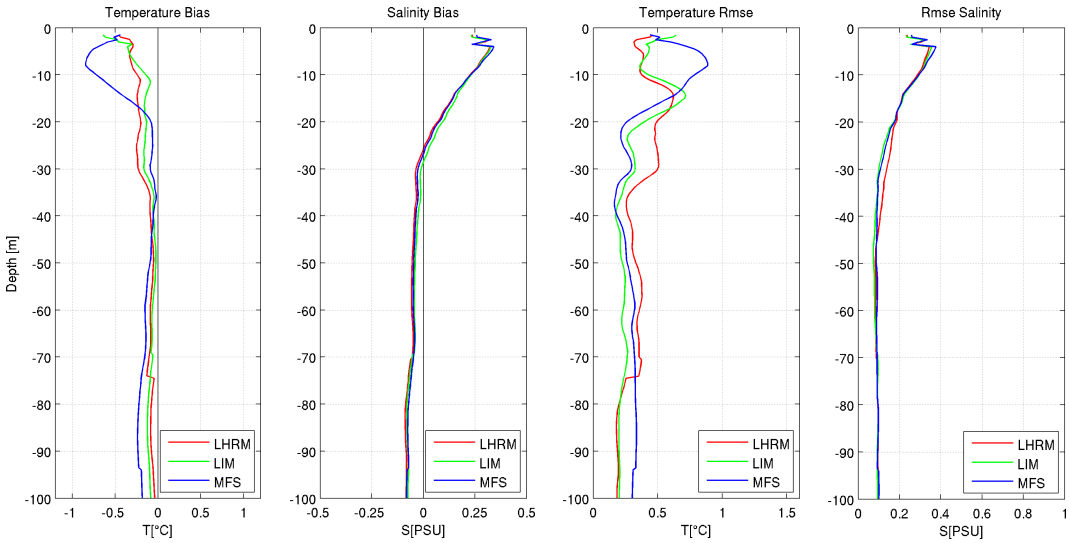

Figure 4.15 Averaged vertical profiles for the upper 100m for: (A) temperature bias, (B) salinity bias, (C) temperature RMS error, (D) salinity RMS error. Blue lines indicate MFS results, green lines LIM results and red lines LHRM results for Exp1A.

The temperature and salinity horizontal fields obtained by applying the objective analysis to LHRM simulations (Figure 4.18) confirm the results shown by bias and RMS error profiles. The salinity and temperature fields for May and June are very similar to LIM maps; there is no clear improvement of the second nested model. This probably depends on the time of initialization: 3 days is too short a time to create the small scales not captured in the initial conditions. Another problem might be the small number of CTD data, which is not sufficient for a robust statistic. Furthermore, the LHRM results are affected by coarse horizontal

resolution of the atmospheric forcing and both relocatable models are driven by the same atmospheric dataset (ECMWF).

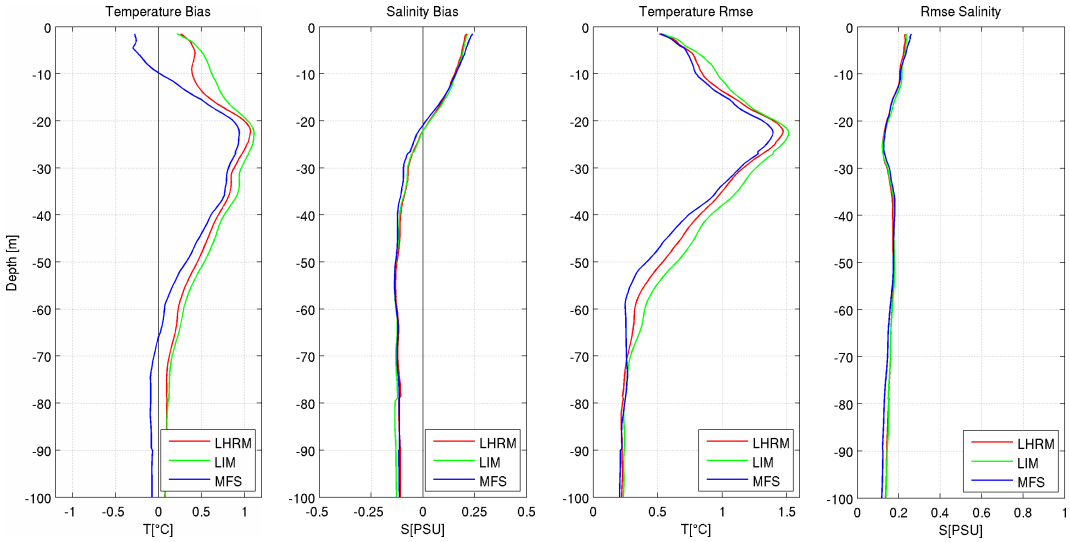

Figure 4.16 Averaged vertical profiles for the upper 100m for: (A) temperature bias, (B) salinity bias, (C) temperature RMS error, (D) salinity RMS error. Blue lines indicate MFS results, green lines LIM results and red lines LHRM results for Exp2A.

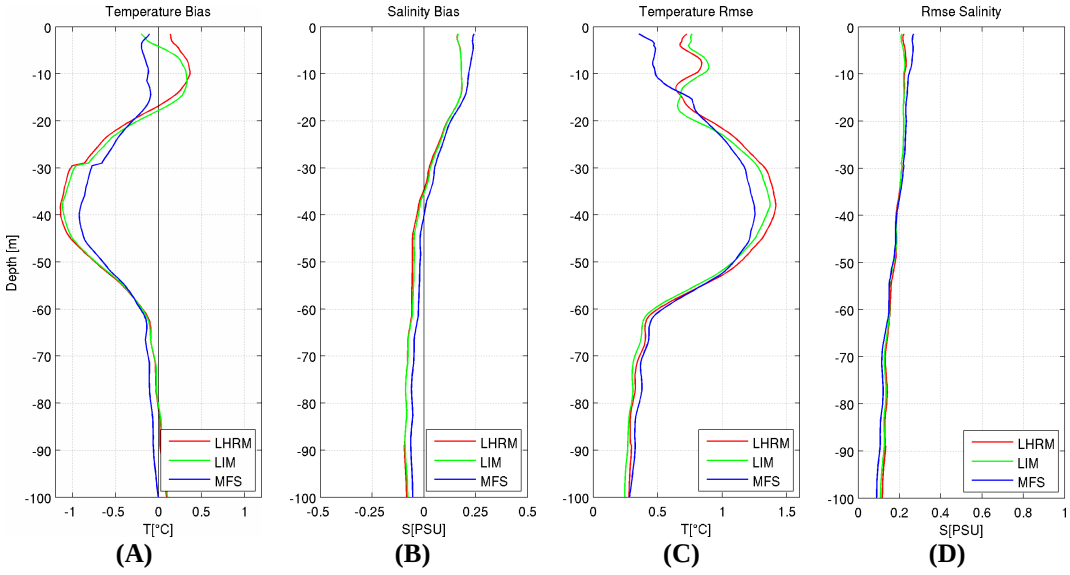

Figure 4.17 Averaged vertical profiles for the upper 100m for: (A) temperature bias, (B) salinity bias, (C) temperature RMS error, (D) salinity RMS error. Blue lines indicate MFS results, green lines LIM results and red lines LHRM results for Exp3A.

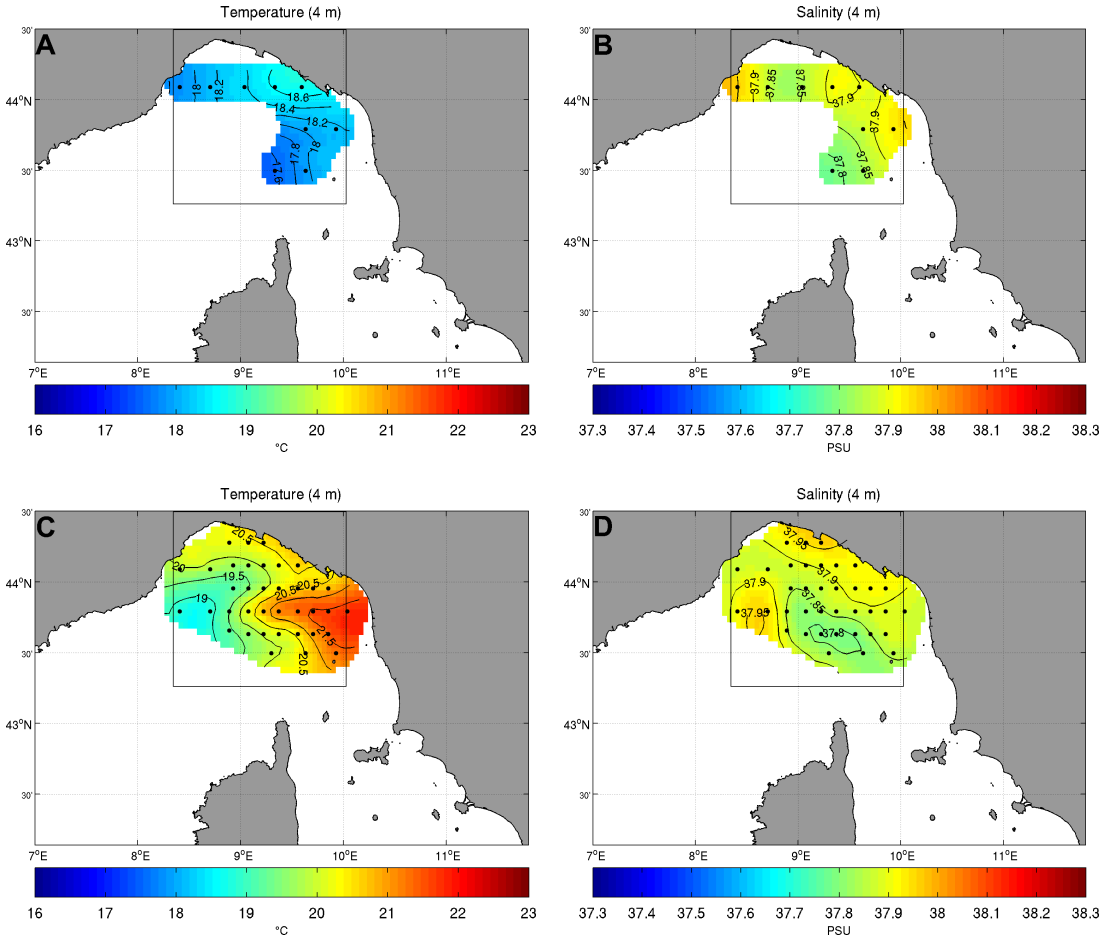

Figure 4.18 Horizontal maps at 4 m depth constructed with the Objective Analysis technique from LHRM simulation: (A) temperature map for 7-9 May, (B) salinity map for 7-9 May, (C) temperature map for 4-18 June, (D) salinity map for 4-18 June. The area enclosed by the solid line represents the LHRM domain.

4.4.2 Eulerian current field

In this section we show the near surface (1.5m depth) velocity fields for the MFS, LIM and LHRM experiments.

Figure 4.19 depicts the current fields for MFS, LIM (Exp1) and LHRM (Exp1A) for 7 and 14 May. Significant differences can be noted between MFS and nested models. MFS is characterized by a reversal of the TC along the eastern side of Corsica (Figure 4.19A) and a strong weakness of the Ligurian-Provençal current along the Ligurian coast; the cyclonic gyre distinctive for the basin is located farther to the coast. The LIM current field for the same day (Figure 4.19C) shows

well-defined cyclonic circulation; the northward TC joins with the WCC north of Corsica and the Elba Island Current, a branch of TC, runs northward into the energetic LPC. The path of the Elba Island Current can be linked to the particular pattern of the salinity shown in the horizontal salinity maps for May (Figure 4.6B and Figure 4.14B). The corresponding LHRM field (Figure 4.19E) reproduces the LIM circulation dynamic with an intensification of the LPC that shifts closer to the Italian coast. The LIM and LHRM current fields for 14 May (Figure 4.19D, F) are characterized by more energetic circulation pattern with respect to MFS (Figure 4.19B).

Similar considerations can be made for the experiments Exp2 and Exp2A: the near surface current field for MFS, LIM and LHRM for 4 June are shown in Figure 4.20A, C, E and for 11 June are represented in Figure 4.20B, D, F. The MFS field is characterized by a less energetic circulation pattern; the cyclonic gyre is located farther from the Ligurian coast and furthermore the TC presents another reversal period. The LIM displays a weakness of the LPC, the TC and the Elba Island Current. The LHRM shows a well-defined and energetic LPC which flows close to the Italian coast. For 11 June in the LIM field (Figure 4.20D) the LPC disappears and small eddies are visible around the cyclonic gyre located at the centre of the basin. However, for the same day in the LHRM simulation the LPC presents intensification (Figure 4.20F).

The current fields for 13 June and 20 June obtained from the experiments Exp3 and Exp3A are shown in Figure 4.21 (Panels A, B, C, D, E, F). The MFS model shows another reversal event in the Corsica Channel and the lack of LPC signal. LIM simulation presents the reversal of TC; the Elba Island Current disappears and develops small mesoscale eddies. However, the LHRM for both days (Figure 4.21E, F) is able to capture the dynamics of the Ligurian circulation representing a well-defined LPC that flows toward the western Mediterranean Sea along the Italian coast.

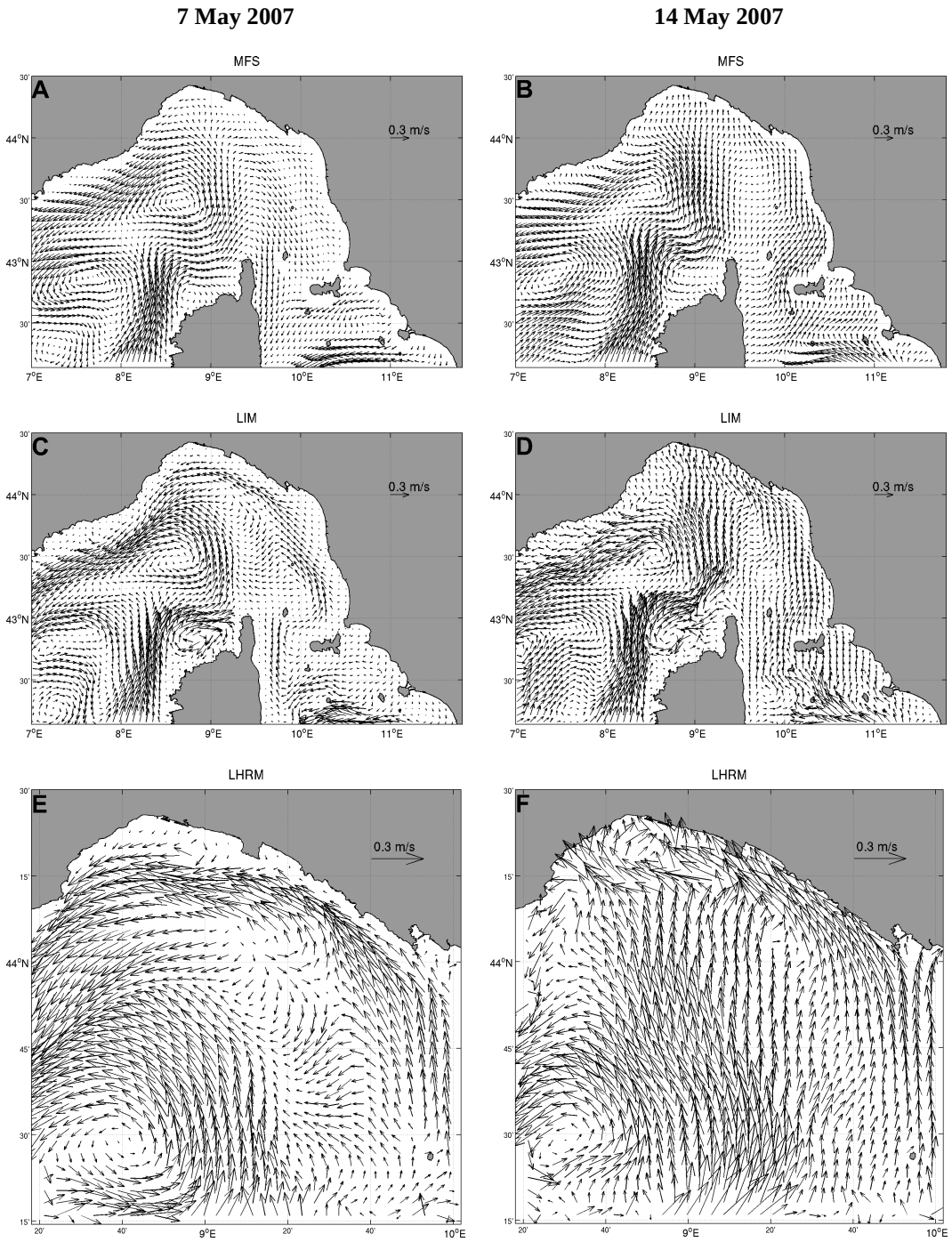

Figure 4.19 Exp1 and Exp1A. Near surface (1.5 m depth) velocity fields [m/s] from MFS (A)-(B), from LIM (C)-(D) and from LHRM (E)-(F). Not all the grid points have been plotted in the LIM and LHRM maps.

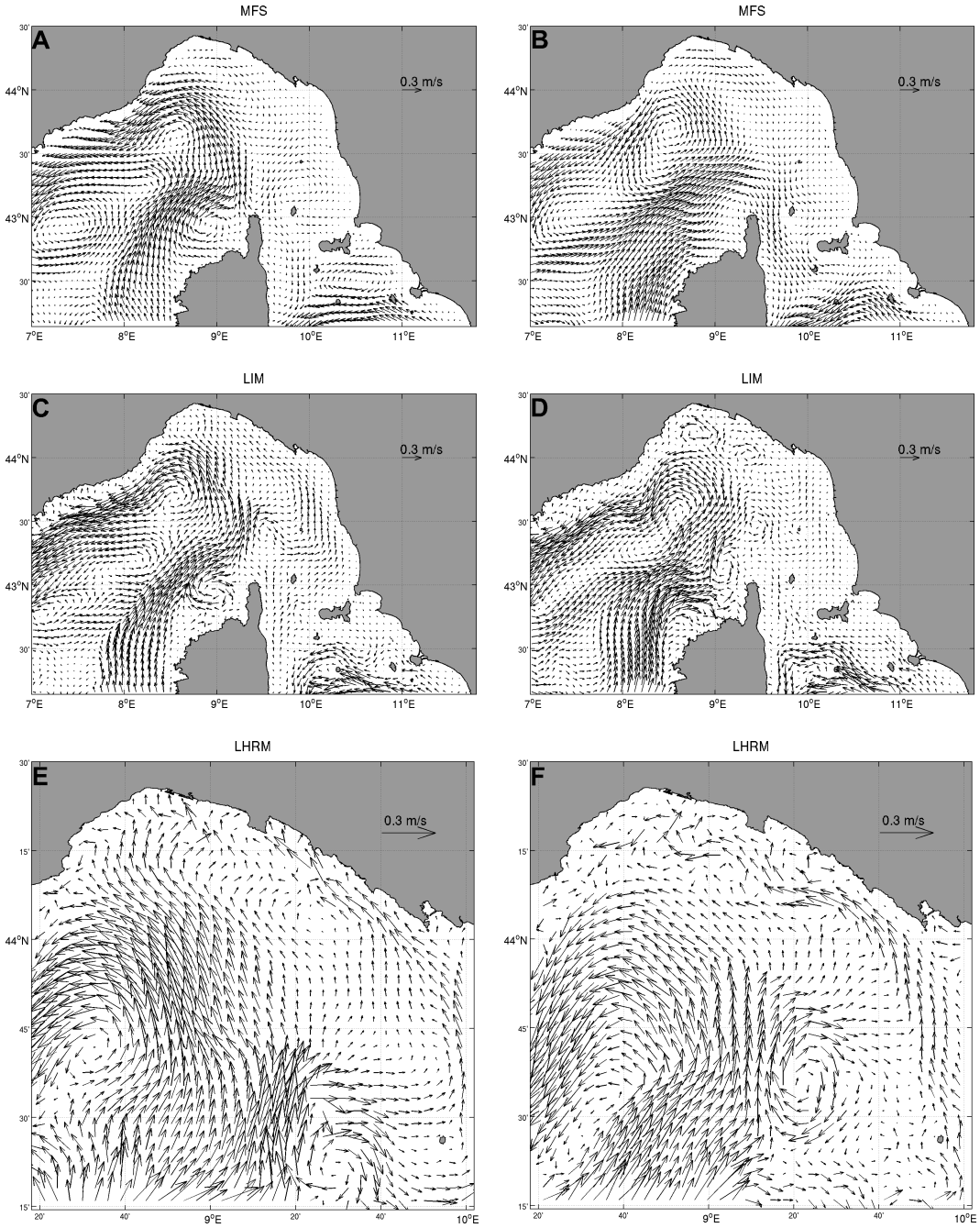

Figure 4.20 Exp2 and Exp2A. Near surface (1.5 m depth) velocity fields [m/s] from MFS (A)-(B), from LIM (C)-(D) and from LHRM (E)-(F). Not all the grid points have been plotted in the LIM and LHRM maps.

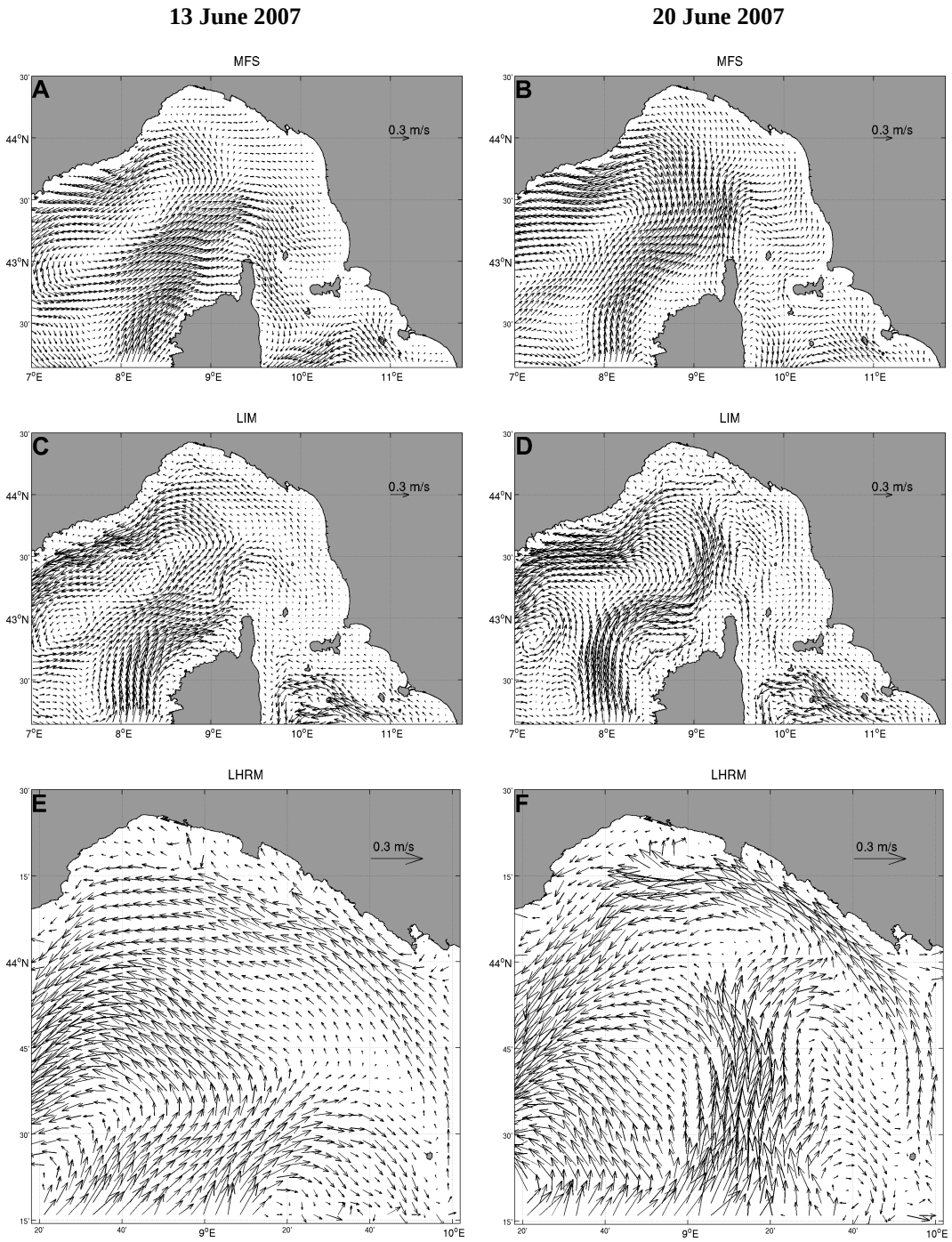

Figure 4.21 Exp3 and Exp3A. Near surface (1.5 m depth) velocity fields [m/s] from MFS (A)-(B), from LIM (C)-(D) and from LHRM (E)-(F). Not all the grid points have been plotted in the LIM and LHRM maps.

4.5 Summary and conclusions

In this chapter we have shown the first results of a modelling effort performed during the MREA experiment in the Ligurian Sea during spring-summer 2007. The main purposes of this experiment were: 1) to collect hydrological data to support the REA methodology; 2) implement and validate a system of nested models embedded in existing operational forecasting systems.

The goal of this work is to understand the improvements in simulating the ocean state deriving from a telescopic nesting modelling approach; the models are nested using a simple one-way offline nesting technique. The parent coarse ocean model with a horizontal resolution of about 6.5 km is part of the Mediterranean Forecasting System (MFS); the model has been downscaled with an intermediate model at horizontal resolution of the order of 3 km (LIM) and an additional submesoscale model of 1 km (LHRM). High-resolution velocity fields provided by nested models are required for application in environmental emergency management such as oil spills and contaminant spreading. The relocatable model can be rapidly implemented in any region of the word and can provide an accurate forecast in a very short time.

The quality of the nested systems has been evaluated by mean of comparisons with observed data in order to have a first estimate of the nested model system capability in reproducing the dynamics of the Ligurian Sea.

During MREA07 two oceanographic cruises were carried out by the Istituto Idrografico della Marina; 12 CTD profiles were collected during the first survey (from 7 to 9 May 2007) and with the second survey (4-6 June, 13-14 June, 18 June) another 46 CTD profiles were obtained. This oceanographic dataset has been useful in investigating the hydrographic structure of the basin.

The vertical profiles of temperature and salinity show the existence of two superimposed layer of marine water: the surface MAW and MLIW (200-800m). The horizontal distributions of temperature at a depth of 4 metres show a stable thermal front that divides the warmer coastal water from that of the central area of the basin. However, the salinity maps show a variable salinity gradient: in May

we find higher salinity close to the Italian coast, while in June the salinity increases in the centre of the basin.

The comparison between observed and LIM-simulated salinity profiles shows a positive salinity bias in the surface. The model error is a direct consequence of the initialization from MFS: the salinity does not significantly change during the seven days of simulation and consequently remains close to the initialization fields. Due to the fact that all models are driven by the same atmospheric forcing and due to the relatively short integration time, the quality of the LIM relocatable model is primarily constrained by the quality of the MFS.

The circulation features simulated with LIM are consistent with the known dynamics of the Ligurian Sea. The model is able to reproduce successfully the large-scale cyclonic gyre; the LPC and TC are well-represented.

The second nesting model LHRM gives a similar behaviour to LIM in the temperature and salinity fields but the high resolution of the current field helps to ameliorate the representation of the LPC, which is well-defined in the velocity maps. LHRM is capable of capturing the dynamics in the shelf region which are not adequately resolved by the coarser model.

We can conclude that the nested models are working properly even if we need to ameliorate the vertical model structure; in particular, the vertical mixing affecting the upper layer introducing atmospheric forcing at higher resolution.

Chapter 5

Maritime Rapid Environmental Assessment Experiment in the Ligurian Sea, Part 2: Drifter Trajectory Simulation Using a Relocatable Nested System

5.1 Introduction

The Maritime Rapid Environmental Assessment (MREA07) experiment carried out in the Ligurian Sea in spring-summer 2007 focused on: (1) collecting oceanographic data to calibrate and validate the MREA concept for environmental applications in open sea and coastal areas; (2) implementing and validating a relocatable model system nested in a basin scale operational ocean model and (3) demonstrating the utility of an MREA model system for contaminant dispersal forecasting.

The first and second goals have been discussed and analyzed in Chapter 4, where we have demonstrated the implementation of a nested model system in the Ligurian Sea embedded in an operational existing general circulation model. The third objective will be discussed in this chapter. Contaminant dispersal will be mimicked by the movement of a cluster of drifters released close to each other and then freely drifting at the surface.

The main purpose of this chapter is to evaluate the ability of the relocatable models to predict particle spreading in the ocean using the drifter dataset collected

during MREA07. The spatial resolution of the current field provided by the oceanographic model plays an important role in representing the important physical processes. Coarse resolution models are not usually capable of resolving the relevant scales of motion and may consequently be inadequate for describing the drift of floating objects. Our hypothesis is that higher resolution models could increase the predictability of particle trajectories. However, it is also true that increasing the resolution without an accurate knowledge of the initial condition could produce a loss of predictability. This is why observations have been collected to be assimilated in the large-scale model in order to increase the realism of the initial condition.

The MREA07 experiment offered a unique opportunity to test the relocatable model as a tool in the Lagrangian prediction problem. The relocatable model can be rapidly deployed in emergency areas and it could produce high resolution forecasts starting from the forecast and analysis products provided by the basin scale operational forecasting system.

This work is organized as follows: Section 2 provides information on the drifter dataset released during the MREA07 experiment and on the Eulerian current field used for Lagrangian simulations. A description of the Lagrangian model is given in Section 3. Section 4 shows the Lagrangian statistics. The experiments performed are presented in Section 5, while the results are shown in Section 6. Summary and conclusions follow in Section 7.

5.2 Data sources

5.2.1 Drifter data

Surface drifters were deployed in the Ligurian Sea in May and June 2007 during the MREA07 and LASIE (Ligurian Air-Sea Interaction Experiment) experiments by the Italian Navy Vessel Galatea and R/V Urania. Three drifter clusters, each consisting of five drifters, were launched in three different periods in the vicinity

of the ODAS buoy (9.17° E 43.79° N). For simplicity, in the discussion we call the three clusters: clusterA, clusterB and clusterC.

ClusterA was launched on 14 May; clusterB was deployed on 17 June; cluster C was released on 22 June. The deployment position and 12-day trajectories for each cluster are shown in Figure 5.1.

The drifters employed were provided by NATO/SACLANT Undersea Research Centre (NURC) and by Istituto Nazionale di Oceanografia e di Geofisica sperimentale (OGS). The drifter design is similar to that used in the Coastal Dynamics Experiment (CODE) in the early 1980s (Davis, 1985); a detailed description can be found in Poulain (1999) and Ursella *et al*. (2006). Comparison with current meter measurement (Davis, 1985) showed that the drifters follow the current to within 3cm/s, even during strong wind conditions.

These drifters have been localized by Global Positioning System (GPS) at hourly intervals and their data telemetered via the ARGOS system. Quality control of the drifter positions has been carried out with automatic statistical and manual procedures (Ursella *et al*., 2006) and surface velocities have been calculated as finite differences of the position data.

In Figure 5.1 we notice that, while clusterA turns southward with intense inertial oscillation loops (the time scale of inertial oscillations is about 17 hours at these latitudes) the other two clusters take the north-westward path, similar to the direction of the flow field investigated in PartI (Chapter 4). In particular, clusterC seems to be trapped in a narrow intense jet very close to the coasts, which could be very hard to produce with the large-scale numerical models. ClusterA starts really to disperse after 7 days. The other two clusters, however, do not seem to evidence any dispersal, probably due to the coastal boundary jet intensification.

5.2.2 Surface currents

The surface current fields used for Lagrangian simulations have been provided by the MFS and nested models described in PartI (Chapter 4). For our Lagrangian experiments we will use the MFS analysis hourly snapshots.

The nested system is based on two relocatable models implemented in the Ligurian Sea with two successive zooms. The first system implemented is the Ligurian Intermediate Model (LIM) with 3 km horizontal resolution and the second system is the finer Ligurian High Resolution Model (LHRM) that reaches 1 km of horizontal resolution.

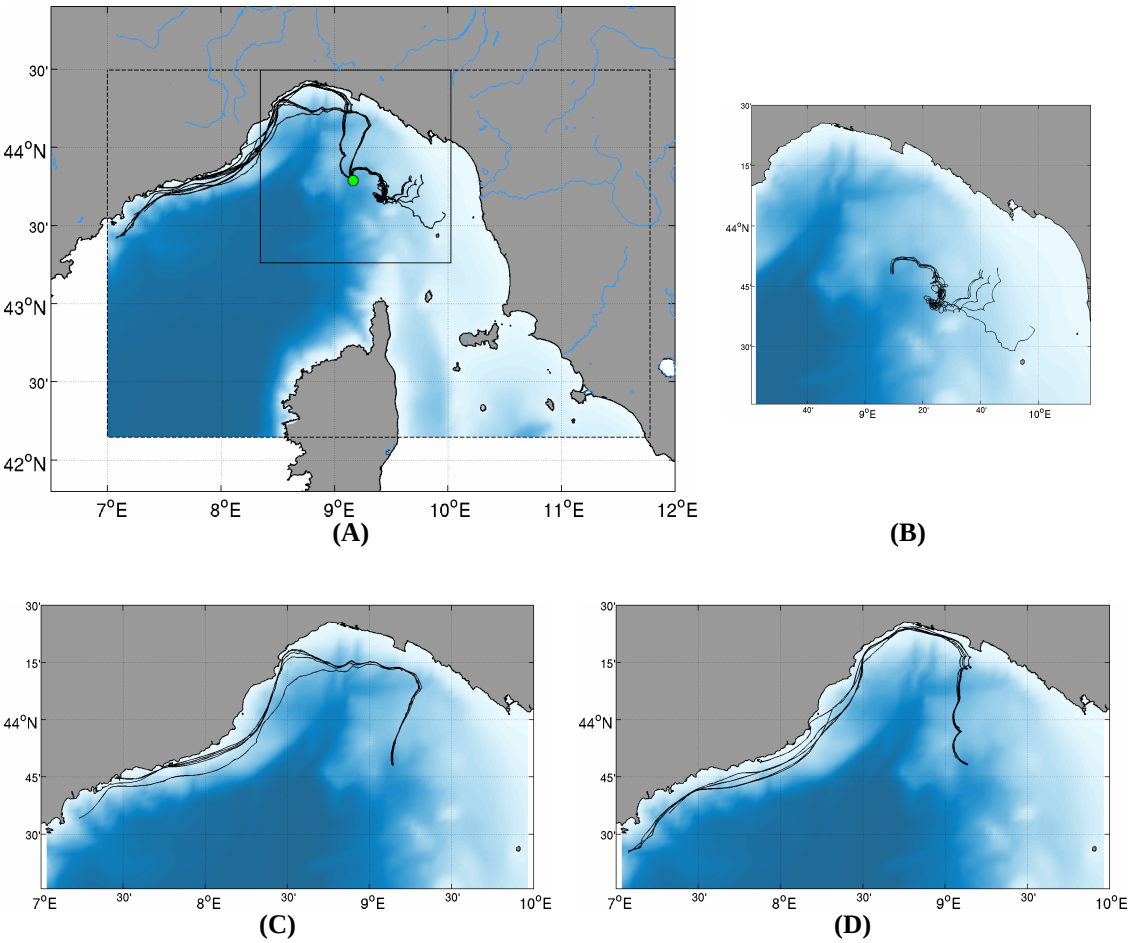

Figure 5.1 (A) 12-day trajectories of the 15 drifters released during the MREA07 and LASIE experiments in the Ligurian Sea and domains of the two nested models represented with solid and dashed lines. Zooms of trajectories of the three clusters: (B) clusterA, (C) clusterB, (D) clusterC.

LIM and LHRM are based on the Harvard Ocean Prediction System (HOPS) model system. The core of HOPS is a free-surface primitive equation model with prognostic variables arranged on an Arakawa B grid and sigma-coordinates in the

vertical direction; a detailed description of HOPS can be found in Robinson (1996, 1999) and Lozano *et al*. (1996).

Exhaustive information about LIM and LHRM implementation is given in Chapter 4. The three models are coupled by simple one-way, offline nesting technique; the finer grid model initial and boundary conditions are interpolated from the coarse grid model without any feedback from the fine to the coarse system. The coarse MFS model provides initial and boundary condition to LIM which in turn provides initial and boundary condition to LHRM. The three models are forced to the surface with the atmospheric forcing European Centre for Medium-Range Weather Forecasts (ECMWF) with a 0.5° horizontal resolution and temporal frequency of 6 hours provided by the Italian National Meteorological Office.

5.3 Trajectory model

The Lagrangian simulations have been performed with a Lagrangian dispersion model which describes the drifters spreading with a discrete number of mass-less particles released from a source point. The movement of individual particles is given by the summation of successive particle displacements; each of these displacements is described by a deterministic and a stochastic part. The first component represents the advection associated with the Eulerian current field while the second part describes the sub-grid scale diffusion due to unresolved scales in the Eulerian model. To simulate this particle turbulent motion, we use a stochastic process parameterization. In our trajectory model we then write:

$$d\vec{x} = \vec{U}dt + \sqrt{2K_{\vec{v}}dt}\vec{\xi} \tag{5.1}$$

where $d\vec{x} = (dx, dy)$ is the displacement in the horizontal plane, $\vec{U}$ is the Eulerian velocity field, dt the Lagrangian timestep, $K_{\vec{v}}$ is a turbulent diffusion coefficient and $\vec{\xi}$ is a randomly generated number with values between 0 and 1. The key issue is to estimate the proper $K_{\vec{v}}$ for our model grids.

5.4 Estimating turbulent velocity statistics

In this section Lagrangian velocity statistics are computed using oceanographic drifter data and Eulerian model velocities to estimate the turbulent diffusion coefficient used in equation (5.1).

Taylor (1921) demonstrated that the turbulent dispersion of particles in homogeneous turbulent flows can be evaluated using the autocorrelation function of the Lagrangian velocity field.

In order to quantify the diffusivity we will compute the difference between the model velocities and the drifter ones making the assumption that this difference is due to the stochastic part of the flow field not resolved by the model.

The fluctuating velocity for the zonal component (u') and meridional component (v') is then computed as the difference between drifter velocity (u, v) and modelled velocity (U_M, V_M) as:

(5.2) $$u' = u - U_M \ ; \ v' = v - V_M \ .$$

The modelled velocities are hourly snapshot values provided by three numerical models: MFS, LIM and LHRM; the bilinear interpolation of the Eulerian velocity from the grid model to the location of a drifter has been performed using the four grid points around the position. The average time series of u' and v' calculated for each drifter have been used to compute the autocovariance function and estimate the diffusivity coefficient.

The relations used for the autocovariance (R) and diffusivity (K) are:

(5.3) $$R_u(\tau) = \left\langle u'(t)u'(t+\tau) \right\rangle \ ; \ R_v(\tau) = \left\langle v'(t)v'(t+\tau) \right\rangle$$

(5.4) $$K_u = \int_0^\tau R_u(\tau) d\tau \ ; \ K_v = \int_0^\tau R_v(\tau) d\tau$$

where τ is the time lag.

The autocovariance functions and the diffusivities obtained from clusterA using MFS, LIM and LHRM current fields are depicted in Figure 5.2 panels A,B,C respectively. The autocovariances and diffusivities show a slight anisotropy with the zonal component more energetic than the meridional component; the

autocovariances also present a rapid exponential decay at short timescales. For all three cases the diffusivity converges to asymptotic value. For the MFS model we obtain $K_{\bar{v}} \approx 1.6x10^6 cm^2/s$, for LIM $K_{\bar{v}} \approx 1x10^6 cm^2/s$ and for LHRM $K_{\bar{v}} \approx 0.8x10^6 cm^2/s$. The $K_{\bar{v}}$ value is correlated with the horizontal grid resolution of the Eulerian model; increasing the resolution of the current field the diffusivity coefficient decreases.

In the future we will calculate the diffusion coefficients for each model without doing trajectory differences in an attempt to estimate each model subgrid scale parameterization.

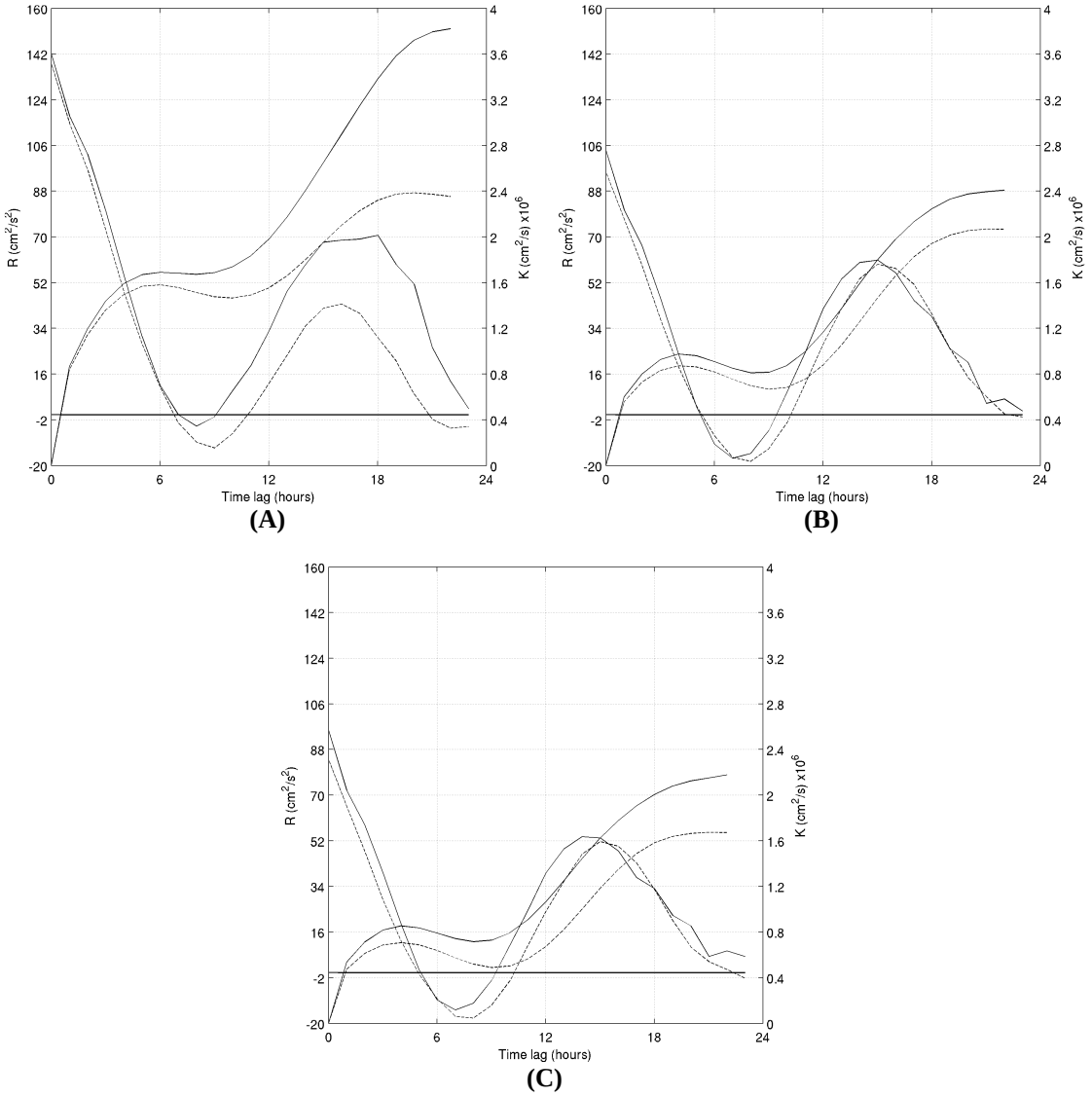

Figure 5.2 Autocovariance functions [R] and diffusivities [K] resulting from clusterA using MFS (A), LIM (B) and LHRM (C) current fields. The continuous line refers to the zonal component and dotted lines to the meridional component.

5.5 Experiment design

In this section we investigate the sensitivity of the Lagrangian trajectory model as a function of the horizontal resolution of the Eulerian velocity field. The goal is to evaluate the ability of the relocatable models to simulate the drifter movement. The LIM and LHRM have been integrated for three different periods for which

the drifter data are available. Initial and boundary conditions for LIM simulation have been given by MFS analysis and initial and boundary conditions for LHRM have been provided by LIM output. The hourly snapshot current fields provided by MFS, LIM and LHRM have been used to drive the Lagrangian trajectory model in order to reproduce the trajectories of clusterA, clusterB and clusterC (Figure 5.1).

The impact of the Eulerian horizontal resolution field on particle trajectories has been quantified by means of comparisons of the observed drifters trajectories to those simulated.

The Lagrangian experiments have been carried out by releasing a cluster of twenty-five particles evenly distributed in a square of 5 km each day along the trajectories of the drifters, integrated for 5-day periods.

The results have been analyzed with qualitative and quantitative comparisons. The first test is a qualitative comparison between the drifters and simulated trajectories. The second test is a quantitative comparison in order to quantify the Lagrangian simulation accuracy. Accuracy has been evaluated considering the ensemble average distance error ($\langle d_E \rangle$) between the drifter position and the centre of mass of the simulated cluster with a temporal frequency of 1 hour:

$$\langle d_E(n\Delta t)\rangle = \frac{1}{N_T}\sum_{i=1}^{N_T}\left(\left|x_D(n\Delta t) - x_M(n\Delta t)\right|\right) \tag{5.5}$$

where N_T represents the total number of trajectories computed, x_D and x_M are the drifter position and the centre of mass position of the cluster respectively, n is the total number of timestep with Δt the timestep of the Lagrangian trajectory model.

One additional experiment has been added to investigate the effect of the horizontal resolution of the atmospheric forcing on trajectory calculations. In this experiment the LIM has been forced to the surface with a high horizontal resolution atmospheric forcing. The atmospheric forcing is from the COSMO-ME model with a horizontal resolution of 7 km and 6hr temporal frequency provided by the Italian National Meteorological Office (Bonavita and Torrisi, 2005). The

LIM current field has been used to drive the Lagrangian simulations to reproduce the movement of the three clusters.

5.6 Results

The quality and the accuracy of the simulated trajectories have been explored with qualitative and quantitative comparisons. Analysis has been performed for clusterA, clusterB and clusterC, deployed during the MREA07 experiment.

5.6.1 Qualitative comparison of trajectories

As a first test, a qualitative comparison between the real and simulated trajectories is carried out. We report here only the qualitative results obtained with one drifter of clusterA deployed in May. Figure 5.3 shows the simulated trajectories computed using the MFS current field. We note that the numerical trajectories, integrated with the coarse resolution model, are not able to reproduce the displacement of the drifter. Initially, the drifter turns southward while the numerical trajectories take the north-westward direction with large velocities compared to those of the drifters. Furthermore, in the final path of the drifter the numerical trajectories move southward more quickly than the drifter.

Figure 5.4 depicts the Lagrangian simulations driven by the LIM current field. We can note a slight improvement in the simulations. Initially the numerical trajectories turn southward following the direction of the drifter and they have velocity values comparable to those of the drifters.

The numerical trajectories computed with the LHRM current field are shown in Figure 5.5; the results are very similar to those obtained with the LIM current field. The simulated trajectories capture the drifter movement in its initial path successfully, while there is some discrepancy in the final part of the drifter.

The performance of these Lagrangian simulations has been quantified with statistical analysis shown in the next sections.

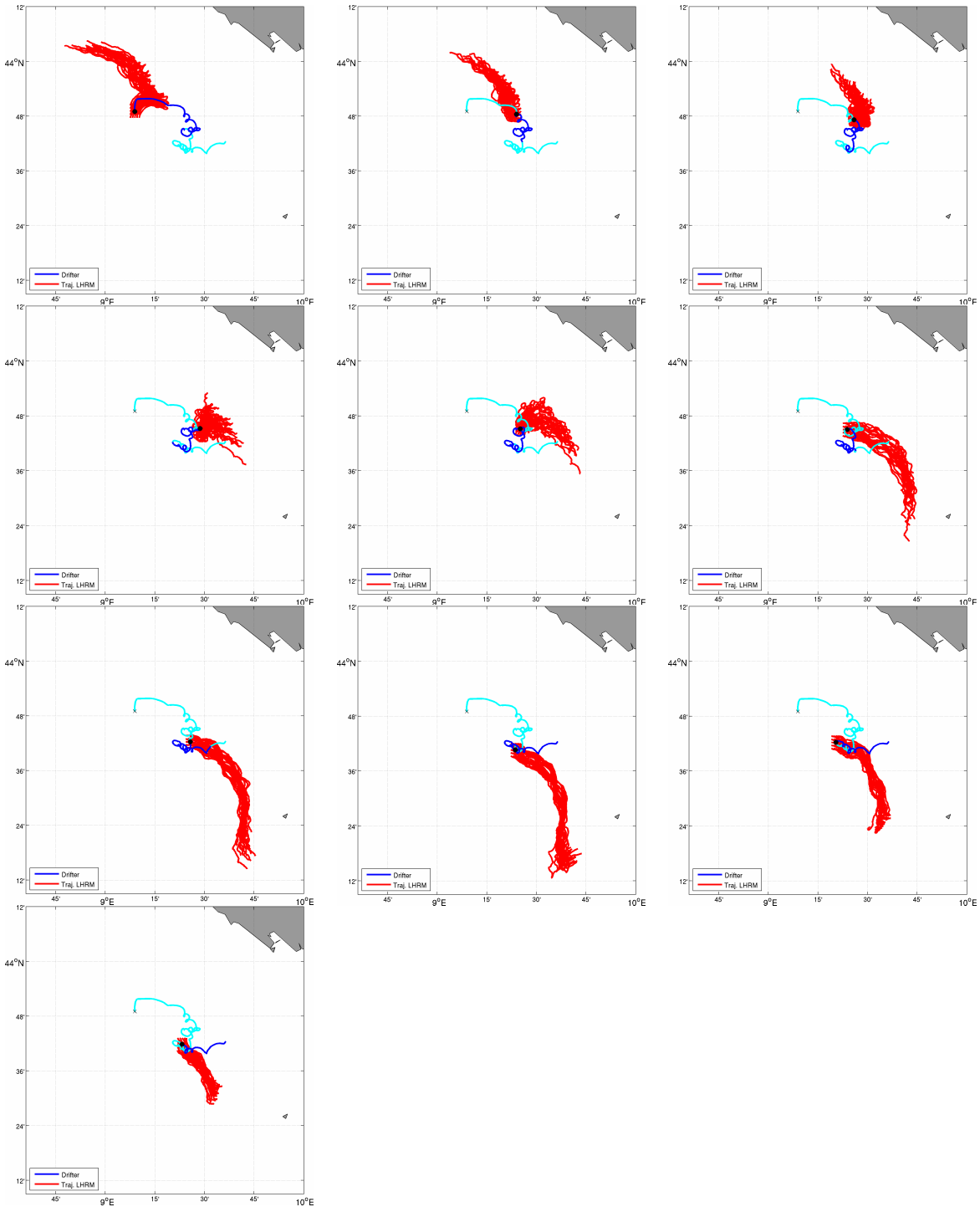

Figure 5.3 Five-day numerical trajectories (red line) of 25 particles released along one drifter trajectory of clusterA computed with MFS hourly snapshot fields. The blue line indicates the five-day drifter trajectory; the cyan line is the total drifter trajectory; the star marks the initial numerical trajectories and the cross marks the initial drifter total trajectory.

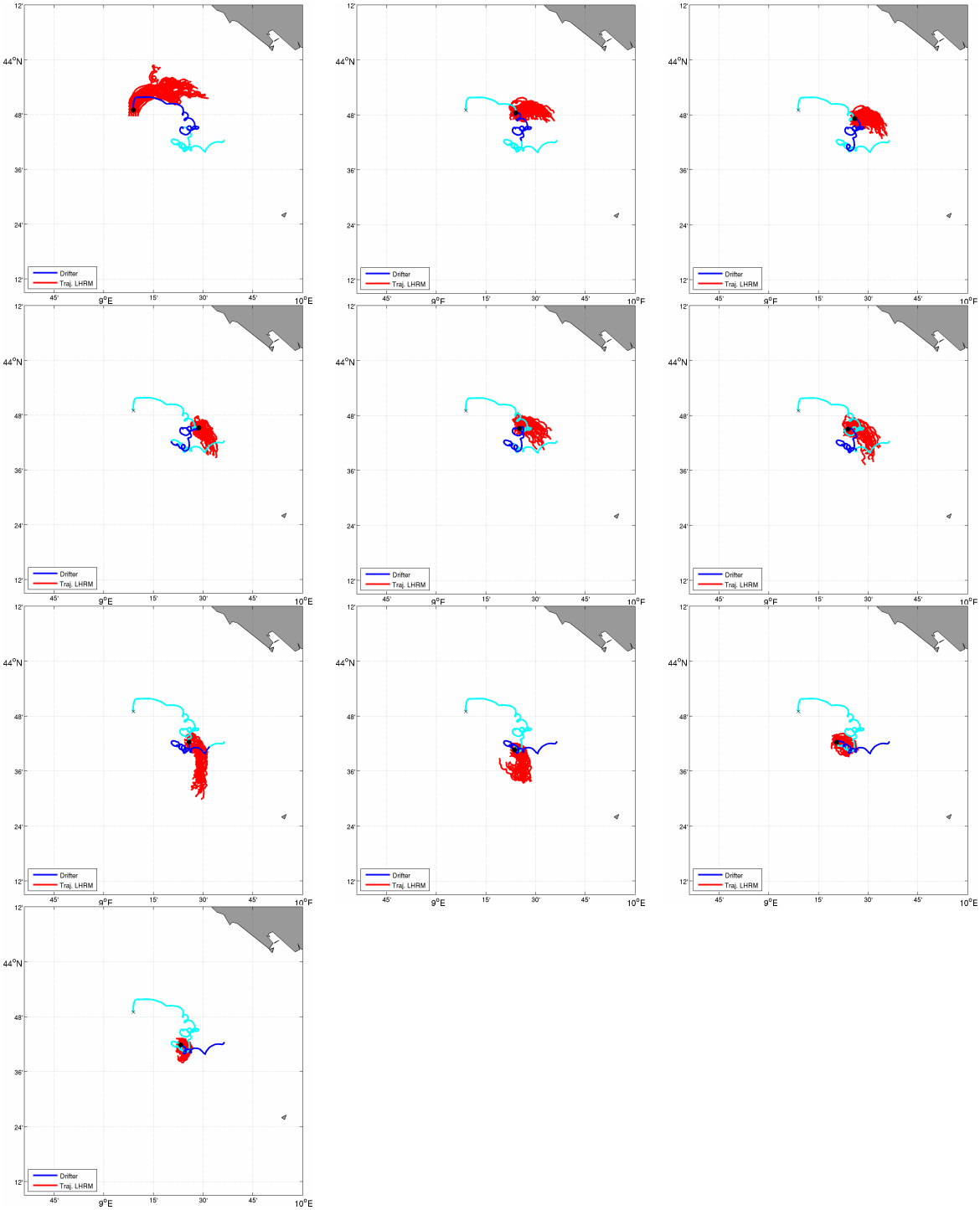

Figure 5.4 Five-day numerical trajectories (red line) of 25 particles released along one drifter trajectory of clusterA computed with LIM hourly snapshot fields. The blue line indicates the five-day drifter trajectory; the cyan line is the total drifter trajectory; the star marks the initial numerical trajectories and the cross marks the initial drifter total trajectory.

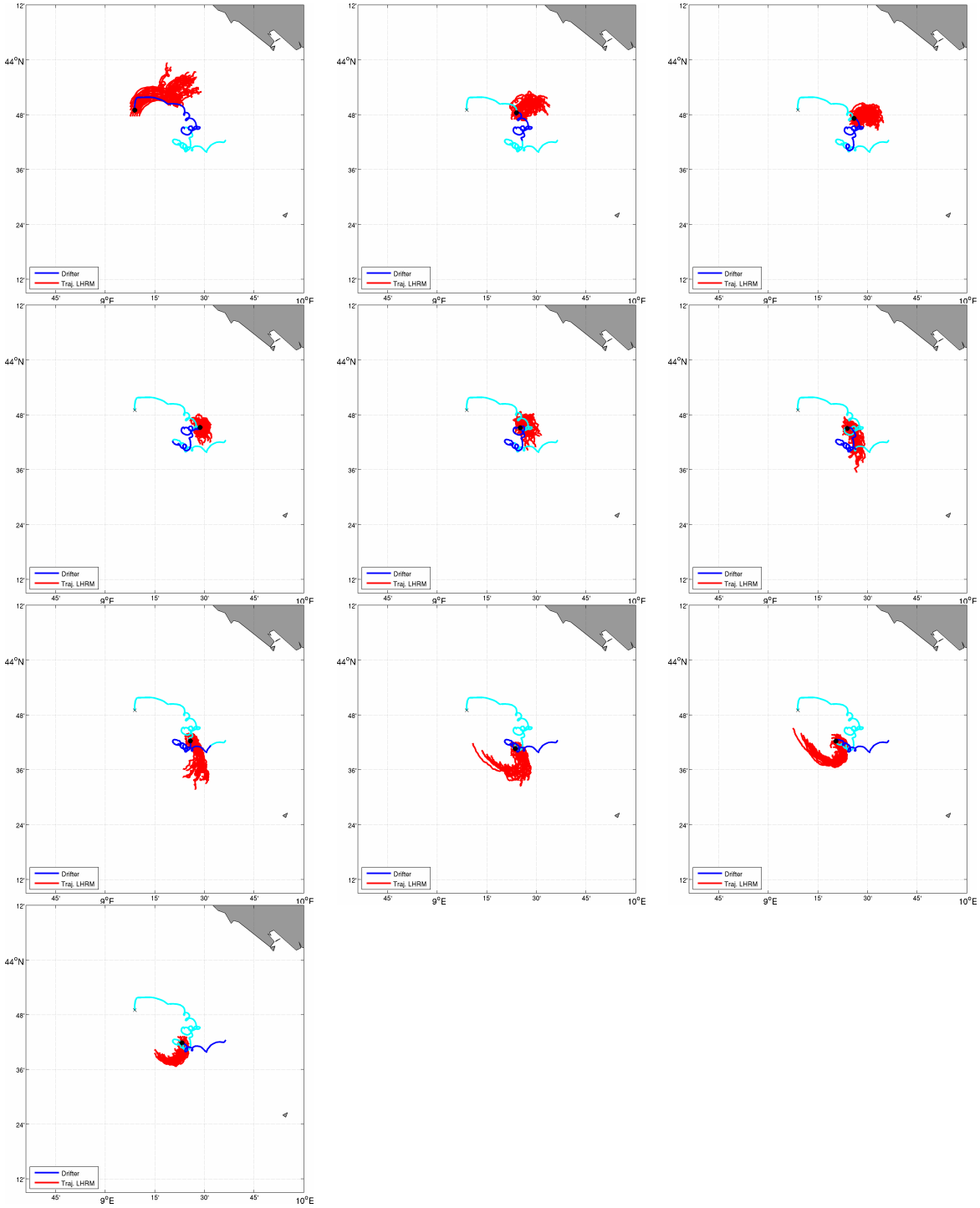

Figure 5.5 Five-day numerical trajectories (red line) of 25 particles released along one drifter trajectory of clusterA computed with LHRM hourly snapshot fields. The blue line indicates the five-day drifter trajectory; the cyan line is the total drifter trajectory; the star marks the initial numerical trajectories and the cross marks the initial drifter total trajectory.

5.6.2 Quantitative comparison of trajectories

In this section we show the quantitative measure of the sensitivity of Lagrangian simulation as a function of the Eulerian field resolution.

The ensemble average distance errors ($\langle d_E \rangle$) for each cluster are shown in Figure 5.6A,B,C in function of the simulation time (days). For all clusters the distance error increases linearly with the integration time in agreement with our previous study (see Chapter 3).

For clusterA (Figure 5.6A), the Lagrangian simulations carried out with the MFS current field provide high $\langle d_E \rangle$, the distance error after the first day is $\langle d_E \rangle \approx 10km$, after 3 days becomes $\langle d_E \rangle \approx 25km$ and reaches approximately $30km$ after 5 days. The LIM and LHRM experiments, however, give instead small $\langle d_E \rangle$, after one day $\langle d_E \rangle \approx 5km$, after 3 days $\langle d_E \rangle \approx 10km$ and after 5 days of integration $\langle d_E \rangle \approx 15km$. We conclude that for clusterA the higher resolution current field improves the Lagrangian trajectory simulation, even though there are not evident improvements with the current field at 1km provided by LHRM.

The statistical results for clusterB are shown in Figure 5.6B. We can note a slight improvement in the Lagrangian simulations driven by the LIM and LHRM current fields after the third day of integration. After 5 days of integration MFS provides a value of $\langle d_E \rangle \approx 100km$ while the simulations with LIM and LHRM give a $\langle d_E \rangle \approx 50km$.

The last analysis has been performed with clusterC (Figure 5.6C); in this case we obtain high $\langle d_E \rangle$ values using the three Eulerian current fields; for this cluster an improvement of the prediction with a higher horizontal resolution model is not evident. This probably depends to the position of the drifters; most of the trajectories closely follow the coastline and the Eulerian models do not resolve the shelf dynamics accurately.

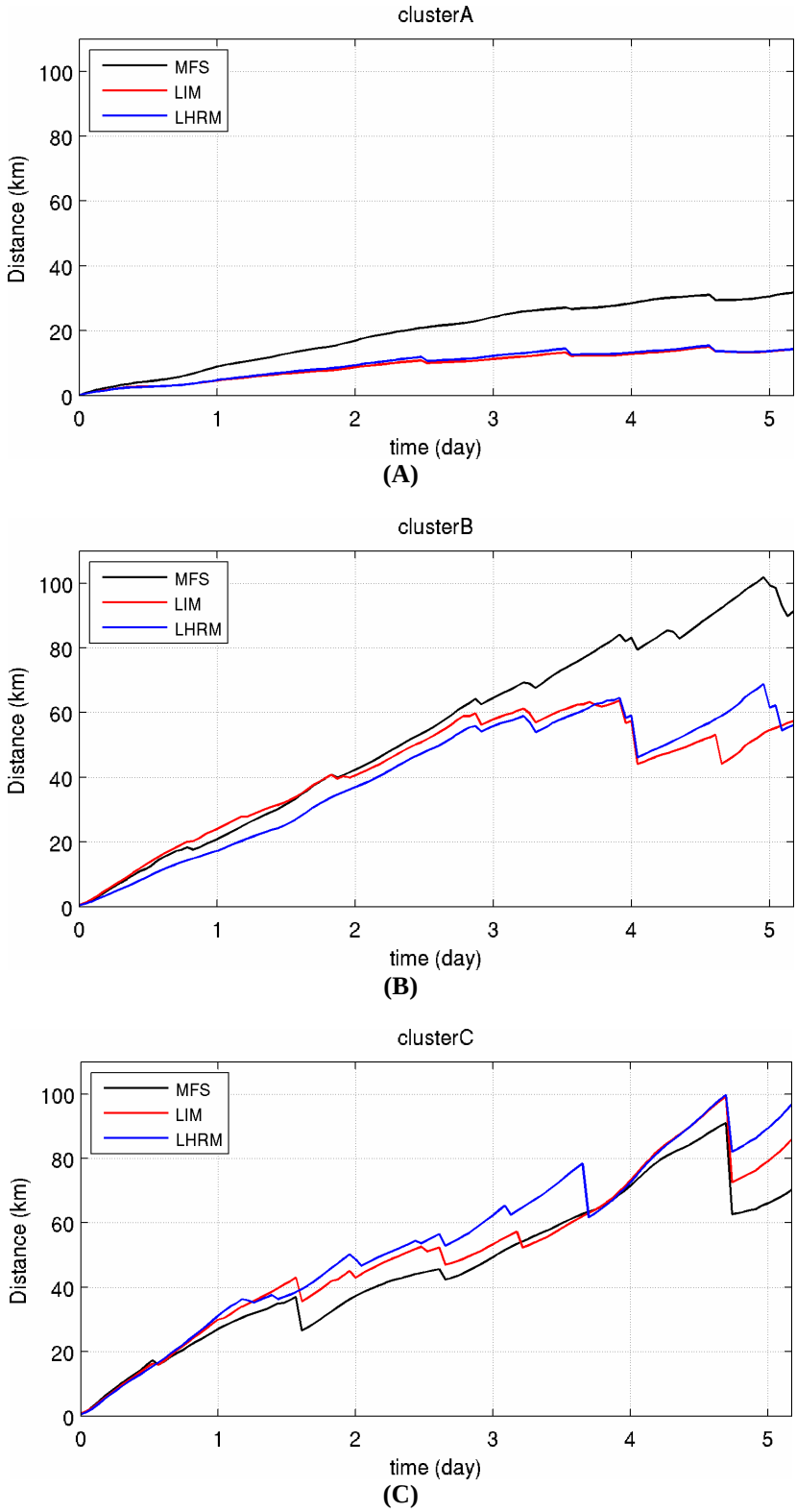

Figure 5.6 Ensemble average of the distance errors between drifters and simulated trajectories in function of the simulation time for: (A) clusterA, (B) clusterB, (C) clusterC.

5.6.3 Sensitivity of trajectory model to atmospheric forcing

In this section we show the qualitative and quantitative results obtained from Lagrangian trajectory simulations driven by LIM output with high-resolution atmospheric forcing.

Figure 5.7 depicts the numerical trajectories for one drifter of clusterA. We can note that initially the numerical trajectories represent the drifter movement well and show intense inertial oscillation loops. The atmospheric forcing at high resolution seems to improve the Lagrangian simulation. This improvement is not so evident from the statistical analysis. The quantitative measure of Lagrangian simulation performance is shown in Figure 5.8; the distance error values obtained using LIM forced by ECMWF and COSMO-ME are compared. For this quantitative comparison a great improvement caused by changing the resolution of the atmospheric forcing it is not evident.

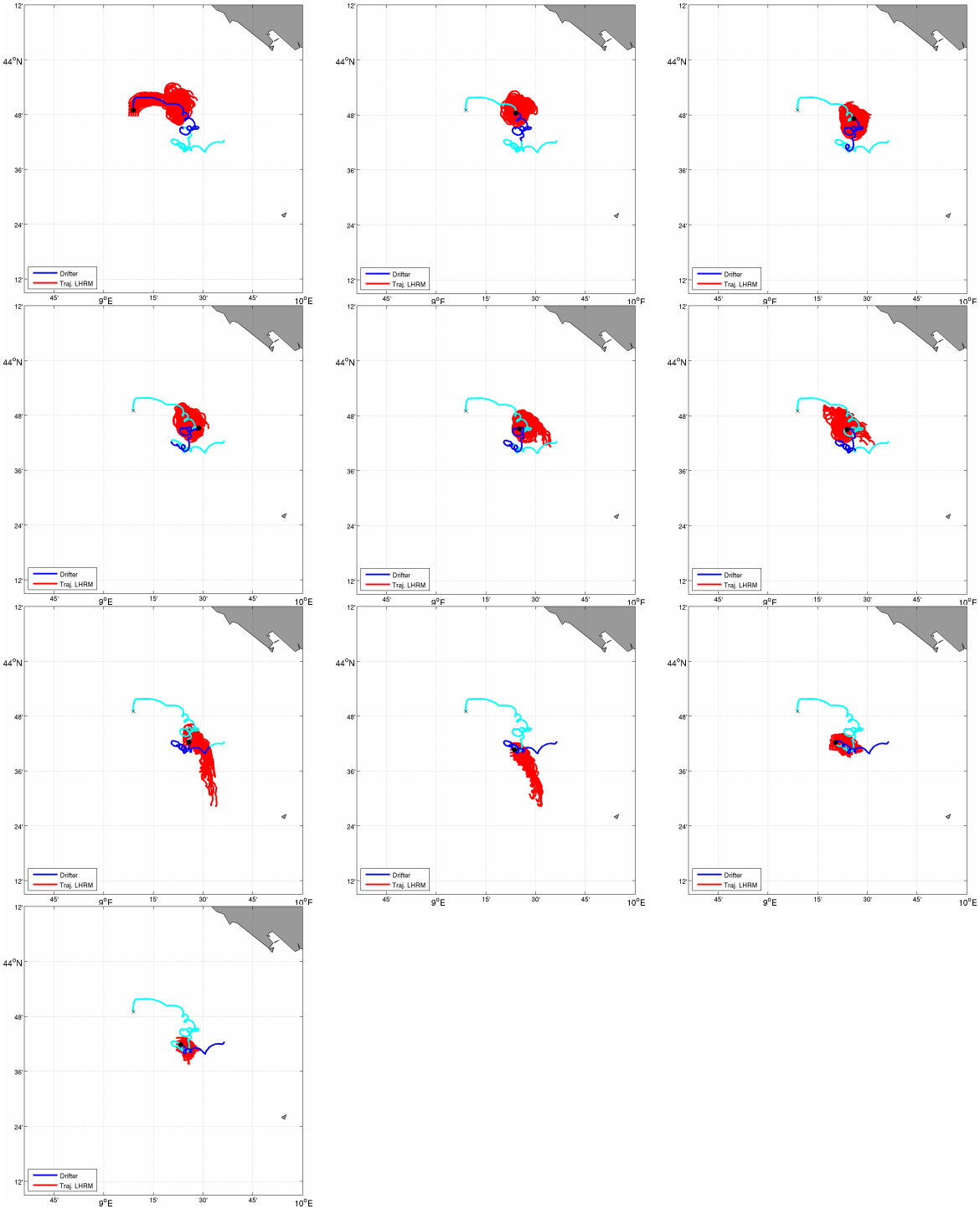

Figure 5.7 Five-day long numerical trajectories (red line) of 25 particles released along one drifter trajectory of clusterA computed by LIM hourly snapshot fields forced by high-resolution atmospheric forcing. The blue line indicates the five-day drifter trajectory; the cyan line is the total drifter trajectory; the star marks the initial numerical trajectories and the cross marks the initial drifter total trajectory.

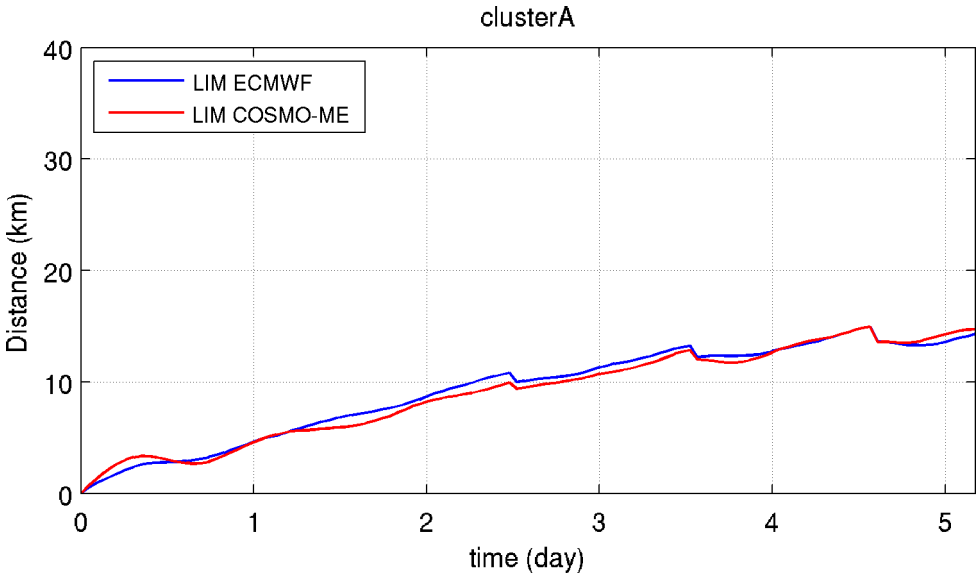

Figure 5.8 Ensemble average of the distance errors between drifters and simulated particles in function of the simulation time for: (A) clusterA.

5.7 Summary and Conclusions

In this study our goal has been to evaluate the ability of the relocatable models to simulate particle spreading in the ocean using the drifter dataset available. The hypothesis formulated is that high-resolution models could increase the predictability of particle trajectories.

This study has been performed in the framework of MREA07 experiment, which took place in the Ligurian Sea in spring-summer 2007. A nested model system has been implemented in the Ligurian Sea embedded in the operational MFS. The MFS system releases current field for the whole Mediterranean Sea with a resolution of approximately 6.5 km. This horizontal resolution could represent a limit for the Lagrangian trajectory simulation. The relocatable model represents a possible solution to this problem: it can be rapidly deployed in limited area and provide fine resolution forecasting at short notice starting from the MFS products. The first relocatable model implemented is LIM with 3km of horizontal resolution and the second model is LHRM, which reaches 1km of horizontal resolution; the models are nested using a simple one-way offline nesting technique.

The impact due to the horizontal resolution of the Eulerian field on the particle trajectory simulation has been investigated by means of comparisons between drifter and numerical trajectories. The drifter trajectories have been simulated with a Lagrangian trajectory model.

During MREA07 three clusters each consisting of five drifters were launched in the Ligurian Sea in three different periods. The first cluster (clusterA) was launched on 14 May, the second cluster (clusterB) was deployed on 17 June and the third cluster (clusterC) was released on 22 June. The paths of the drifters are very different: clusterA moves southward with intense inertial oscillation loops while the other two clusters take the north-westward direction driven by a strong current.

In the first part of the study this drifter dataset has been used to estimate the turbulent diffusion coefficient used by the Lagrangian trajectory model to describe the sub-grid scale diffusion. We found that the diffusivity values for clusterA are in the range $0.8-1.6x10^{6}cm^{2}s^{-1}$; these value are too large to use in the Lagrangian trajectory model. We need in the future to apply different methods to estimate the diffusion coefficients from observed drifters.

In the second part of the study, the predictability of the Lagrangian model has been analyzed as a function of the horizontal resolution of the Eulerian model. The trajectory model has been forced with MFS, LIM and LHRM hourly snapshot current fields in order to reproduce the observed drifters. The qualitative and quantitative comparisons between real drifters and simulated trajectories show that the current field at higher resolution does not always improve Lagrangian predictability. LIM and LHRM are able to improve the simulation of clusterA, while for clusterB and clustedC the improvement is not evident, probably due to drifter trajectories closely following the coastline.

Lagrangian predictability can be increased using an atmospheric forcing at higher resolution that improves the simulation of the Eulerian field provided by the relocatable model.

Future work will include testing the relocatable models in other ocean regions using the drifter dataset available and with an atmospheric forcing at a higher resolution.

Chapter 6

Conclusions

In this work we presented the development and the application to real case studies of a lagrangian trajectory model to simulate and forecast the passive tracers dispersion in the sea. We considered the tracers as mass-less water parcels, leaving for future studies the development of a trajectory model for active particles like oil or other chemical pollutants in the sea. Initially the effort has been devoted to the development of a validated numerical trajectory model that is at the basis of practical applications such as the management and prevention of environmental impacts from pollutant spreading and/or support for efficient search and rescue operations. Our main motivation has been to design a set of numerical tools to be coupled to marine hydrodynamics models simulating the eulerian currents in the ocean and marine areas. The dispersion of tracers is then reduced to the tracking of many particles in the sea, advected by currents and dispersed by turbulence.

Two important aspects of the Lagrangian model have been dealt with this thesis: the implementation and validation of different particle trajectory numerical models, their coupling with eulerian models and the parameterization of turbulent diffusion. In a second part, the Maritime Rapid Environmental Assessment (MREA) concepts have been enlarged to relocatable models nested within operational oceanographic systems and coupled with particle-tracking algorithms in order to extend the limit of predictability of particle trajectories in the sea.

In the first part of this work (Chapter 2) four particle-tracking algorithms have been implemented and intercompared to estimate the numerical accuracy of the algorithms. The trajectory model describes the motion of a number of discrete particles which positions vary due to advection and a diffusive components, each of them is modeled separately. Two different numerical integration schemes have been developed to compute the particle advection motion. The first is an Eulerian forward and the second is the fourth-order Runge-Kutta method, both algorithms adopt a bilinear spatial interpolation and a linear temporal interpolation method to the eulerian advective field. The diffusive component represents the sub-grid turbulent diffusion due to the unresolved scales in the eulerian motion. A stochastic process parameterization is introduced to simulate the particle turbulent motion. Firstly, these particle-tracking algorithms have been validated with two analytical solutions and the numerical scheme accuracy has been evaluated by means of sensitivity experiments. The experiments have underlined the importance of the temporal resolution of the eulerian field and they show the advantage of both Runge-Kutta and Eurler forward methods for the accurate reproduction of the analytical solutions.

One of the two accurate trajectory models has been then coupled with a realistic Eulerian flow field in order to estimate the generic predictability of particle trajectories in the Adriatic Sea using a large observational data set collected between 2002 and 2004 (Chapter 3). The lagrangian simulations have shown that the average predictability limit of trajectories is 20 km after 3 days of simulation. This value represents the current limit of single trajectories predictability given a resolution of approximately 2 km for the eulerian velocity field. This analysis is a first attempt to evaluate the uncertainty of trajectories forecasts and we believe that increasing the realism of the eulerian flow filed and its time resolution will allow a major improvement in the near future.

The second part of this thesis is dedicated to the MREA concept and its extension to lagrangian predictions (Chapter 4). The MREA philosophy has been extended to the coupling of high resolution models nested in the operational Mediterranean Forecasting System (MFS). The study has concentrated in the design and

execution of a MREA experiment in the Ligurian Sea during May-June 2007. The advantages of the MREA approach for tracer dispersal forecasting can be summarized in the following three points: 1) the relocatable model can be rapidly applied in any region of the sea affected by environmental emergencies; 2) greater resolution and then accuracy in the eulerian field can determine an extended predictability of particle trajectories and 3) nowadays the nested models can be initialized and driven by coarse operational circulation models. The particle trajectories are extremely sensitive to the details of the Eulerian flow and to the small-scale processes that cannot be resolved by coarse resolution grid models. In the past, MREA concepts defined the system design, in terms of observations, climatology and numerical models, needed to increase processes and resolution in limited area of the open ocean and the coastal seas. In our MREA extension, the relocatable models have been successfully nested in operational forecasting models and they have shown to increase the realism of the current simulations.

The relocatable models are shown to be capable to simulate quite accurately the major ocean dynamics of the Ligurian Sea and to ameliorate the mesoscale processes representation. The comparison with data collected in situ has shown that the nested model simulations are in agreement with observations better than the coarse model. The major model errors are a direct consequence of the initialization from coarser model fields: in the future the assimilation of the MREA data directly in the nested model should correct this error.

In the last part of the thesis (Chapter 5) the hypothesis that higher resolution models could increase the predictability of particle trajectories has been verified. The products of relocatable models have been used to drive the trajectory model developed in this thesis and the results have been compared to the drifters released during MREA07. The drifters have been released close to each other to mimic the dispersion of contaminants from a point source. The lagrangian simulations have demonstrated an increase in the lagrangian predictability for one of the three clusters of drifters deployed. The higher resolution current field could improve the lagrangian predictions but further work is necessary to ameliorate the realism of the eulerian flow field in two of the three studied periods.

The next step of this study is the design and the implementation of an operational forecasting system based on the relocatable models (Appendix A). We have started this research during the framework of MREA08 experiment, carried out again in the Ligurian Sea in October 2008. Due to the short time, the results of this experiment are still work in progress. In the thesis we have included only the report of the oceanographic cruises and the description of the operational forecasting system developed. Even if the results are still under validation, it is clear that the nested forecasting system has worked properly.

For the future there are several pending and new open questions to address. Firstly, the trajectory model must be improved in the particle spreading part of the algorithm, introducing a better parameterization of lagrangian turbulence processes depending on the eulerian model resolution. Secondly, the eulerian flow field representation should include the wave propagation and the induced Stokes drifts and probably the tidal currents.

Finally, future research of lagrangian trajectories uncertainty should consider multi-model estimates also by means of nested relocatable models similar to the ones we have implemented in this thesis but not exclusively.

Appendice A

Esperimento di Maritime Rapid Environmental Assessment (MREA08): Rapporto di Crociera

In questa sezione è presentato il rapporto dell'esperimento di Maritime Rapid Environmental Assessment (chiamato MREA08) realizzato nel Mar Ligure dal 29 settembre al 22 ottobre 2008. Il rapporto contiene la descrizione delle campagne oceanografiche effettuate dalla Marina Militare Italiana, l'elaborazione dei dati acquisiti e la presentazione dei risultati preliminari ottenuti dal sistema di previsione sviluppato per l'esperimento. Le previsioni giornaliere dei campi di temperatura, salinità, velocità e d'elevazione della superficie del mare sono state realizzate con un sistema di modelli rilocabili ad alta risoluzione annidati nel modello operativo a grande scala del Mediterraneo (MFS). Un'approfondita elaborazione scientifica dei risultati sarà sviluppata in futuro.

A.1 Istituti partecipanti

All'esperimento MREA08 hanno partecipato i seguenti Istituti ed Enti di Ricerca:

- Istituto Idrografico della Marina (IIM):
  - C.C. Maurizio DeMarte
  - C.C. Piero Di Vasta

- Centro Nazionale di Meteorologia e Climatologia Aeronautica (CNMCA) - Ufficio Spazio Aereo e Meteorologia (USAM):
    Ten. Col. Massimo Ferri
    Cap. Lucio Torrisi
    Brig. Gen. Massimo Capaldo
    Dr. Francesca Marcucci
    Col. Sergio Pasquini.
- Università di Bologna (UNIBO):
    Prof.ssa Nadia Pinardi
    Dott. Nicoletta Fabbroni
- Istituto Nazionale di Geofisica e Vulcanologia (INGV):
    Dr. Paolo Oddo,
    Ing. Massimiliano Drudi
    Ing. Michela Dedominicis
    Dott. Claudia Fratianni
    Dr. Marina Tonani
- Istituto Nazionale di Oceanografia e Geofisica Sperimentale (OGS):
    Dr. Pierre-Marie Poulain
    Dr. Elena Mauri
    Dr. Riccardo Gerin.
- CNR-ISMAR:
    Dr. Annalisa Griffa
- Ente per le nuove Tecnologie, l'Energia e l'Ambiente (ENEA):
    Dr. Giuseppe Manzella
    Dr. Franco Reseghetti
- CNR-ISAC:
    Dr. Rosalia Santoleri

All'esperimento hanno partecipato anche i seguenti partner stranieri:

- NURC:
    Dr. Michel Rixen,

Dr. Alberto Alvarez

- MIT, Cambridge (USA):

  Dr. Pierre Lermusiaux

  Dr. Patrick Haley

  Dr. Wayne Leslie.

A.2 Introduzione

L'esperimento di Maritime Rapid Environmental Assessment (MREA08) rappresenta la continuazione dell'esperienza REA in campo marino iniziata nel 2007 con MREA07, descritto nel Capitolo 4 e Capitolo 5.

MREA08 è stato realizzato nel Mar Ligure nel periodo 29 Settembre-22 Ottobre 2008 per raggiungere i seguenti obiettivi scientifici:

1. Collezionare dati oceanografici per calibrare e validare il sistema MREA finalizzato ad un'applicazione ambientale in mare aperto e costiero;
2. Calibrare e validare il sistema di modelli rilocabili annidato nel modello oceanografico operativo di larga scala;
3. Dimostrare la potenzialità della metodologia MREA nella previsione della dispersione di inquinanti in mare;
4. Studiare i processi di mesoscala del Mar Ligure e il loro impatto sulla dispersione di inquinanti.

La metodologia di REA è stata sviluppata nel campo marino dal gruppo di Harvard del Prof. Allan Robinson per fornire rapidamente un'accurata previsione e simulazione dello stato del mare in supporto alle attività operative. La tecnica REA si basa su un sistema osservativo che fornisce una descrizione dello stato del mare e di una componente modellistica capace di utilizzare le osservazioni collezionate per una rapida previsione dei campi marini. Nell'esperimento MREA08, la parte di modellistica è costituita da un sistema di modelli rilocabili in grado di produrre previsioni dei campi di corrente ad altissima risoluzione orizzontale partendo dai modelli operativi esistenti nell'area, che rilasciano analisi e previsioni in tempo reale. Questi campi di corrente ad alta risoluzione possono

essere utilizzati per simulare e prevedere la dispersione d'inquinanti sia in mare aperto che in prossimità della costa con l'ausilio di un modello di dispersione lagrangiano.

Il sistema di previsioni marine per il Mar Mediterraneo è MFS (Mediterranean Forecasting System) sviluppato all'interno di progetti finanziati dalla Comunità Europea, dal Ministero dell'Ambiente e della Tutela del Territorio e del Mare e dal Ministero degli Affari Esteri ed attualmente mantenuto operativo dal Gruppo Nazionale di Oceanografia Operativa (GNOO) dell'Istituto Nazionale di Geofisica e Vulcanologia (INGV). MFS rilascia tutti i giorni previsioni oceanografiche a dieci giorni dei campi di temperatura, salinità, corrente ed elevazione della superficie del mare su tutta la colonna d'acqua con una risoluzione orizzontale di 1/16°x1/16° (approssimativamente di 6.5 km) e 72 livelli verticali (Tonani *et al.*, 2008). La risoluzione orizzontale di circa 6.5 km rappresenta un fattore limitante per la capacità del modello lagrangiano di prevedere la dispersione di particelle e da qui nasce l'esigenza di usare un modello rilocabile, annidato in MFS, capace sia di usare le informazioni collezionate nell'area d'interesse che di crescere la risoluzione e quindi la dinamica risolta esplicitamente dal modello. La modellistica rilocabile per la sua rapidità d'implementazione e la sua applicabilità in qualsiasi regione di mare aperto e costiero è un efficace strumento per la tutela dell'ambiente marino e per l'adozione di strategie di riduzione e controllo delle emergenze ambientali.

L'esperimento MREA08 rispetto alla precedente esperienza di MREA07 ha sperimentato:

1. Un sistema di trasferimento in tempo quasi reale dei dati acquisiti durante le campagne oceanografiche, dalla nave al centro elaborazione dati;
2. L'assimilazione dei dati oceanografici nel modello operativo MFS;
3. Lo sviluppo di un sistema operativo di produzione delle previsioni giornaliere a tre giorni dei campi di temperatura, salinità e corrente, basato sulla modellistica rilocabile;
4. La previsione giornaliera dello spostamento di drifters, rilasciati durante le campagne.

Il presente rapporto tecnico fornisce una descrizione generale del Mar Ligure (Sezione3), illustra l'attività operativa in mare e l'analisi dei dati oceanografici collezionati (Sezione 4). Nella Sezione 5 è introdotto il sistema di previsione sviluppato con una breve descrizione dei modelli numerici utilizzati e dei risultati preliminari. Le conclusioni sono presentate nella Sezione 6.

A.3 Aspetti generali del Mar Ligure: morfologia e circolazione

Il Mar Ligure è un sottobacino del Mar Mediterraneo centro-settentrionale, a sud è collegato al Mar Tirreno dal canale di Corsica, ad est e a nord bagna rispettivamente le coste della Toscana e della Liguria mentre ad ovest è aperto verso il Mediterraneo occidentale e il Golfo del Leone (Figura A.1).

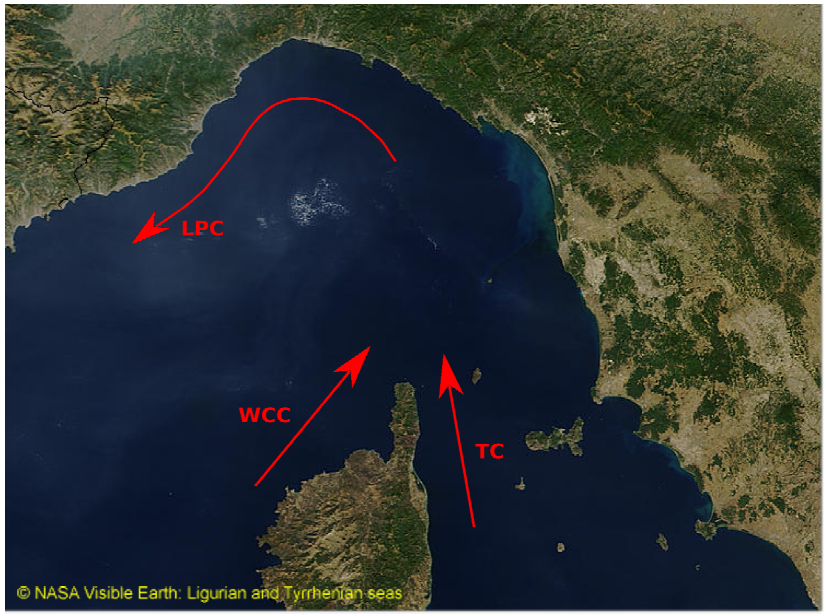

Figura A.1 Mappa del Mar Ligure con uno schema generale della circolazione. LPC (Ligurian-Provencal Current), WCC (West Corsica Current), TC (Tyrrhenian Current)

Il bacino è caratterizzato da una topografia del fondo variabile; a nord le coste presentano una ripida batimetria con una pendenza della piattaforma continentale molto elevata rispetto alle coste italiane. La piattaforma continentale è quasi inesistente e il fondale a 15-30 km dalla costa precipita in una ripida scarpata

verso il fondo della piana abissale che raggiunge una profondità di 2000 metri. La scarpata è incisa da canyon sottomarini tra cui il canyon di Genova considerato il più grande del Mediterraneo; i cigli delle sue pareti distano 50 km l'uno dall'altro e la lunghezza complessiva del suo avallamento è di oltre 70 km lungo i quali il fondale precipita da 200 a 2400 m di profondità.

La circolazione del Mar Ligure è caratterizzata da un permanente giro ciclonico più intenso in inverno che in estate. Il bacino è attraversato in superficie da una corrente settentrionale di Acque Atlantiche Modificate (MAW-Modified Atlantic Water) prodotte dal congiungimento a Nord di Capraria della corrente tirrenica (TC-Tyrrhenian Current) e della corrente occidentale corsa (WCC-West Corsica Current). La corrente settentrionale diventa corrente liguro-provenzale (LPC-Ligurian Provençal Current) che scorre verso il Golfo del Leone completando il giro ciclonico. La circolazione ciclonica del bacino ligure si osserva sia negli strati superficiali che in quelli d'acqua profonda. La colonna d'acqua del bacino Ligure è caratterizzata dalle masse d'acqua della MAW e delle Acque Levantine Intermedie Modificate (MLIW-Modified Levantine Intermediate Water). La MAW rappresenta lo strato più superficiale (0-100m) sono acque atlantiche caratterizzate da bassi valori di salinità e temperature mentre la MLIW, che entra nel bacino ligure attraverso il Canale di Corsica, è localizzata ad una profondità di 200-600 metri con alti valori di salinità.

A.4 Attività operativa in mare

L'attività operativa in mare ha interessato l'area geografica delimitata dalle seguenti coordinate: 8°24'E-10°E di longitudine e 43°18'N-44°26'24''N di latitudine. La fase operativa ha previsto lo svolgimento delle seguenti attività:

- Acquisizione di profili di temperatura e salinità tramite sonda CTD e lancio degli XBT durante i trasferimenti nave tra le zone in cui sono state eseguite misure CTD;
- Rilascio di 10 drifters di tipo CODE con sistema di posizionamento ARGOS e GPS; i drifters sono stati forniti: 6 dall'INGV (ID: 85741, 85742, 85743,

85744, 85745, 85746), 2 dal CNR (ID: 85747, 85748) e 2 dall'OGS (ID: 85193, 85194). Il piano originale prevedeva il lancio separato di due clusters da 5 drifters ciascuno, in seguito a causa del malfunzionamento di una boa è stato deciso di effettuare tre lanci separati di 3 clusters composti ciascuno da 3 drifters.

- Messa a mare del glider di proprietà dell'OGS, in grado di monitorare le variabili oceanografiche lungo un percorso prefissato.

L'acquisizione dei dati oceanografici e la messa a mare dei drifters e del glider sono state eseguite con tre campagne oceanografiche condotte dalla nave Magnaghi dell'Istituto Idrografico della Marina Militare Italiana. Le tre crociere sono state identificate come FaseI, FaseII e FaseIII:

1. FaseI: dal 29 Settembre al 1 Ottobre (3 giorni),
2. FaseII: dal 9 al 11 Ottobre (3 giorni),
3. FaseIII: dal 19 al 22 Ottobre (4 giorni).

Nelle sezioni seguenti è fornita una descrizione di ciascuna fase operativa e un'analisi dei dati collezionati.

A.4.1FaseI

L'attività operativa in mare effettuata nella prima fase ha portato all'esecuzione del campionamento raffigurato in Figura A.2 completato dal 29 Settembre al 1 Ottobre. A causa delle cattive condizioni meteomarine il piano di campionamento originale è stato parzialmente ridimensionato e in totale sono state effettuate 7 stazioni CTD e lanciati 10 XBT. Le coordinate, il tempo d'acquisizione e la massima profondità dei profili CTD e XBT sono riportate nella Tabella A.1 e Tabella A.2.

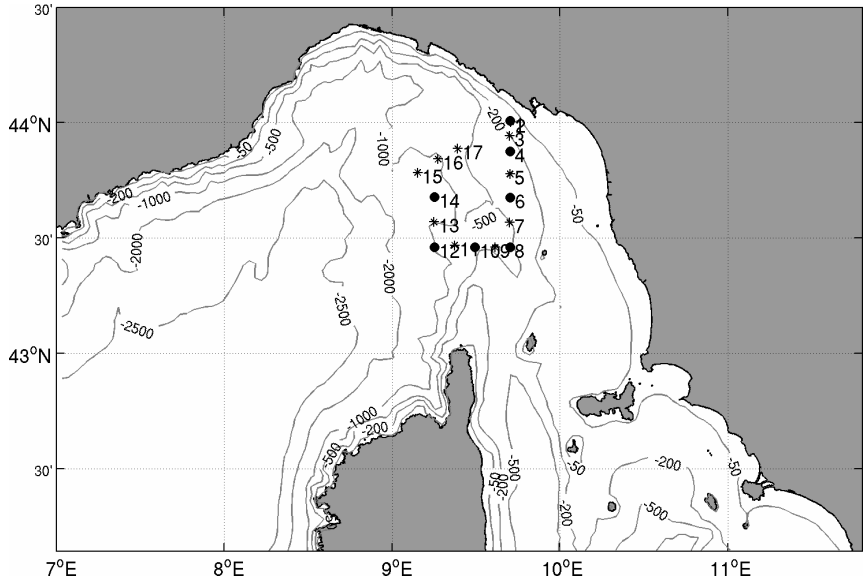

Figura A.2 Posizioni delle stazioni CTD (•) e XBT (*) collezionate nella FaseI (dal 29 settembre al 1 ottobre) con la batimetria del Mar Ligure (in metri).

N° stazione	Data	Ora	Latitudine N (° ‘)	Longitudine E (° ‘)	Profondità (m)
1	30.09.08	10.09	44 0.44	9 42.10	90
4	30.09.08	12.09	43 52.56	9 42.24	327
6	30.09.08	16.09	43 40.52	9 42.17	455
8	30.09.08	18.09	43 27.56	9 42.09	443
10	30.09.08	20.09	43 27.57	9 29.58	436
12	30.09.08	22.09	43 27.63	9 15.14	604
14	01.10.08	2.10	43 40.73	9 15.21	461

Tabella A.1 Elenco delle stazioni CTD effettuate durante la FaseI.

N° stazione	Data	Ora	Latitudine N (° ‘)	Longitudine E (° ‘)	Profondità (m)
2	30.09.08	10.10	44 0.26	9 42.33	114
3	30.09.08	11.15	43 56.66	9 42.00	282
5	30.09.08	15.04	43 46.66	9 42.09	393
7	30.09.08	17.34	43 34.04	9 42.02	513
9	30.09.08	19.55	43 27.56	9 36.76	426
11	30.09.08	21.47	43 28.10	9 22.32	553
13	01.10.08	0.59	43 34.15	9 14.95	925
15	01.10.08	6.31	43 47.02	9 9.07	928
16	01.10.08	7.19	43 50.55	9 16.4	909
17	01.10.08	8.01	43 53.26	9 23.42	537

Tabella A.2 Elenco delle stazioni XBT effettuate durante la FaseI.

I profili verticali di temperatura, salinità e il diagramma T/S delle CTD e XBT sono raffigurati in Figura A.3A,B,C. I profili di temperatura e salinità evidenziano uno strato superficiale (0-50metri) rimescolato e un marcato termoclino posizionato nei primi cento metri della colonna d'acqua. Lo strato delle acque atlantiche modificate si estende fino alla profondità di 200 metri alla quale troviamo un minimo di temperatura (T~13.5°C, S~38.4 PSU). I profili di salinità evidenziano la presenza delle MLIW (200-600 m) con il massimo sottosuperficiale di salinità (T~13.8°C, S~38.6 PSU) posizionato vicino ai 400 metri. Il diagramma T/S (Figura A.3C) evidenzia le masse d'acqua caratteristiche del bacino: la MAW e la MLIW e le loro proprietà fisiche.

Le distribuzioni orizzontali di temperatura e salinità a 4 metri di profondità (Figura A.4A,B), costruite con l'analisi oggettiva, mostrano campi omogenei. Nei campi di temperatura è presente un debole fronte termico che divide le acque calde costiere da quelle fredde del mare aperto mentre è assente un gradiente nella distribuzione della salinità, evidenziato nei dati oceanografici collezionati durante MREA07 per il periodo maggio-giugno (Capitolo 4). Durante la FaseI è stato lanciato il primo cluster di 5 drifters vicino alla boa ODAS (9°9'54''E-43°47'18''N). La posizione di lancio dei drifters ha seguito lo schema di una croce, un drifter centrale vicino alla boa ODAS e i restanti 4 drifters ad una distanza di circa 500 metri dalla boa centrale in direzione nord, est, sud e ovest. In questo primo lancio si è verificato il malfunzionamento del drifter a85741 e lo spiaggiamento, dopo soli 3 giorni, della boa a85742 recuperata e riutilizzata nella FaseIII. Le coordinate e le date dei rilasci sono indicate nella Tabella A.3 mentre le traiettorie sono rappresentate in Figura A.5.

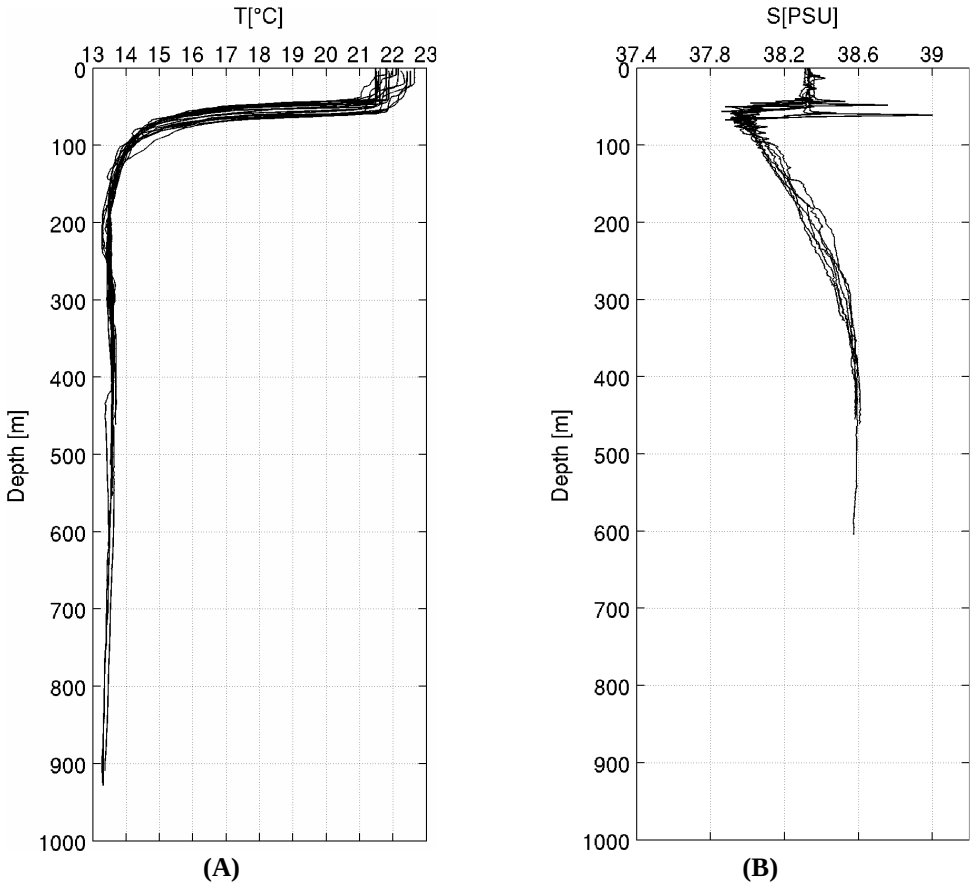

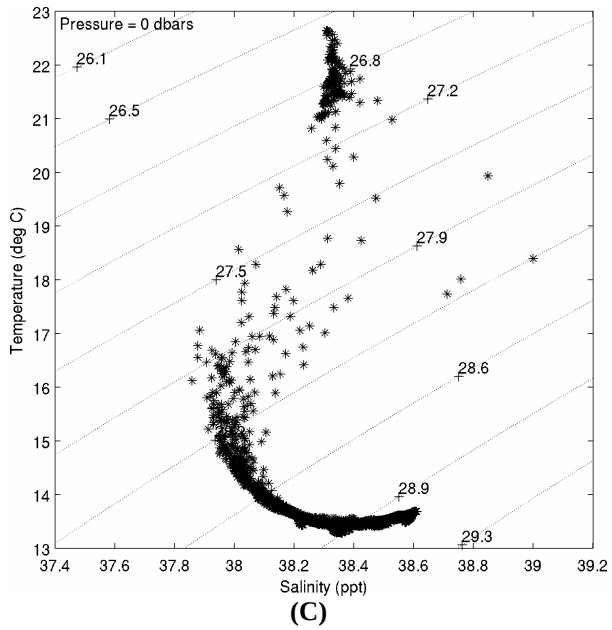

(C)

Figura A.3 Profili verticali di (A) temperatura [°C], (B) salinità [PSU] e (C) diagramma T/S per le stazioni CTD e XBT collezionate durante la FaseI.

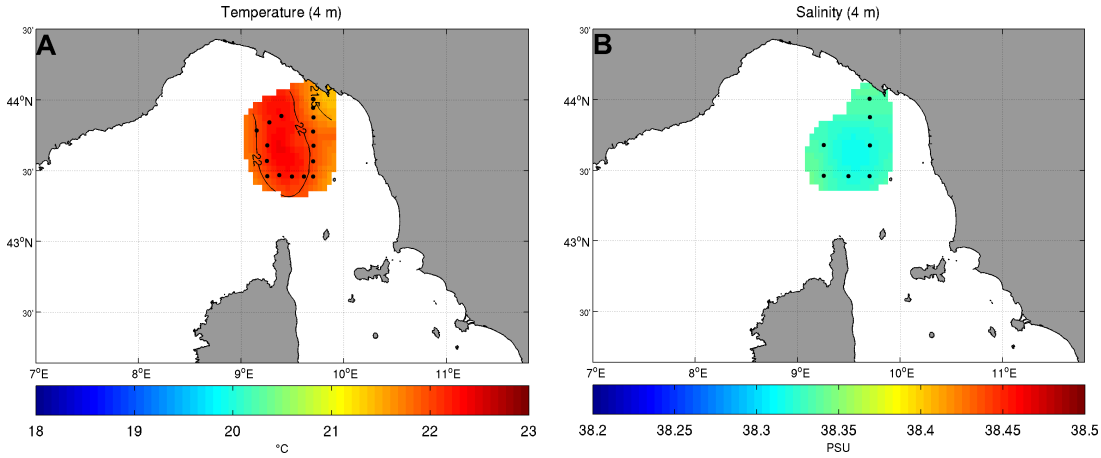

Figura A.4 Mappe della temperatura [°C] e della salinità [PSU] a 4 metri di profondità.

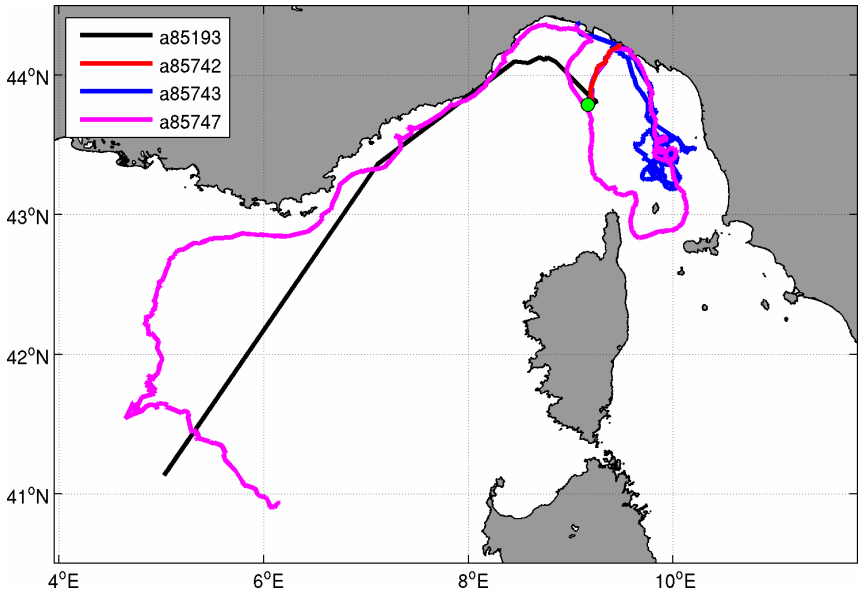

Figura A.5 Traiettorie dei drifters rilasciati durante la FaseI, in verde è indicata la posizione della boa ODAS, zona di lancio dei drifters.

ID Drifter	Data Rilascio (gg.mm.aa hh:mm:ss)	Latitudine N (° ‘)	Longitudine E (° ‘)	Ultimo segnale (gg.mm.aa hh:mm:ss)
a85193	01.10.08 06:35:00	43 47.34	9 9.90	08.12.08 22.00:00
a85747	01.10.08 06:33:00	43 47.28	9 10.20	09.12.08 00:00:23
a85741	01.10.08 06:28:00	43 47.04	9 10.02	01.10.08 06:00:00
a85742	01.10.08 06:24:00	43 47.28	9 9.72	03.10.08 12:00:00
a85743	01.10.08 06:19:00	43 47.58	9 9.90	08.12.08 23:00:00

Tabella A.3 Coordinate e data del rilascio del primo cluster di 5 drifters.

A.4.2Fase II

La FaseII è stata condotta dal 9 al 11 Ottobre; il piano di campionamento mostrato in Figura A.6 è stato eseguito in 3 giorni durante i quali sono state misurate 23 stazioni CTD e lanciati 23 XBT. Le posizioni, le date e la profondità massima dei profili verticali acquisiti sono riportate in Tabella A.4 e Tabella A.5.

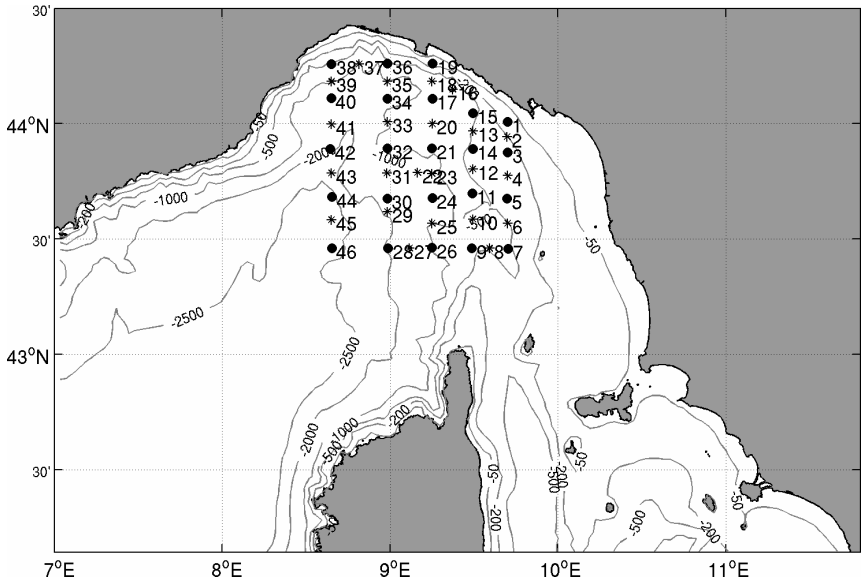

Figura A.6 Posizioni delle stazioni CTD (•) e XBT (*) collezionate nella FaseII (9-11 ottobre) con la batimetria del Mar Ligure (in metri).

I profili verticali di temperatura e salinità e il diagramma T/S dei dati oceanografici sono rappresentati in Figura A.7A,B,C. I profili verticali mostrano una variabilità superficiale della temperatura tra i 18.5-21-5 °C, la presenza di uno strato rimescolato superficiale di profondità variabile e un termoclino ben definito collocato nei primi 100 metri della colonna d'acqua. I profili di salinità mostrano un andamento simile ai dati acquisiti nella FaseI; è sempre evidente il segnale delle acque MLIW con un massimo sottosuperficiale di salinità a 400 metri di profondità (T~13.5°C, S~38.6 PSU). Il diagramma T/S (Figura A.7C) mostra un'ampia variabilità delle temperature. Le distribuzioni orizzontali di temperatura a 4 metri (Figura A.8A) evidenziano la presenza di un fronte termico che separa le acque costiere calde da quelle fredde del mare aperto con direzione principale

Sud-Nord. I campi di salinità a 4m (Figura A.8B) presentano un forte gradiente, l'acqua a maggiore salinità si trova vicino alla costa italiana, da questa struttura procedendo verso est s'incontra una lingua d'acqua meno salata e subito dopo un'altra zona a maggior salinità. Durante questa campagna il secondo cluster di 3 drifters è stato rilasciato in mare seguendo lo schema di lancio della FaseI. Le posizioni sono riportate in Tabella A.6 e le traiettorie raffigurate in Figura A.9.

N° stazione	Data	Ora	Latitudine N (° ')	Longitudine E (° ')	Profondità (m)
1	09.10.08	16.10	44 0.53	9 41.88	101
3	09.10.08	17.10	43 52.48	9 41.97	323
5	09.10.08	19.10	43 40.53	9 41.81	453
7	09.10.08	21.10	43 27.41	9 42.22	434
9	09.10.08	23.10	43 27.62	9 29.15	456
11	10.10.08	2.10	43 41.81	9 29.32	425
14	10.10.08	6.10	43 53.51	9 29.47	421
15	10.10.08	6.10	44 2.69 9	9 29.50	461
17	10.10.08	9.10	44 6.45	9 15.06	549
19	10.10.08	10.10	44 15.63	9 15.15	100
21	10.10.08	11.10	43 53.59	9 14.94	430
24	10.10.08	15.10	43 40.71	9 15.06	506
26	10.10.08	17.10	43 27.77	9 14.90	463
28	10.10.08	19.10	43 27.66	8 59.22	468
30	10.10.08	21.10	43 40.53	8 58.95	514
32	10.10.08	23.10	43 53.56	8 59.05	456
34	11.10.08	1.10	44 6.58	8 58.93	508
36	11.10.08	3.10	44 15.61	8 59.08	464
38	11.10.08	5.10	44 15.56	8 39.01	465
40	11.10.08	6.10	44 6.66	8 38.93	437
42	11.10.08	9.10	43 53.48	8 38.61	455
44	11.10.08	11.10	43 40.92	8 39.16	457
46	11.10.08	13.10	43 27.61	8 39.11	929

Tabella A.4 Elenco delle stazioni CTD effettuate durante la FaseII.

N° stazione	Data	Ora	Latitudine N (° ‘)	Longitudine E (° ‘)	Profondità (m)
2	09.10.08	16.36	43 56.59	9 41.82	225
4	09.10.08	18.36	43 46.49	9 41.98	392
6	09.10.08	20.59	43 34.10	9 42.01	517
8	09.10.08	22.50	43 27.59	9 35.48	429
10	10.10.08	1.00	43 35.17	9 29.51	259
12	10.10.08	3.20	43 48.17	9 29.55	437
13	10.10.08	5.21	43 58.03	9 29.59	460
16	10.10.08	7.30	44 8.94	9 22.40	692
18	10.10.08	9.16	44 11.02	9 15.00	908
20	10.10.08	11.03	44 0.02	9 15.03	679
22	10.10.08	13.29	43 47.27	9 9.86	912
23	10.10.08	14.11	43 47.05	9 15.01	899
25	10.10.08	16.31	43 34.07	9 15.02	890
27	10.10.08	18.31	43 27.60	9 6.96	901
29	10.10.08	20.32	43 37.13	8 58.99	912
31	10.10.08	22.29	43 47.19	8 58.88	895
33	11.10.08	0.43	44 0.45	8 59.03	908
35	11.10.08	2.32	44 10.97	8 58.92	939
37	11.10.08	4.21	44 15.57	8 48.97	920
39	11.10.08	6.08	44 10.99	8 39.02	915
41	11.10.08	7.57	43 59.85	8 39.04	76
43	11.10.08	10.28	43 47.16	8 39.03	934
45	11.10.08	12.33	43 35.0	8 39.05	944

Tabella A.5 Elenco delle stazioni XBT effettuate durante la FaseII.

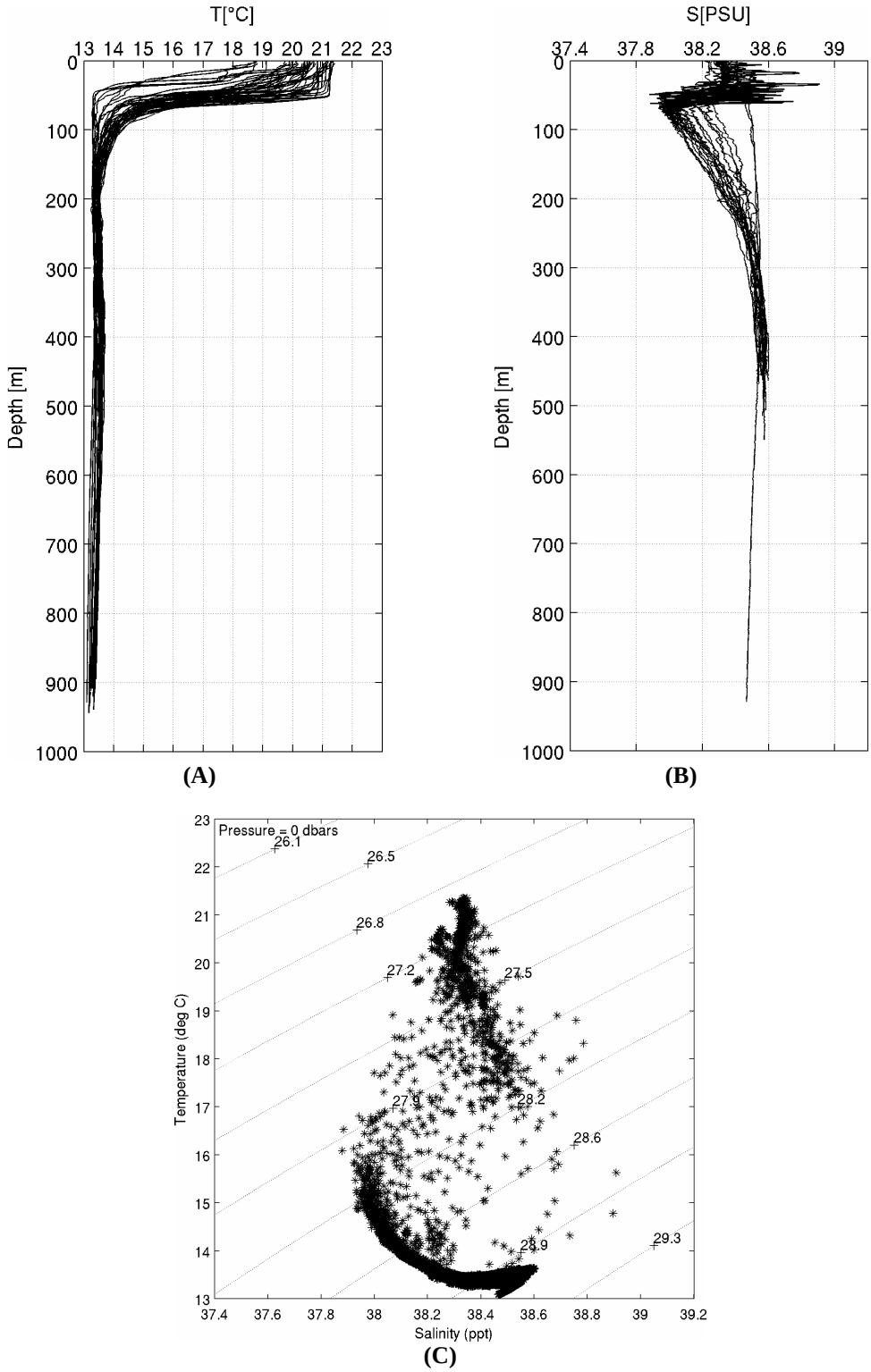

Figura A.7 Profili verticali di (A) temperatura [°C], (B) salinità [PSU] e (C) diagramma T/S per le stazioni CTD e XBT collezionate durante la FaseII.

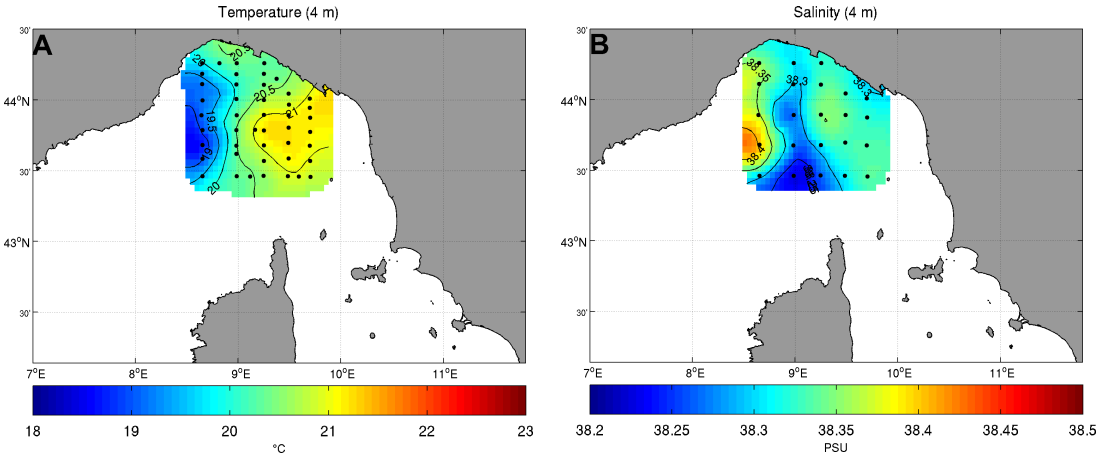

Figura A.8 Mappe della temperatura [°C] e della salinità [PSU] a 4 metri di profondità.

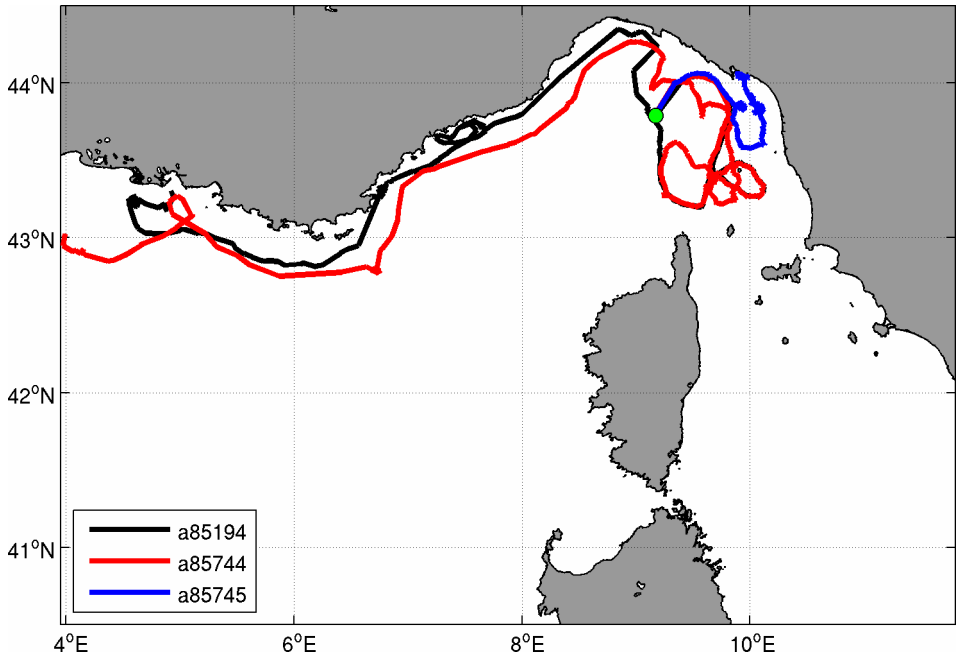

Figura A.9 Traiettorie dei drifters rilasciati durante la FaseII, in verde è indicata la posizione della boa ODAS zona di lancio dei drifters.

ID Drifter	Data Rilascio (gg.mm.aa hh:mm:ss)	Latitudine N (° ‘)	Longitudine E (° ‘)	Ultimo segnale (gg.mm.aa hh:mm:ss)
a85194	11.10.08 15:20:00	43 47.28	9 10.20	08.12.08 22:01:11
a85744	11.10.08 15:36:00	43 47.28	9 9.72	09.12.08 01:01:11
a85745	11.10.08 15:41:00	43 47.58	9. 9.96	08.12.08 22:00:00

Tabella A.6 Coordinate e data del rilascio del secondo cluster di 3 drifters.

A.4.3Fase III

La FaseIII di MREA08 condotta dal 19 al 22 ottobre ha portato all'esecuzione del piano di campionamento rappresentato in Figura A.10 che comprende un totale di 23 stazioni CTD e 26 lanci XBT; informazioni sulle posizioni dei dati oceanografici sono date in Tabella A.7 e Tabella A.8.

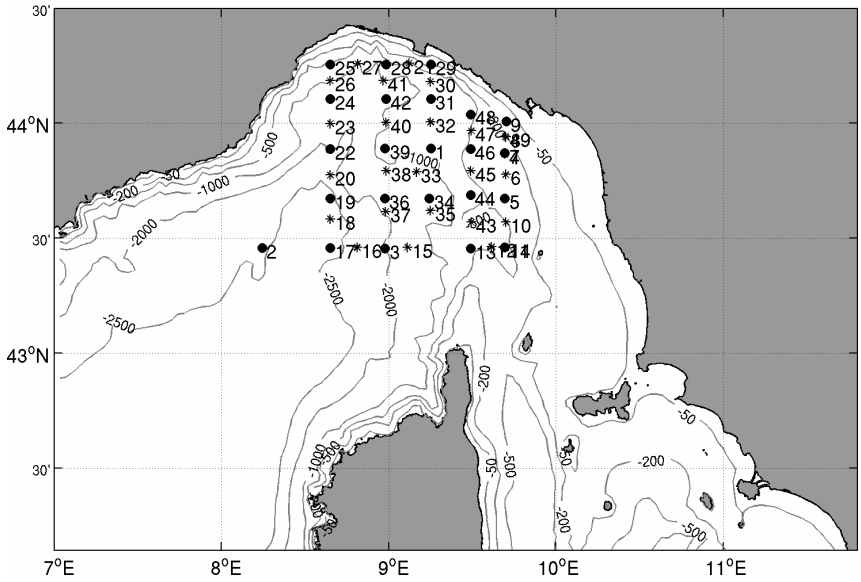

Figura A.10 Posizioni delle stazioni CTD (•) e XBT (*) collezionate nella FaseIII (19-22 ottobre) con la batimetria del Mar Ligure (in metri).

I profili verticali di temperatura e salinità e il diagramma T/S sono rappresentati in Figura A.11A,B,C. I profili di temperatura evidenziano uno strato superficiale rimescolato e un forte termoclino come per i dati collezionati nella FaseI e FaseII. In superficie la temperatura varia nell'intervallo di 19°-22°C. Il segnale delle acque levantine è ben visibile sia nei profili di salinità che nel diagramma T/S. La distribuzione di temperatura a 4 m di profondità (Figura A.12A) evidenzia sempre l'esistenza di un fronte termico che divide le acque costiere calde da quelle fredde di mare aperto con direzione principale SE-NW. La mappa di salinità (Figura A.12B) presenta acque a minor salinità vicino alle zone costiere, una struttura a meandro di acque a maggior salinità e nella parte centrale del bacino un nucleo d'acqua meno salata. Durante la FaseIII è stato rilasciato il terzo e ultimo cluster

di tre drifters seguendo sempre lo schema di lancio ufficiale; le posizioni sono indicate in Tabella A.9 e le traiettorie sono rappresentate in Figura A.13.

N° stazione	Data	Ora	Latitudine N (° ‘)	Longitudine E (° ‘)	Profondità (m)
1	19.10.08	22.10	43 53.38	9 15.03	416
2	20.10.08	2.10	43 27.40	8 14.58	455
3	20.10.08	4.10	43 27.37	8 58.58	453
5	20.10.08	12.10	43 40.36	9 41.57	456
7	20.10.08	15.10	43 52.30	9 41.57	88
9	20.10.08	16.10	44 0.54	9 42.07	88
11	20.10.08	21.10	43 27.55	9 41.49	423
13	20.10.08	23.10	43 27.30	9 29.39	435
17	21.10.08	6.10	43 27.39	8 39.08	504
19	21.10.08	8.10	43 40.41	8 39.03	460
22	21.10.08	10.10	43 53.33	8 39.02	506
24	21.10.08	12.10	44 6.38	8 39.08	606
25	21.10.08	14.10	44 15.33	8 39.07	454
28	21.10.08	16.10	44 15.33	8 59.08	457
29	21.10.08	18.10	44 15.36	9 15.13	101
31	21.10.08	20.10	44 6.39	9 15.06	457
34	22.10.08	0.10	43 40.39	9 14.60	417
36	22.10.08	2.10	43 40.42	8 58.54	401
39	22.10.08	4.10	43 53.39	8 58.59	405
42	22.10.08	10.10	44 6.35	8 59.00	461
44	22.10.08	17.10	43 41.33	9 29.28	404
46	22.10.08	20.10	43 53.32	9 29.28	408
48	22.10.08	23.10	44 2.38	9 29.33	425

Tabella A.7 Elenco delle stazioni CTD effettuate durante la FaseIII.

N° stazione	Data	Ora	Latitudine N (° ‘)	Longitudine E (° ‘)	Profondità (m)
4	20.10.08	9.50	43 52.07	9 41.62	424
6	20.10.08	13.55	43 46.63	9 41.92	392
8	20.10.08	16.05	43 56.40	9 41.98	194
10	20.10.08	21.07	43 34.17	9 41.97	546
12	20.10.08	22.55	43 27.73	9 36.90	430
14	21.10.08	0.36	43 27.57	9 41.82	570
15	21.10.08	3.30	43 27.60	9 6.73	582
16	21.10.08	5.50	43 27.58	8 48.60	590
18	21.10.08	7.35	43 35.00	8 39.05	930
20	21.10.08	9.25	43 46.50	8 39.04	925
21	21.10.08	10.00	44 15.66	9 7.30	444
23	21.10.08	11.16	43 59.90	8 39.04	941
26	21.10.08	14.10	44 11.11	8 38.99	920
27	21.10.08	16.07	44 15.58	8 48.83	916
30	21.10.08	19.23	44 10.94	9 15.02	893
32	21.10.08	21.19	44 0.33	9 15.02	702
33	21.10.08	23.23	43 47.33	9 9.90	896
35	22.10.08	1.06	43 37.16	9 14.88	892
37	22.10.08	2.20	43 36.94	8 58.83	916
38	22.10.08	3.55	43 47.58	8 59.03	890
40	22.10.08	5.30	44 0.23	8 58.98	884
41	22.10.08	10.02	44 11.16	8 58.01	792
43	22.10.08	16.00	43 34.15	9 29.57	178
45	22.10.08	19.10	43 47.60	9 29.46	427
47	22.10.08	22.32	43 58.06	9 29.50	467
49	23.10.08	1.20	43 56.59	9 41.82	496

Tabella A.8 Elenco delle stazioni XBT effettuate durante la FaseIII.

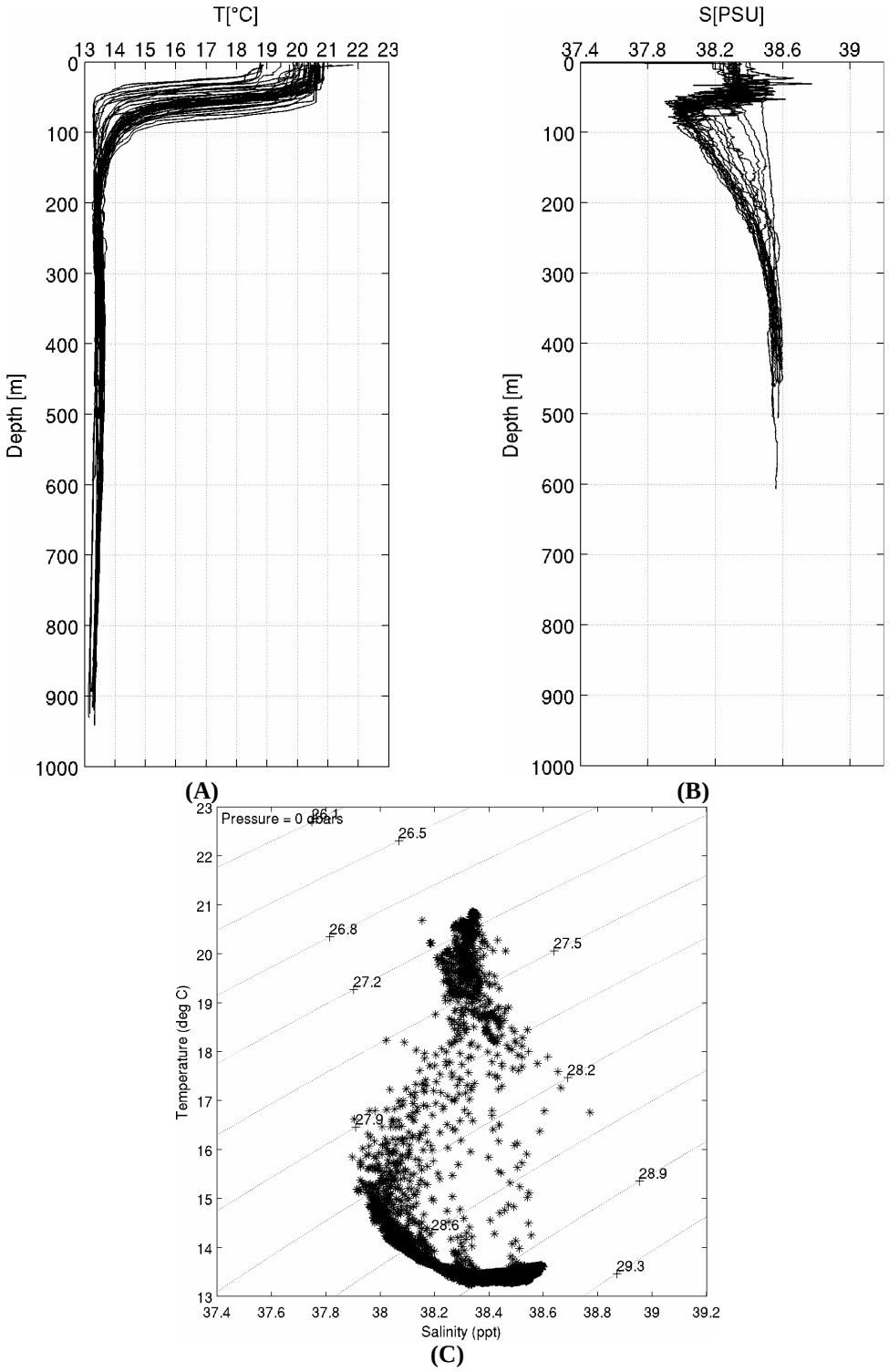

Figura A.11 Profili verticali di (A) temperatura [°C], (B) salinità [PSU] e (C) diagramma T/S per le stazioni CTD e XBT collezionate durante la FaseIII.

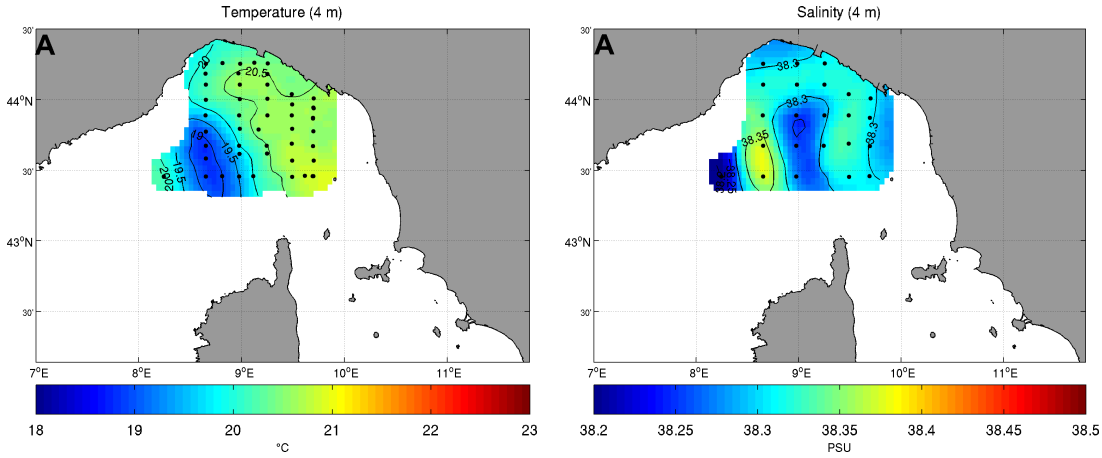

Figura A.12 Mappe della temperatura [°C] e della salinità [PSU] a 4 metri di profondità.

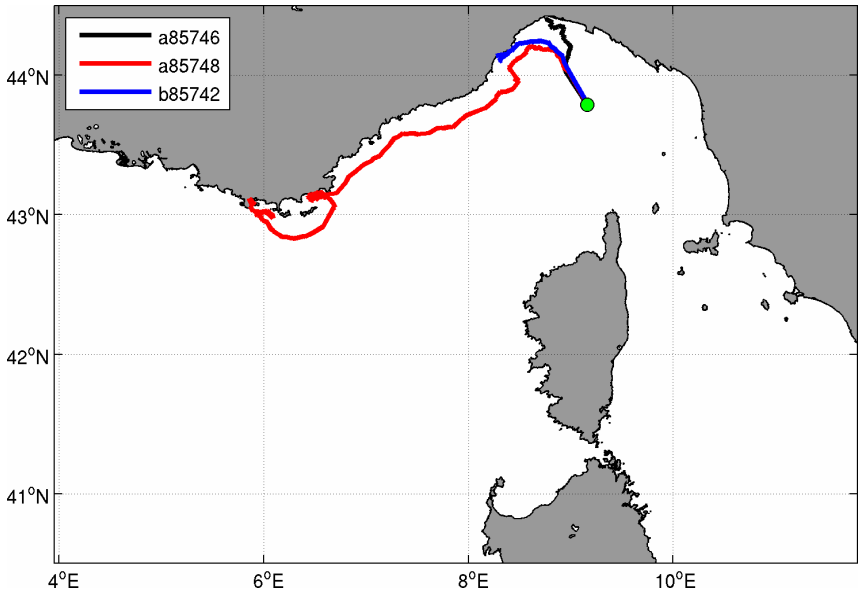

Figura A.13 Traiettorie dei drifters rilasciati durante la FaseIII, in verde è indicata la posizione della boa ODAS zona di lancio dei drifters.

ID Drifter	Data Rilascio (gg.mm.aa hh:mm:ss)	Latitudine N (° ‘)	Longitudine E (° ‘)	Ultimo segnale (gg.mm.aa hh:mm:ss)
a85746	22.10.08 23:22:00	43 47.28	9 9.72	30.10.08 14:03:28
a85748	22.10.08 23:29:00	43 47.28	9 10.20	08.12.08 23:00:00
b85742	22.10.08 23:20:00	43 47.58	9 9.96	31.10.08 08:01:40

Tabella A.9 Coordinate e data del rilascio del terzo cluster di 3 drifters.

A.5 Modellistica Numerica

Al sistema osservativo, acquisito grazie ad un'intensa attività operativa, è stata affiancata la modellistica numerica per la previsione dei campi oceanografici. I modelli numerici di circolazione utilizzati in MREA08 sono: il Mediterranean Forecasting System (MFS) che fornisce le previsioni per tutto il Mediterraneo e i modelli rilocabili implementati nel bacino Ligure, il Ligurian Intermediate Model (LIM) e il Ligurian High Resolution Model (LHRM). Questi modelli euleriani sono stati accoppiati con il modello di traiettorie per la previsione della dispersione dei drifters. In particolare durante l'esperimento MREA08 sono state sviluppate le seguenti azioni:

1. La creazione di un sito ftp dedicato all'esperimento per la trasmissione e la condivisione dei dati;
2. L'assimilazione settimanale dei dati oceanografici di CTD e XBT in MFS;
3. Lo sviluppo di un sistema operativo di previsioni marine basato sulla modellistica rilocabile.

A.5.1 Sito ftp

Durante l'esperimento MREA08 è stato utilizzato un sito ftp per la raccolta:

1. dei dati oceanografici collezionati durante le tre campagne;
2. delle previsioni marine prodotte dai modelli numerici di circolazione;
3. dei campi atmosferici e di temperatura superficiale del mare da satellite.

I vari partners del progetto avevano il compito di aggiornare i files presenti sul sito secondo le loro aree di competenza.

La Figura A.14 mostra l'albero delle directory del sito ftp; la directory principale è MREA08_GNOO che contiene 6 sottodirectory dedicate agli istituti partecipanti:

1. **INGV**: contiene i prodotti del sistema MFS; le analisi, le simulazioni e le previsioni a media giornaliera (MFS_Sys2b_daily) e oraria (MFS_Sys2b_hourly).

2. **CNMCA_USAM**: raccoglie un ampio dataset del forzante atmosferico a diversa risoluzione spaziale e temporale messo a disposizione dall'Aeronautica militare. Il dataset comprende le analisi e le previsioni degli ECMWF con risoluzione di 0.5° x 0.5° e di 0.25° x 0.25° a frequenza temporale di 6 hrs e le previsioni a 72 ore del modello COSMO-ME ad altissima risoluzione orizzontale (7km) e temporale (3hrs).
3. **UNIBO**: contiene le previsioni a 3 giorni rilasciate dal sistema rilocabile annidato in MFS, HOPS1 rappresenta il modello intermedio a 3km mentre HOPS2 identifica il secondo sistema a maggiore risoluzione (1km). La sottodirectory LDM raccoglie i risultati delle previsioni dello spostamento dei drifters prodotti dal modello lagrangiano accoppiato al modello rilocabile.
4. **OGS**: raccoglie sia i dati dei drifters lanciati durante le tre campagne che i dati del glider.
5. **CNR**: fornisce i campi medi giornalieri di temperatura superficiale del mare (SST) rilevata da satellite. Si tratta di temperature interpolate con tecniche d'interpolazione ottimale sulla griglia del modello MFS.
6. **ENEA_IIM**: raccoglie i profili verticali di temperatura e salinità acquisiti da CTD e XBT durante le tre campagne di MREA08.

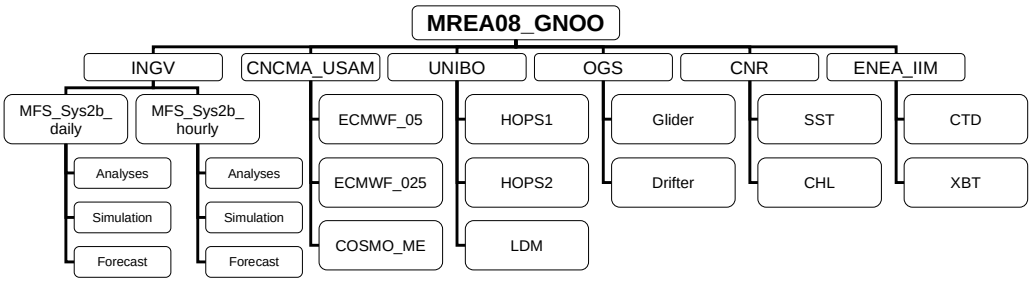

Figura A.14 Albero delle directory del sistema ftp attivato durante l'esperimento MREA08.

A.5.2Assimilazione dati in MFS

I profili verticali di temperatura e salinità, acquisiti con CTD e XBT nelle tre campagne oceanografiche (FaseI, FaseII e FaseIII), dopo aver superato un controllo di qualità effettuato nel centro di raccolta dell'ENEA di La Spezia, sono stati assimilati dal sistema previsionale MFS. MFS rilascia giornalmente le previsioni per il Mar Mediterraneo a dieci giorni dei campi di temperatura, salinità, corrente ed elevazione della superficie del mare con una risoluzione orizzontale di 1/16° x 1/16° (approx. 6.5 km), una descrizione dettagliata del modello operativo si trova in Tonani *et al.* (2008). Il sistema è costituito oltre che da un modello numerico anche da uno schema d'assimilazione che permette di correggere ed aggiornare le simulazioni del modello con i dati disponibili. La procedura d'assimilazione è eseguita settimanalmente, ogni martedì i dati da satellite (SLA) e in situ (XBT, ARGO, CTD) disponibili (Dobricic *et al*, 2007) vengono integrati con le simulazioni del modello tramite lo schema SOFA (Software for Ocean Forecast Assimilation), in modo da ottenere la condizione iniziale dal quale far partire la previsione forzando il modello numerico con i dati atmosferici di previsione. Seguendo questa procedura i dati di MREA08 sono stati assimilati con successo dal modello ogni martedì successivo a ciascuna campagna.

A.5.3Sistema rilocabile: LIM e LHRM

Il sistema rilocabile è un'implementazione dell'Harvard Ocean Prediction System (HOPS). HOPS è un sistema integrato di software che permette un approccio multidisciplinare nel campo oceanografico, la previsione delle correnti e una realistica simulazione dell'oceano per studiare i processi di mesoscala. La parte principale è costituita da un modello idrodinamico alle equazioni primitive con l'approssimazione di superficie libera; le variabili prognostiche di temperatura, salinità e correnti sono calcolate su una griglia ArakawaB, una descrizione dettagliata del sistema è fornita da Robinson (1996,1999), Robinson *et al.* (1996) and Lozano *et al.* (1996). La versione di HOPS utilizzata in MREA08 calcola

interattivamente i flussi di calore e momento alla superficie del mare dai dati di forzante atmosferico prodotti dal modello ad alta risoluzione COSMO-ME.

I domini dei due sistemi rilocabili sono rappresentati in Figura A.15. Il primo modello rilocabile LIM, annidato in MFS, è stato implementato nel Mar Ligure nell'area geografica delimitata dalle seguenti coordinate: 42.14° N - 44.49° N di latitudine e 6.9° E -11.8°E di longitudine con una risoluzione orizzontale di 3km e 40 livelli "double-sigma" per il sistema verticale.

Il secondo modello rilocabile LHRM comprende l'area tra i 43.26°N - 44.49°N di latitudine e tra i 8.34° E - 10.02°E di longitudine e presenta una risoluzione orizzontale di 1 km con 40 livelli verticali "double-sigma". L'accoppiamento tra i modelli numerici è stato eseguito secondo la tecnica del "one-way nesting"; il modello a bassa risoluzione fornisce le condizioni iniziali e laterali al modello ad alta risoluzione. Nel nostro sistema il modello LIM è inizializzato e forzato dai campi di MFS e a sua volta fornisce le condizioni iniziali e al contorno per il modello LHRM.

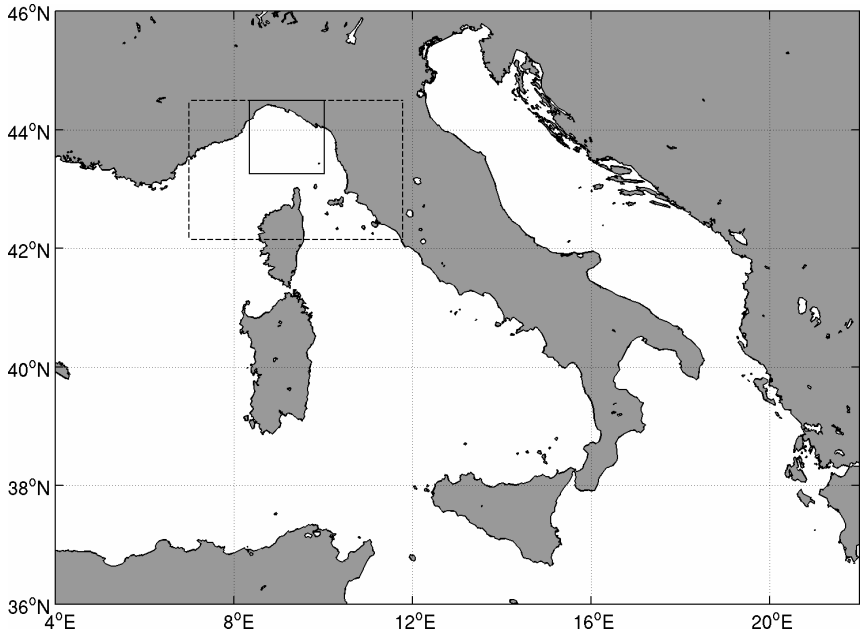

Figura A.15 Rappresentazione dei domini dei modelli numerici. Il Mar Mediterraneo è il dominio di MFS, l'area delimitata dalla linea tratteggiata è il dominio di LIM (3km) mentre l'area delimitata dalla linea continua è il dominio di LHRM (1km).

A.5.4Sistema di produzione delle previsioni

L'aspetto più innovativo dell'esperimento MREA08 è stato lo sviluppo di un sistema di previsione che ha fornito giornalmente le previsioni marine a tre giorni dei campi di temperatura, salinità, corrente ed elevazione della superficie del mare. Il sistema basato sui modelli rilocabili ad alta risoluzione, il LIM e il LHRM, è costituito da due catene operative sequenziali completamente automatiche rappresentate in Figura A.16 e Figura A.17.

Per fare le previsioni il sistema ha utilizzato le analisi e il forecast del forzante atmosferico COSMO-ME, rilasciato giornalmente dall'Aeronautica Militare, e le analisie e le previsioni prodotte sempre giornalmente da MFS.

La prima catena operativa interessava la produzione delle previsioni con il modello LIM seguita dalla seconda catena operativa dedicata al modello LHRM. Ogni giorno la produzione si attivava circa alle 5:00 UTC per finire approssimativamente alle 13:00 UTC. La partenza era vincolata dall'orario di rilascio dei dati atmosferici e dei prodotti MFS scaricati dal sito ftp di MREA_GNOO e sottoposti a pre-processing. Il modello LIM è stato inizializzato e forzato al contorno dai prodotti MFS, mentre il modello LHRM a 1km è stato inizializzato e forzato al contorno dalle previsioni del LIM. I prodotti dei modelli rilocabili erano caricati giornalmente sul sito ftp di MREA08 e pubblicati in una pagina dedicata sul sito web del Laboratorio di Simulazione Numeriche del Clima e degli Ecosistemi Marini (SINCEM) dell'Università di Bologna (http://www.sincem.unibo.it/index.php?option=com_content&view=article&id=11). A seguire, i prodotti dei modelli rilocabili forzavano il modello di traiettorie per la previsione dello spostamento dei drifters.

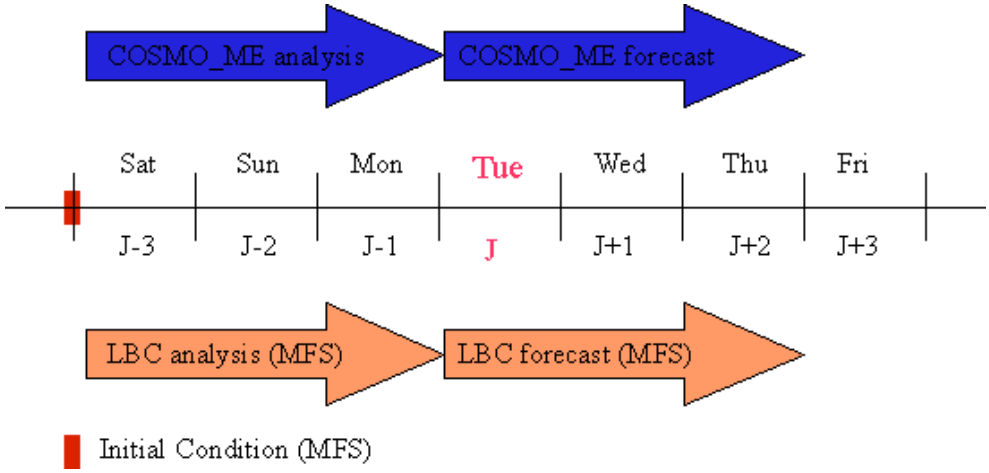

Figura A.16 Schema di produzione delle previsioni con il LIM. Le frecce indicano i dati esterni utilizzati per le previsioni. Il modello LIM è inizializzato tre giorni prima dalle analisi di MFS. LBC (Lateral Boundary Condition).

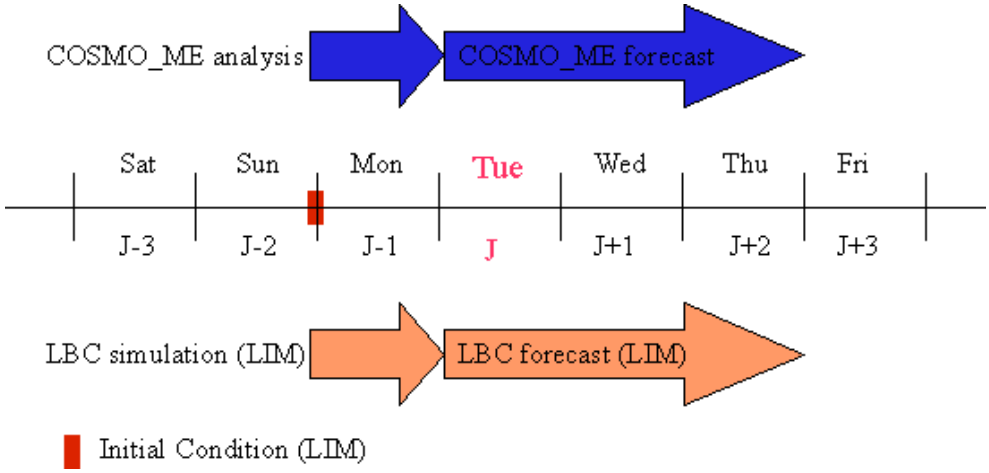

Figura A.17 Schema di produzione delle previsioni con il LHRM. Le frecce indicano i dati esterni utilizzati per le previsioni. Il modello LHRM è inizializzato un giorno prima dal modello LIM. LBC (Lateral Boundary Condition).

A.5.5Risultati preliminari

In questa sezione sono presentati i risultati preliminari ottenuti dal sistema di previsione. Un'approfondita elaborazione e una dettagliata analisi dei risultati saranno fornite in un rapporto tecnico futuro.

La Figura A.18 mostra le previsioni dei campi istantanei di velocità e temperatura prodotte dai modelli LIM e LHRM per i giorni 1, 2 e 3 ottobre 2008. Le distribuzioni di temperatura evidenziano la presenza di un fronte termico vicino alle zone costiere che separa le acque calde della costa da quelle fredde del mare aperto. Il campo di velocità, prodotto dal LIM, per il primo ottobre (Figura A.18A) mostra un'intensa corrente sul lato occidentale della Corsica che alimenta il giro ciclonico posizionato al centro del bacino Ligure, con una ben definita LPC che scorre vicino alla costa italiana e francese verso ovest. La TC sul lato orientale della Corsica invece presenta una forte attenuazione. Le previsioni ottenute con il LHRM (Figura A.18B,D,F) per gli stessi giorni riproducono le strutture presenti nel LIM, con una maggiore definizione della LPC.

In Figura A.19 sono rappresentati i risultati delle previsioni a tre giorni dello spostamento dei tre clusters di drifters sviluppate con il modello di traiettoria accoppiato al modello rilocabile LIM. La Figura A.19A mostra lo spostamento per tre giorni del primo cluster, rilasciato il primo d'ottobre; la Figura A.19B riproduce le previsioni di traiettoria per il secondo cluster rilasciato durante la seconda campagna e la Figura A.19C rappresenta le traiettorie numeriche per il terzo cluster.

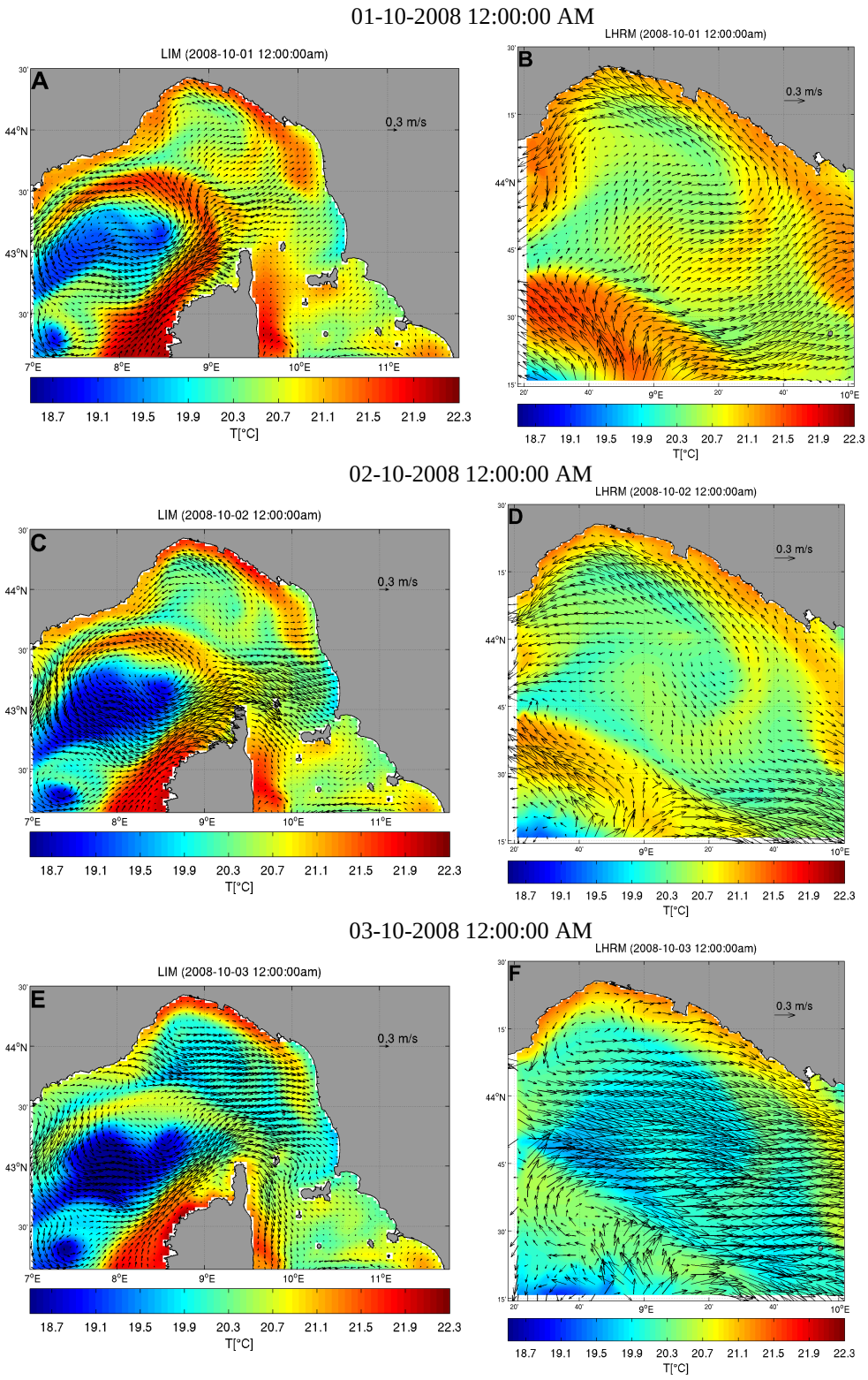

Figura A.18 Campi superficiali (1.5 m) di velocità [m/s] e temperatura (°C) previsti dal modello rilocabile LIM (A),(C),(E) e LHRM (B),(D),(F). Non tutti i punti griglia dei modelli sono stati rappresentati.

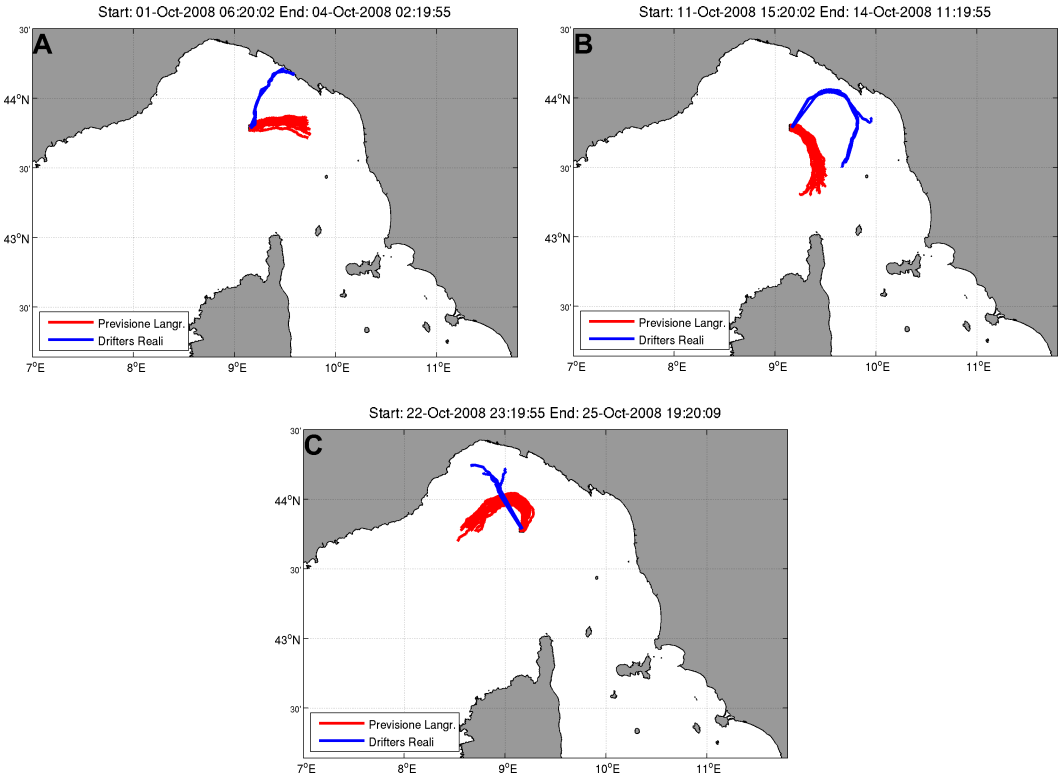

Figura A.19 Confronto tra le traiettorie numeriche previste con il modello di traiettoria (linee rosse) e i drifters reali (linee blu) per il primo cluster (A), secondo cluster (B) e il terzo cluster (C).

A.6 Conclusioni

Questo rapporto tecnico ha presentato i primi risultati dell'esperimento MREA08 condotto nel Mar Ligure dal 29 Settembre al 22 Ottobre 2008. Obiettivi principali dell'esperimento sono stati di sviluppare una metodologia MREA finalizzata ad un'applicazione in campo ambientale e validare un sistema di modelli rilocabili, annidati in un modello di circolazione di larga scala, utili nella previsione di dispersione d'inquinanti in mare. L'aspetto innovativo di questo esperimento è stato lo sviluppo di un sistema di previsione marine basato sulla modellistica rilocabile, capace di rilasciare giornalmente le previsioni a tre giorni dei campi di velocità, temperatura, salinità ed elevazione della superficie del mare.

Durante MREA08 sono state eseguite dall'Istituo Idrografico della Marina Militare Italiana tre campagne oceanografiche, la prima dal 29 settembre al primo ottobre, la seconda fase dal 9 al 11 ottobre e la terza dal 19 al 22 ottobre. Durante le crociere sono stati acquisti profili verticali di temperatura e salinità tramite sonda CTD e XBT e sono stati lanciati 10 drifters.

L'attività operativa in mare è stata affiancata da un intenso impegno nel campo della modellistica numerica.

I dati oceanografici sono stati assimilati settimanalmente con successo nel sistema operativo MFS dal Gruppo Nazionale di Oceanografia Operativa dell'INGV. Inoltre per MREA08 è stato sviluppato un efficiente sistema operativo di previsione basato sui modelli rilocabili ad alta risoluzione, implementati nel Mar Ligure. Il sistema, per tutta la durata dell'esperimento, ha rilasciato giornalmente le previsioni orarie a tre giorni dei campi di velocità, temperatura, salinità ed elevazione della superficie del mare. Le previsioni dei campi di corrente ad alta risoluzione sono state utilizzate nel modello lagrangiano di traiettorie per la previsione della dispersione dei drifters.

I risultati dei modelli numerici sono ancora sotto analisi ma il sistema si è dimostrato stabile ed efficiente.

Bibliography

- AL-RABEH, A.H., CEKIRGE, H.M., GUNAY, N., 1989. A stochastic simulation model of oil spill fate and transport. *Applied Mathematical Modelling*, 13, 322-329.
- AL-RABEH, A.H., GUNAY, N., 1992. On the application of a particle dispersion model. *Coastal Engineering*, 17, 195-210.
- ARAKAWA, A., 1972. Design of the UCLA general circulation model. Numerical simulation of weather and climate. Tech. Rep. 7, Dept. of Meteorology, University of California, Los Angeles, 116 pp.
- ARAKAWA, A., LAMB, V.R., 1977. Method in Computational Physics, 17, 173-265.
- ARTEGIANI, A., AZZOLINI, R., SALUSTI, E., 1989. On the dense water in the Adriatic Sea. *Oceanology Acta*, 12, 151-160.
- ARTEGIANI, A., BREGANT, D., PASCHINI, E., PINARDI, N., RAICICH, F., RUSSO, A., 1997a. The Adriatic Sea general circulation. Part I: Air Sea interactions and water mass structure. *Journal of Physical Oceanography*, 27, 1492-1514.
- ARTEGIANI, A., BREGANT, D., PASCHINI, E., PINARDI, N., RAICICH, F., RUSSO, A, 1997b. The Adriatic Sea general circulation. Part II: Baroclinic circulation structure. *Journal of Physical Oceanography*, 27, 1515-1532.
- ASTRALDI, M., GASPARINI, G.P., MANZELLA, M.R., 1990. Temporal variability of currents in the eastern Ligurian Sea. *Journal of Geophysical Research*, 95(C2), 1515 -1522.
- ASTRALDI, M., GASPARINI, G.P., 1992. The seasonal characteristics of the circulation in the north Mediterranean Basin and their relationship with the

atmospheric-climatic conditions. *Journal of Geophysical Research*, 97(C6), 9531-9540.

- BARBANTI, R., URSELLA, L., POULAIN, P.-M., 2004. Interpolazione mediante kriging di dati lagrangiani e confronto tra i dati del Mar Nero e del Mar Adriatico, Rapporto Tecnico 73/2003/OGA/29, Istituto Nazionale di Oceanografia e di Geofisica Sperimentale, Trieste, Italy.
- BARBANTI, R., IUNGWIRTH, R., POULAIN, P-M., 2005. Stima dell'accuratezza del drifter tipo CODE con GPS nella determinazione della posizione geografica. Rapporto Tecnico 32/2005/OGA/20, Istituto Nazionale di Oceanografia e di Geofisica Sperimentale, Trieste, Italy.
- BELETSKY, D., SCHWAB, D.J., MCCORMICK, M.J., 2006. Modeling 1998-2003 summer circulation and thermal structure in Lake Michigan. *Journal of Geophysical Research*, 111.
- BELETSKY, D., MASON, D.M., SCHWAB, D.J., RUTHERFORD, E.S., JANSSEN J., CLAPP, D.F., DETTMERS, J.M., 2007. Biophysical model of larval yellow perch advection and settlement in Lake Michigan. *Journal of Great Lakes Research*, 33, 842-866.
- BIGNAMI, F., MARULLO, S., SANTOLERI, R., SCHIANO, M.E., 1995. Longwave radiation budget in the Mediterranean Sea. *Journal of Geophysical Research*, 100(C2), 2501–2514.
- BLANKE, B., RAYNAUD, S., 1997. Kinematics of the Pacific Equatorial Undercurrent: an Eulerian and Lagrangian approach from GCM result. *Journal of Physical Oceanography*, 27, 1038-1053.
- BLANKE, B., ARHAN, M., MADEC, G., ROCHE, S., 1999. Warm water paths in the equatorial Atlantic as diagnosed with a general circulation model. *Journal of Physical Oceanography*, 29, 2753-2768.
- BLANKE, B., SPEICH, S., MADEC, G., DÖÖS, K., 2001. A global diagnostic of interocean mass transfers. *American Meteorological Society*, 31, 1623-1632.
- BLUMBERG, A.F., MELLOR, G.L., 1987. A description of a three-dimensional coastal ocean circulation model. In. Heaps, N.S. (Ed.), Three-dimensional coastal ocean models. *American Geophysical Union*, Washington, DC, p. 208.

- BONAVITA, M., TORRISI, L., 2005. Impact of a Variational Objective Analysis Scheme on a Regional Area Numerical Model: The Italian Air Force Weather Service Experience. *Meteorology and Atmospheric Physics*, 88, No. 1-2.
- CARTER, E.F., ROBINSON, A.R., 1987. Analysis models for the estimation of oceanic fields. *Journal of Atmospheric and Oceanic Technology*, 4, 49-74.
- CUSHMAN-ROISIN, B., 1994. *Introduction to Physical Oceanography*. Prentice-Hall, New Jersey, USA.
- DAVIS, R.E., 1985. Drifter observations of coastal currents during CODE: The method and descriptive view. *Journal of Geophysical Research*, 90, 4741-4755.
- DE MEY, P., BENKIRAN, M., 2002: A multivariate reduced order optimal interpolation method and its application to the Mediterranean basin-scale circulation. In Pinardi N. and Woods J.D., (Eds): *Ocean Forecasting: conceptual basis and applications*, Spinger-Verlag, 281-306.
- DIMOU, K.N., ADAMS, E.E., 1993. A random-walk, particle tracking model for well-mixed estuaries and coastal waters. *Estuarine, Coastal and Shelf Science*, 37, 99–110.
- DOBRICIC, S., PINARDI, N., ADANI, M., TONANI, M., FRATIANNI, C., BONAZZI, A., FERNANDEZ, V., 2007. Daily oceanographic analyses by the Mediterranean basin scale assimilation system. *Ocean Sciences*, 3, 149-157.
- DÖÖS, K., 1995. Interocean exchange of water masses. *Journal of Geophysical Research*, 100, 13499-13514.
- FISCHER H.B., LIST, E. J., KOH, R.C.Y., IMBERGER, J., BROOKS, N.H., 1979. *Mixing in Inland and Coastal waters*. Academic Press, USA.
- GARDINER, C. W., 1985. *Handbook of stochastic methods for physics, chemistry and the natural sciences*. Berlin: Springer-Verlag.
- GILL, A.E., 1982. *Atmosphere-Ocean Dynamics*. Academic Press, New York. International Geophysics Series, 30, 662 pages.
- GRIFFA, A., PITEBARG, L.I., OZGOKMEN, T., 2004. Predictability of Lagrangian particle trajectories: Effects of smoothing of the underlying Eulerian flow. *Journal of Marine Research*, 62, 1-35.

- HANSEN, D.V., POULAIN, P.-M., 1996. Processing of WOCE/TOGA drifter data. *Journal of Atmospheric and Oceanic Technology*, 13, 900-909.
- HELLERMAN, S., ROSESTEIN, M., 1983. Normal monthly wind stress over the world ocean with error estimates. *Journal of Physical Oceanography*, 13, 1093-1104.
- HUNTER, J.R., 1987. The applications of Lagrangian particle tracking techniques to modeling of dispersion in the sea. In: Noye J. (ed) *Numerical Modeling: Applications to Marine Systems*. Elsevier Science Publishers, Amsterdam, p 295.
- HUNTER, J.R., CRAIG, P.D., PHILLIPS, H.E., 1993. On the use of random walk models with spatially variable diffusivity. *Journal of Computational Physics*, 106:366–367.
- KONDO, J., 1975. Air-sea bulk transfer coefficients in diabatic conditions. *Boundary Layer Meteorology*, 9, 91-112.
- LERMUSIAUX, P.F.J., 1997. Error subspace data assimilation methods for ocean field estimation: theory, validation and applications. *Harvard Open Ocean Model Reports*, vol. 55. Harvard University, Cambridge, MA, 402 pp.
- LOZANO, C.J., HALEY, P.J., ARANGO, H.G., SLOAN, Q., ROBINSON, A.R., 1994. Harvard coastal/deep water primitive equation model. *Harvard Open Ocean Model Reports*, No. 52, Harvard University, Cambridge, MA, 15 pp.
- LOZANO, C.J., ROBINSON, A.R., ARANGO, H.G., GANGOPADHYAY, A., SLOAN, N.Q., HALEY, P.J., ANDERSON, L., LESLIE, W.G., 1996. An interdisciplinary ocean prediction system: Assimilation strategies and structured data models. *Modern Approaches to Data Assimilation in Ocean Modelling*, P. Malanotte-Rizzoli, ed., Elsevier Oceanography Series, Elsevier Science, The Netherlands.
- MADEC, G., DELECLUSE, P., IMBARD, M., LEVY, C., 1998. OPA8.1 Ocean general Circulation Model reference manual. Note du Pole de modelisazion, Institut Pierre-Simon Laplace (IPSL), France, 11.
- MANCA, B.B., KOVACEVIC, V., GACIC, M., VIEZZOLI, D., 2001. Dense water formation in the southern Adriatic Sea and spreading into the Ionian Sea in the period 1997-1999. *Journal of Marine Systems*, 33/34, 133-154.

- MEDAR/MEDATLAS Group, 2002. MEDAR/MEDATLAS 1998-2001 Mediterranean and Black Sea database of temperature, salinity and bio-chemical parameters and climatological atlas (4CDroms), European Commission Marine Science and Technology Programme, and internet server http://www.ifremer.fr/sismer/program/medarIFREMER/TMSI/IDM/SISMER Ed. Centre de Brest).
- NOYE, J., 1987. Numerical methods for solving the transport equation. In: Noye J. (ed) *Numerical Modeling: Applications to Marine Systems*. Elsevier Science Publishers, Amsterdam.
- ODDO, P., PINARDI, N., ZAVATARELLI, M., 2005. A numerical study of the interannual variability of the Adriatic Sea (2000-2002). *Science of the Total Environment*, 353 (1-3), 39-56.
- ODDO, P., PINARDI, N., ZAVATARELLI, M., COLUCELLI, A., 2006. The Adriatic Basin Forecasting System. *Acta Adriatica*, 47 (suppl), 169-184.
- ODDO, P., GUARNIERI, A., PINARDI, N., 2007. Operational Ocean Forecasting in the Adriatic Sea Recent Improvements. In 38th Congress Proceedings, 38, CIESM, Istanbul, Turchia.
- ORLANSKI, I., 1976. A simple boundary condition for unbounded hyperbolic flows. *Journal of Computational Physics*, 41, 251-269.
- OVCHINNIKOV, I.M., ZATS, V.I., KRIVOSHEYA, V.G., NEMIROSKY, M.S., UDODOV, A.I., 1987. Winter Convection in the Adriatic and formation of deep eastern Mediterranean water. *Annales Geophysicae*, 5B, 89-92.
- PACANOWSKI, R.C., PHILANDER, S.G.H., 1981: Parameterization of vertical mixing in numerical models of tropical oceans. *Journal of Physical Oceanography*, 11(11), 1443-1451.
- PEDLOSKY, J., 1987. *Geophysical Fluid Dynamics*. 2d ed. Springer-Verlag, 710 pp.
- PERKINS, A.L., SMEDSTAD, L.F., BLAKE, D.W., HEBURN, G.W., WALLCRAFT, A.J., 1997. A new nested boundary condition for a Primitive-Equation ocean model. *Journal of Geophysical Research*, 102, 3483-3500.

- PINARDI, N., AUCLAIR, F., CESARINI, C., DEMIROV, E., FONDA-UMANI, S., GIANI, M., MONTANARI, G., ODDO, P., TONANI, M., ZAVATARELLI, M., 2002. Toward marine environmental predictions in the Mediterranean Sea coastal areas: a monitoring approach. In *Ocean Forecasting* (Eds) Pinardi, N., Woods, J., Springer & Verlag.
- PINARDI, N., ALLEN, I., DEMIROV, E., DE MEY, P., KORRES, G., LASCARATOS, A., LE TRAON, P.Y., MAILLARD, C., MANZELLA, G., TZIAVOS, C., 2003. The Mediterranean ocean Forecasting System: first phase of implementation (1998-2001). *Annales Geophysicae*, 21, 1, 3-20.
- POULAIN, P.-M., 1999. Drifter observations of surface circulation in the Adriatic Sea between December 1994 and March 1996. *Journal of Marine System*, 20, 231-253.
- POULAIN, P.-M., 2001. Adriatic Sea surface circulation as derived from drifter data between 1990 and 1999. *Journal of Marine System*, 29, 3-32.
- POULAIN, P.M., CUSHMAN-ROISIN, B., 2001. Circulation In: Physical Oceanography of the Adriatic Sea, Past, present and future, (Eds.) Cushman-Roisin, B., Gacic, M., Poulain, P.M., Artegiani, A, Kluwer Academic Publ., 67-109.
- POULIQUEN, E., KIRWAN, A.D., PEARSON, R.T., 1997. Rapid Environmental Assessment. Proceedings of a conference held in Lerici, Italy, 10-14 March 1997, SANCLANTCEN Conference Proceedings Series CP-44.
- PRESS, W.H., FLANNERY B.P., TEUKOLSKY S.A., VETTERLING W.T., 1986. *Numerical Recipes*. Cambridge Univ. Press, Cambridge, UK.
- RAICICH, F., 1996. On the fresh water balance of the Adriatic Sea. *Journal of Marine System*, 9, 305-319.
- REED, R.K., 1977. On estimating insolation over ocean. *Journal of Physical Oceanography*, 17, 854-871.
- RISKEN, H., 1989. *The Fokker-Planck equation*. Ed. Springer-Verlag, Berlin.
- ROBINSON, A.R., 1996. Physical processes, field estimation and an approach to interdisciplinary ocean modeling. *Earth-Science Reviews*, 40, 3-54.

- ROBINSON, A.R., ARANGO, H.G., WARN-VARNAS, A., LESLIE, W.G., MILLER, A.J., HALEY, P.J., LOZANO, C.J., 1996. Real-time regional forecasting. *Modern Approaches to Data Assimilation in Ocean Modeling* (P.Malanotte-Rizzoli, ed.), Elsevier Oceanography Series, Elsevier Science, The Netherlands, 377-412.
- ROBINSON, A.R., 1999. Forecasting and simulating coastal ocean processes and variabilities with the Harvard ocean prediction system. In: Mooers, C.N.K. (Ed.), Coastal Ocean Prediction. *American Geophysical Union Coastal and Estuarine Studies Series*, pp. 77-100.
- ROBINSON, A.R., LERMUSIAUX, P.F.J., 2002. Data assimilation for modeling and predicting coupled physical-biological interactions in the sea. In: Robinson, A.R., McCarthy, J.J., Rothschild, B.J., (Eds), *THE SEA*: Volume 12: Biological-Physical Interactions in the Sea. John Wiley and Sons, NY, pp. 475-536.
- ROBINSON, A.R., LERMUSIAUX, P.F.J., 2004. Prediction systems with data assimilation for coupled ocean science and ocean acoustics. In: Tolstoy, A., Teng, Y.-C., Shang, E.C., (Eds), *Theoretical and Computational Acoustics 2003*. World Scientific Publishing, pp. 325-342.
- ROSSBY, C.G., MONTGOMERY, R.G., 1935. The layer of frictional influence in wind and ocean currents. Pap. Phys. Oceanogr. Meteor. 3, *Annual Reviews*, 101 pp.
- ROULLET, G., MADEC, G., 2000: Salt conservation, free surface, and varying levels: a new formulation for ocean general circulation models. *Journal of Geophysical Research*, 105, C10, 23,927-23,942.
- SCHÖNFELD, W., 1995. Numerical simulation of the dispersion of artificial radionuclides in the English Channel and the North Sea. *Journal of Marine System*, 6, 529-544.
- SHAPIRO, R., 1970. Smoothing, filtering, and boundary effects. *Reviews of Geophysics and Space Physics*, 8(2), 359-387.

- SPAULDING, M.L., KOLLURU, V.S., ANDERSON, E., HOWLETT, E., 1994. Applciation of Three-Dimensional Oil Spill Model (WOSM/OILMAP) to Hindcast the braer spill. *Spill Science & Technology Bulletin*, 1 (1), 23-35.
- STOMMEL, H., (1948). The West-ward intensification of Wind-Driven Ocean Currents. *Transactions of the American Geophysical Union*.
- TAYLOR, G.I., 1921. *Diffusion by continuous movements*. Proc. London Math. Soc., 20, 373-416.
- TOMPSON, A.P.B., GELHAR, L.W., 1990. Numerical simulation of solute transport in three-dimensional randomly heterogeneous porous media. *Water Resources Research*, 26, 2541-2562.
- TONANI, M., PINARDI, N., DOBRICIC, S., PUJOL, I., FRATIANNI, C., 2008. A high resolution free surface model of the Mediterranean Sea. *Ocean Sciences*, 4, 1-14.
- URSELLA, L., BARBANTI, R., POULAIN, P.-M., 2004. Dolcevita Drifter Program: Rapporto tecnico finale. Rel.77/2004/OGA/30.
- URSELLA, L., POULAIN, P.-M., SIGNELL, R.P., 2006. Surface drifter derived circulation in the northern and middle Adriatic Sea: Response to wind regime and season. *Journal of Geophysical Research*, 112, C03S04, doi:10.1029/2005JC003177.
- URSELLA, L., POULAIN, P.-M., SIGNELL, R.P., 2007. Surface drifter derived circulation in the northern and middle Adriatic Sea: Response to wind regime and season. *Journal of Geophysical Research*, Vol. 12.
- XIE, P., ARKIN, P.A., 1997. Global Precipitation: A 17-year monthly analysis based on gauge observations, satellite estimates, and numerical model outputs. *Bulletin of the American Meteorological Society*, 78, 2539-2558.
- ZAVATARELLI, M., PINARDI, N., KOURAFALOU, V.H., MAGGIORE, A., 2002. Diagnostic and prognostic model studies of the Adriatic Sea circulation. Seasonal variability. *Journal of Geophysical Research*, 107, Ant. No. 3004.
- ZAVATARELLI, M., PINARDI N., 2003. The Adriatic Sea modelling system: a nested approach. *Annales Geophysicae*, 21, 345-364.